12-31-2003

Spatially varying threshold models for the automated segmentation of radiodense tissue in digitized mammograms

Richard Edson Eckert III
Rowan University

Spatially varying threshold models for the automated segmentation of radiodense tissue in digitized mammograms

by

Richard Edson Eckert III

A Thesis Submitted to the

Graduate Faculty in Partial Fulfillment of the

Requirements for the Degree of

MASTER OF SCIENCE

Department: Electrical and Computer Engineering
Major: Engineering (Electrical Engineering)

Approved: Members of the Committee

_____ _____

In Charge of Major Work

_____ _____

For the Major Department

_____ _____

For the College

Rowan University
Glassboro, New Jersey
2003

TABLE OF CONTENTS

LIST OF FIGURES

LIST OF TABLES

ABSTRACT

The percentage of radiodense (bright) tissue in a mammogram has been correlated to an increased risk of breast cancer. This thesis presents an automated method to quantify the amount of radiodense tissue found in a digitized mammogram. The algorithm employs a radial basis function neural network in order to segment the breast tissue region from the remainder of the X-ray. A spatially varying Neyman-Pearson threshold is used to calculate the percentage of radiodense tissue and compensate for the effects of tissue compression that occurs during a mammography procedure. Results demonstrating the efficacy of the technique are demonstrated by exercising the algorithm on two separate sets of mammograms – one obtained from Brigham Women's Hospital, Harvard Medical School and the other set obtained from Fox Chase Cancer Center and digitized at Rowan University. The results of the algorithm compare favorably with a previously established manual segmentation technique.

ACKNOWLEDGEMENTS

I would like to begin by sincerely thanking my advisor, Dr. Shreekanth Mandayam, for his wisdom and guidance. I would also like to thank Dr. Jennifer Kadlowec, Dr. Anthony Marchese, and Dr. Robi Polikar for serving on my committee and providing me with constructive feedback.

Much appreciation goes to Dr. Marilyn Tseng, of Fox Chase Cancer Center in Philadelphia, Pennsylvania, whose grants "Dietary Patterns and Breast Density," *American Institute of Cancer Research*, Collaborative Research with Fox Chase Cancer Center, and "Dietary Patterns and Breast Density in Chinese American Women," *American Cancer Society*, Collaborative Research with Fox Chase Cancer Center, funded this research.

I would like to thank Dr. Celia Byrne, formerly at the Brigham and Women's Hospital at Harvard Medical School in Cambridge, Massachusetts who provided me with useful information regarding validation of this research. Also, Dr. Kathy Evers, MD, of Fox Chase Cancer Center for helping to understand analysis of mammograms from a radiologist's point of view.

Throughout the course of this research, there have been many people involved. I would like to particularly thank Dan Barrot, Lyndsay Burd, and Mike Kim for their help.

Finally, I would like to thank my friends and family for their support in helping me to complete this thesis.

CHAPTER 1: INTRODUCTION

The second leading cause of mortality among Americans is malignant neoplasms or cancer. Cancer is second only to heart disease as the leading cause of death among Americans. Reports indicate an estimated 553,000 deaths in Americans due to cancer in the year 2000. Cancer accounts for 23% of the total number of deaths; 21.8% among females and 24.3% among males. The second leading cause of cancer related deaths among women is breast cancer, exceeded only by lung cancer [1]. Breast cancer accounts for nearly one of every three cancers diagnosed in American women [2] and it is estimated that 1 in 8 women in the United States will develop breast cancer in their lifetime [3]. Early detection of breast cancer and the use of breast cancer risk factors through application of mammography screening along with improvement in breast cancer treatments has attributed to the recent decline in breast cancer mortality [4,5].

1.1 Medical Imaging in Mammography

Scientists have come a long way since the initial attempt at the development of a machine specifically designed for producing mammograms. From what was at first essentially a tripod supporting a special X-ray camera, the medical industry is now beginning to incorporate the idea of beaming digital mammograms via satellite to doctors in remote locations around the world. Mammography is a special type of X-ray imaging used to create a more detailed image of the breast. Mammography uses low dose X-ray; high contrast, high-resolution film; and an X-ray system designed specifically for imaging the breast. It is estimated, that in one year, 48 million mammograms are performed. The US Food and Drug Administration reports that mammography can find 85 to 90 percent of

breast cancers in women over 50 and can discover a lump up to two years before it can be felt [6]. Computer aided diagnostics in mammography can improve these statistics even further. Other breast imaging modalities include ultrasound, breast magnetic resonance imaging (MRI), nuclear medicine imaging, and ductography.

Researchers and scientists have placed much emphasis in aiding the fight against breast cancer by analyzing mammograms using digital image processing techniques. The main areas of research in the image processing of mammographic X-rays focus on the detection of malignancies and their pre-cursors. Much of the current work is dedicated to the detection of microcalcifications, which are tiny specks of calcium in the breast. Microcalcifications are the most common mammographic sign of ductal carcinoma in situ, which is an early cancer confined to the breast ducts. Almost 90% of cases of ductal carcinoma are associated with microcalcifications. Many image processing algorithms have shown a significant performance in the detection of microcalcifications. Methods used in the detection of microcalcifications include support vector machine learning [7-9], wavelet based analysis [9], texture features [10], and Gaussian filtering [11]. Collections of microcalcifications seen in one area are referred to as a cluster and may indicate a small cancer. Other areas being researched for the detection of malignancies include the detection of macrocalcifications and masses. Macrocalcifications are coarse calcium deposits that are often associated with benign fibrocystic change or with degenerative changes in the breast, such as aging of the breast arteries, old injuries, or inflammation.

The research work presented in this thesis focuses on risk factor analysis. Risk factors represent the *potential* of the patient to develop breast cancer. The American

Cancer Society characterizes risk factors into three broad categories. These three categories include 1) risk factors that cannot be changed, 2) lifestyle-related risk factors, and 3) risk factors with uncertain, controversial, or unproven effect on breast cancer risk. Risk factors that cannot be changed include gender, aging, genetic risk factors, race, and family history of breast cancer. Lifestyle-related factors include bearing children, breast-feeding, alcohol, obesity, and physical inactivity. Factors with unproven effects on breast cancer risk include antiperspirants, smoking, and breast implants. Table 1.1 describes some breast cancer risk factors with their associated relative risk [12]. Knowledge of risk factor statistics is beneficial for the early detection and screening of breast cancer.

TABLE 1.1 – Breast cancer risk factors [12].

Risk Factor	High-Risk Group	Low-Risk Group	Relative risk
Age	Old	Young	> 4.0
Country of birth	North America, Northern Europe	Asia, Africa	> 4.0
Socioeconomic status	High	Low	2.0 – 4.0
Marital Status	Never married	Ever married	1.1 – 1.9
Place of residence	Urban	Rural	1.1-1.9
Place of residence	Northern US	Southern US	1.1-1.9
Race ≥ 45 years	White	Black	1.1-1.9
< 40 years	Black	White	1.1-1.9
Nulliparity	Yes	No	1.1-1.9
Age at first full-term pregnancy	≥ 30 years	< 20 years	2.0-4.0
Age at menopause	Late	Early	1.1-1.9
Weight, postmenopausal women	Heavy	Thin	1.1-1.9
Any first-degree relative with history of breast cancer	Yes	No	2.0-4.0
Mother and sister with history of breast cancer	Yes	No	> 4.0
Mammographic parenchymal patterns	Dysplastic	Normal	2.0-4.0

Studies have shown that, in comparison to other more commonly used risk factors, breast density may be the strongest independent marker for breast cancer risk. It has been shown that a strong positive correlation exists between breast parenchymal density on mammograms and breast cancer risk [13,14,15]. The radiographic appearance

of the female breast can be divided into bright radiodense regions that consist of parenchymal tissue and darker radiolucent regions that consist primarily of fatty tissue. An example of the different regions within a mammogram X-ray is evident in Figure 1.1. The percentage of radiodense tissue in the breast tissue region is known as breast density, mammographic density or radiodensity. The distribution of radiographically lucent fat and radiographically dense connective and epithelial tissues creates a mammographic parenchymal pattern.

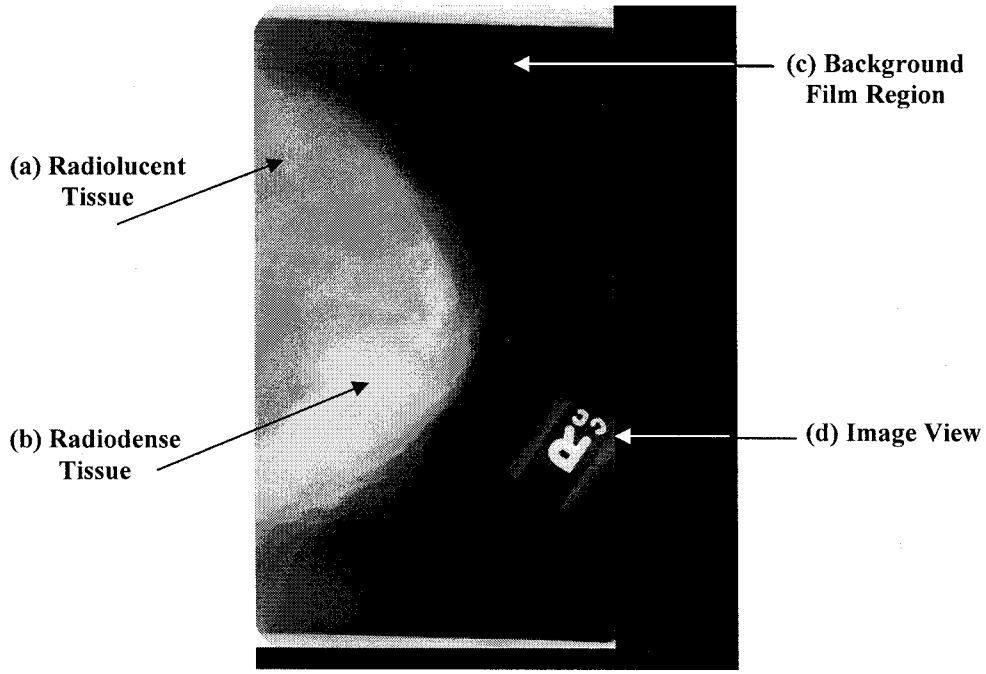

FIGURE 1.1 - Mammogram X-ray with (a) radiolucent and (b) radiodense tissue labeled, and (c) film (non-tissue) region with (d) corresponding image view.

1.2 Mammography Procedure

Mammography is one of the best breast imaging modalities available for the early detection of breast cancer in women, when it can be most effectively treated. X-ray mammography is one of the most common procedures performed by radiologists in the screening and diagnosis of breast cancer. During this procedure, the breast is exposed to

a small dose of radiation to produce an image of internal breast tissue. A conventional mammography process is shown in Figure 1.2 [16]. The image of the breast is produced as a result of some of the X-rays being absorbed, through attenuation, while others pass through the breast to expose the film. The differences in absorption of various types of tissue and the corresponding varying exposure level of the film create the images that clearly show normal structures such as fat, fibroglandular tissue, breast ducts, and nipples. The term fibroglandular has been used to describe the structures of both fibrous and glandular tissue. Abnormalities such as microcalcifications, masses, and cysts are also visible. Breast masses (including benign and cancerous lesions) appear as white regions on mammogram film whereas fat appears as black regions on a mammogram film. Everything else (glands, connective tissue, tumors and other significant abnormalities such as microcalcifications) appears as levels of white on a mammogram. The assessment of radiographic pattern of the breast is based on the amount and distribution of radiodense breast parenchyma (composed of fibrous stroma and epithelial, glandular elements) in radiolucent fatty tissue. The differences seen among different women in mammograms are due to differences in the relative amounts of fat, connective and epithelial tissue, and the different X-ray attenuation characteristics of these tissues and are referred to as the parenchymal patterns of the breast [17].

A specially qualified radiologic technologist will position the female breast for proper imaging. The Mammography Quality Standards Act (MQSA), passed by Congress in 1992 and administered by the Food and Drug Administration, requires facilities to meet specific standards of quality in order to offer mammography. The breast is first placed on a special cassette and compressed with a paddle. This tissue

compression is necessary in order to even out the breast thickness so that all of the tissue can be visualized. Both the size of the breast and the woman's age may contribute to the apparent variation in thickness due to the tissue compression on the mammograms [18]. A mammogram is an X-ray image of a breast taken from one or more views [19]. Typically, the mammography procedure produces a set of four X-ray films. An example of this X-ray film set is shown in Figure 1.3. The X-rays are of the craniocaudal (CC) and mediolateral oblique (MLO) views of both breasts.

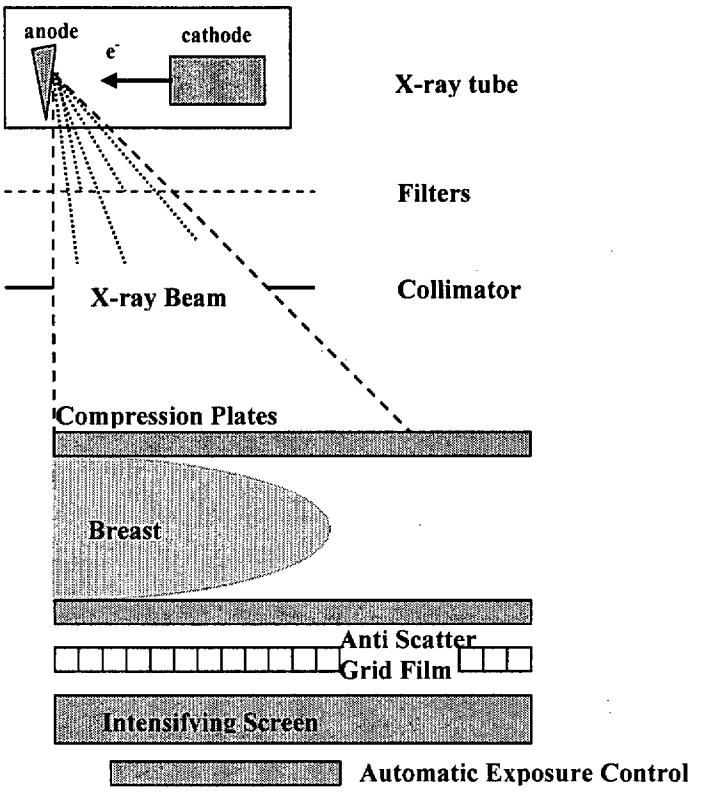

FIGURE 1.2 - Conventional mammography process from [16].

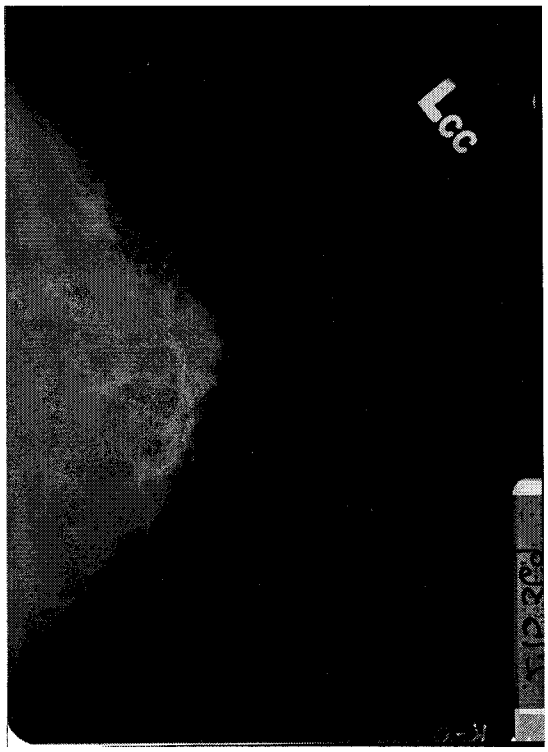

Left Craniocaudal (LCC) View

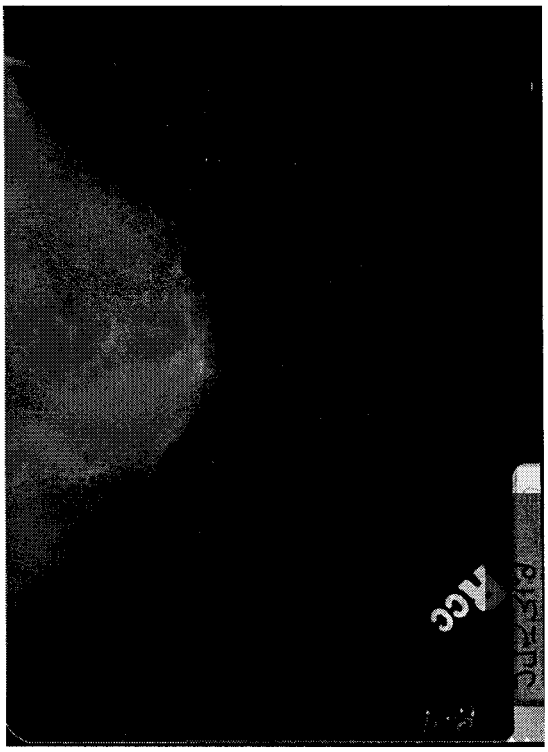

Right Craniocaudal (RCC) View

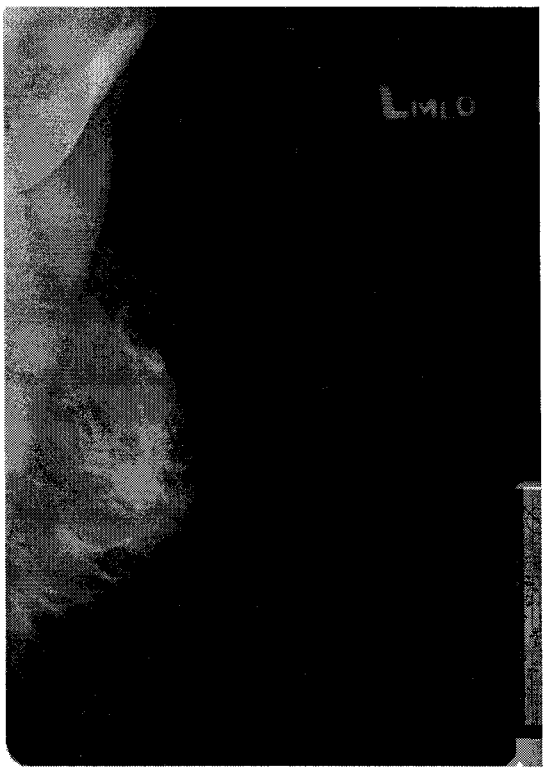

Left Mediolateral Oblique (LMLO) View

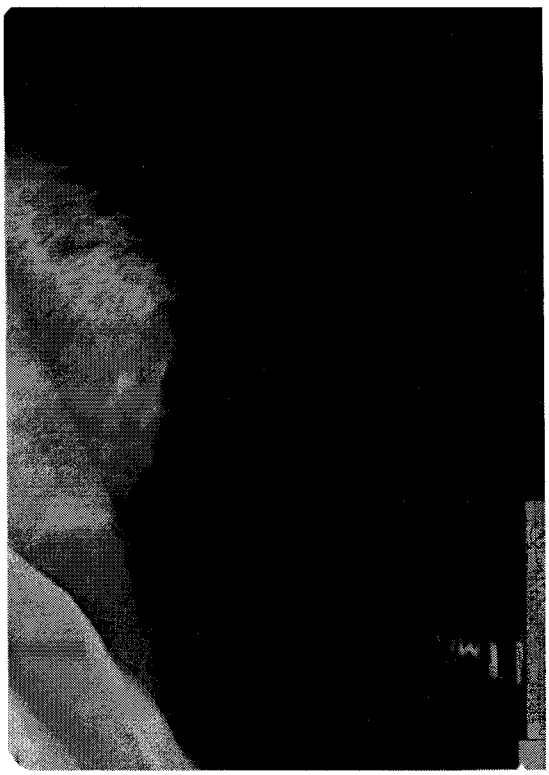

Right Mediolateral Oblique (RMLO) View

FIGURE 1.3 - Typical mammogram X-ray film set.

The mediolateral oblique view is taken from an oblique or angled view. This MLO view is preferred over a lateral 90-degree projection because more of the breast tissue can be imaged in the upper outer quadrant of the breast and the axilla (armpit). The pectoral (chest) muscle should be depicted obliquely from above and visible down the level of the nipple to further down. The shape of the muscle should curve or bulge outward as a sign that the muscle is relaxed; the medial (middle) portion of the breast should be prominent in the MLO view. The variation of angle is needed because the shape of the pectoral muscle is various.

The craniocaudal view images the breast from above. With the CC view, the entire breast parenchyma should be depicted. As with the MLO view, tissue compression is applied to spread the breast tissue involving the parenchyma.

Although much of the X-ray capture process is now automated, proper positioning and tissue compression of the patient's breast by the technologist is essential to capturing a useful set of mammogram films. Most serious and frequent errors are due to improper positioning [20]. After the mammogram is taken, a trained radiologist traditionally performs the diagnosis of the X-rays. The radiologist is typically concerned with the presence of immediate dangers to the patient, malignancy and other abnormalities. A highly dense breast is a concern because of the complexity it adds to the diagnostic process and due to the emergence of breast density as a risk factor for developing breast cancer.

Studies have been performed to measure the inconsistency of radiologists in screening mammography [21]. It is stated in this study that the amount of inconsistency in interpretation among radiologists varies across different types of analysis in screening

mammography. The degree of disagreement in radiologists' estimations is subjected to factors including mammographic features specific to the breast, features specific to the case, and naturally occurring differences among observers.

1.3 Statement of Problem

The quantification of radiographically dense tissue, referred to as breast density, has been shown to be one of the most robust markers as a risk factor for the development of breast cancer. Current methods designed to quantify this tissue are prone to both inter- and intra-observer variability. This variability is present because of the subjective decision making of the trained radiologist. The development of an objectively designed automated method to quantify the amount of breast density is necessary to eliminate the effects of inter- and intra-observer variability.

The design of this automated system will incorporate typical evaluation skills present in a trained radiologist during the segmentation and quantification of radiodense tissue. This evaluation includes the differentiation in gray-level values of tissue defined as radiolucent or radiodense. The radiologist also incorporates the fact that tissue compression has occurred during the mammography procedure. Tissue compression is necessary during the mammography procedure for a number of reasons. The breast tissue must be compressed so that there is a lesser amount of tissue overlap leading to a better visualization of the internal structure of the female breast and any potential abnormalities. Other reasons include reducing overlapping normal shadows, allowing the use of a lower X-ray dosage, and immobilizing the breast to eliminate image blurring cause by motion. According to the American College of Radiology and the Breast Imaging Reporting and Data System (BI-RADS), breast tissue is heterogeneously dense within a mammogram

because the breast is almost entirely flat due to the compression plates [22]. The gray-level values of the two types of tissue will differ with respect to the amount of tissue compression that has occurred at any particular location within the digitized mammogram.

A major effect of tissue compression is the creation of "artificial density." It has been shown that dense tissue appears relatively bright on a digitized mammogram. At the chest wall, where tissue compression is the highest, the greatest amount of tissue will be compressed into a smaller amount of space. Evaluation of the digitized mammogram must account for the appearance of radiographically dense tissue in regions closer to the chest wall may actually only be a result of artificial density caused by tissue compression and must be disregarded as being quantified as radiodense tissue. The research presented here addresses these issues and advances the state of the art techniques in building an automated system to segment between radiodense and radiolucent tissue indications.

1.4 Scope and Organization of the Thesis

This thesis introduces a novel algorithm for the automated segmentation and quantification of radiodense tissue in digitized mammograms. This technique incorporates methods of quantifying radiodense tissue that are consistent with those methods used by trained radiologists in the quantification process. Methods used in the development of this algorithm include:

1. A radial basis function neural network used to extract the breast tissue region from a digitized mammogram;

2. A constrained Neyman-Pearson algorithm to generate a global threshold to distinguish between radiodense and radiolucent tissue indications;
3. Parametric models for tissue location developed to analyze tissue in accordance with the location within the digitized mammogram;
4. Variation of the threshold using parametric models to minimize artifacts induced by tissue compression.

The proposed algorithm has been exercised on mammogram images obtained from the Channing Laboratory of the Brigham and Women's Hospital and Harvard Medical School. Results presented in this thesis have been validated by independent assessments from an experienced radiologist using a previously established method for quantifying radiodense tissue. This research is intended to support an investigation being conducted at Fox Chase Cancer Center (FCCC), examining the correlation between dietary patterns and breast density.

This thesis is organized as follows; this introduction is followed by a background investigation of mammography and an extensive literature survey of previous breast density estimation techniques in Chapter 2. Chapter 3 presents an analysis of techniques from random variable theory that is employed towards an automated technique to segment radiodense tissue. The overall approach proposed for automatically segmenting radiodense tissue in digitized mammograms is presented in Chapter 4. In Chapter 5, the results are presented from implementing the algorithm on the digitized mammogram images. Finally, a summary of the work is provided along with identifying future research directions in Chapter 6.

CHAPTER 2: BACKGROUND

Several methodologies have been developed to quantify breast density in mammogram X-rays. This chapter describes, in detail, many of these methods, ranging from when breast density was first described as a risk factor for breast cancer, to current automated techniques to quantify breast density.

2.1 Breast Density

Studies by J.N. Wolfe proposed that a correlation is prominent between mammographic parenchymal patterns and the risk of developing breast cancer [23,24]. This finding produced many studies to look further into the association between mammographic fibroglandular density and the related breast cancer risk. Many of these studies supported Wolfe with a similar relationship between parenchymal patterns and breast cancer risk [13,25-35]. Breast density is loosely defined as the amount of connective tissue and glandular tissue within the breast. One study in particular showed that women with a breast density of 75% or greater were at a risk of developing breast cancer five times greater than women with little or no breast density [13]. Boyd *et al* demonstrated the heritability of breast density, concluding that finding the genes responsible for this phenotype may be a significant step in understanding the pathogenesis of breast cancer [36]. The investigators of the heritability study analyzed nearly 1 000 pairs of female monozygotic (identical) and dizygotic/fraternal (non-identical) twins in North America and Australia. Readers who were blinded to the identity of the women computed mammographic densities. The percentage of dense breast tissue was correlated twice as strongly among monozygotic twin pairs than among dizygotic twin pairs, indicative of a finding that is consistent with an additive genetic cause. Methods have been developed

and experimented with to quantify breast density. This chapter presents a description of these methods.

2.1.1 The Wolfe Classification

The Wolfe classification was proposed in the mid 1970s to identify groups of women at high risk for breast cancer [23,24]. This is a four-class classification, where classification is dependent on the relative amounts of fat, epithelial and connective tissue densities and prominent ducts present in the mammogram. These four classes, called Wolfe patterns, are defined as:

a. *N1*: The breast is comprised entirely of fat.
b. *P1*: The breast has up to 25% nodular densities.
c. *P2*: The breast has over 25% nodular mammographic densities.
d. *DY*: The breast contains extensive regions of homogeneous mammographic densities.

Wolfe proposed these mammographic parenchymal patterns as a marker for the prediction of breast cancer and associated them with a stepwise increase in breast cancer risk. *N1* is indicative of a breast containing parenchyma that is radiographically lucent and the risk for developing breast cancer is at a relative minimum. *DY* is indicative of a breast containing parenchyma that is radiographically dense and the risk for developing breast cancer is at a relative maximum. The Wolfe classification was popular for many years due to the advantages created in that observers have the ability to quickly classify mammograms, but there are a number of limits to this method. Wolfe's initial descriptions of the classes were brief and this leads to the classification of mammograms to a broad analysis introducing a lack of uniformity between different observers. This

introduces a high amount of variability in the risk estimation [37]. The problem of inter-observer variability is also evident because the radiologists' subjective assessment is used to classify a mammogram into a particular Wolfe pattern. Because of these limitations, other methods of quantifying breast density have been researched.

2.1.2 Breast Imaging Reporting and Data System (BI-RADS)

As recommended by the American College of Radiology, the Breast Imaging Reporting and Data System (BI-RADS) have incorporated a four-category classification scheme for mammographic density [22]. These classifications include:

a. The breast is almost entirely fat.
b. There are scattered fibroglandular densities.
c. The breast tissue is heterogeneously dense. This may lower the sensitivity of mammography.
d. The breast is extremely dense, which could obscure a lesion on mammography.

These classifications are defined so there can be a concise report of the overall breast composition. Radiologists typically estimate the breast density on mammograms in clinical practice based upon this BI-RADS classification. This classification method is affected by the inter-observer variability among different experienced radiologists performing the analysis.

2.1.3 Six-Category Classification

Particular studies of breast density rely heavily on the categorization of breast densities. Previous classification schemes for breast density are sometimes too broad for the research in these studies. One particular study enhanced this categorization of breast

density into six different categories [38]. These categories rely on the percentage of the breast volume occupied by ductal prominence or mammographic dysplasia (abnormal development of tissue) and are estimated through visual inspection by a trained radiologist. The mammogram was defined as being 0 %, > 0 to < 10 %, 10 to < 25 %, 25 to < 50 %, 50 to 75 %, or 75 to 100 % dense. While this method of classification is more precise than the previous four category methods, this is still hindered by the inter-observer variability. Also, the radiologist is approximating the area of the breast to calculate the percentage of radiodense tissue within the mammogram, which can become a source of error due to the irregularity of the shape of the breast. There is a need to develop an automated and quantitative estimation that is not susceptible to the inter-observer variability.

2.2 Semi-Automated Segmentation Techniques

The Wolfe classification scheme, the ACR-BIRADS method, and the six-category classification are all entirely dependent upon the expertise of the expert performing the classification. The definition of breast density is loosely defined, therefore, a method must be developed to allow a consistency among the expert observers.

2.2.1 Interactive 'Toronto' Method

Yaffe, Boyd *et al* developed the popularly used interactive software program to identify regions within a mammogram that appear as radiodense [39,40]. This program imports any given mammogram onto the computer screen to perform manual segmentation between radiodense and radiolucent tissue. The digitized mammogram is quantified to

4096 (2^{12}) discrete grayscale levels per pixel. The radiologist using the program then segments the image into three regions: (1) the film region outside the breast tissue area, which is information that is not important for the study of breast density, (2) the area within the breast tissue which appears as radiolucent, and (3) the area within the breast tissue which appears as radiodense.

The radiologist selects two threshold gray-levels with the aide of a computer trackball or mouse. The movement of the mouse relates to a positioning of a slider, which is representative of the 4096 possible gray-levels. As the user moves the mouse, the gray-level threshold is increased and the effective segmentation is visually depicted on the computer screen. The first gray-level threshold chosen will distinguish the edge of the breast tissue region, differentiating between breast tissue and the outside film region. When the threshold selection is sufficient and the breast tissue region is secured, the next step is to select an additional gray-level threshold to identify regions within the breast tissue as either radiodense or radiolucent. This second threshold is chosen in a similar method as the initial threshold, however this choice is dependent upon the expertise of the radiologist. This method is referred to as the "Toronto" method.

It is mentioned that the use of gray-level thresholding incorporates a simple decision rule to maintain a consistency between different radiologists. Also, the difficulty of visually assessing relative area from an irregularly shaped image is minimized. However, a completely automated method is still desired to eliminate any subjective decision regarding the choice of the radiodense regions.

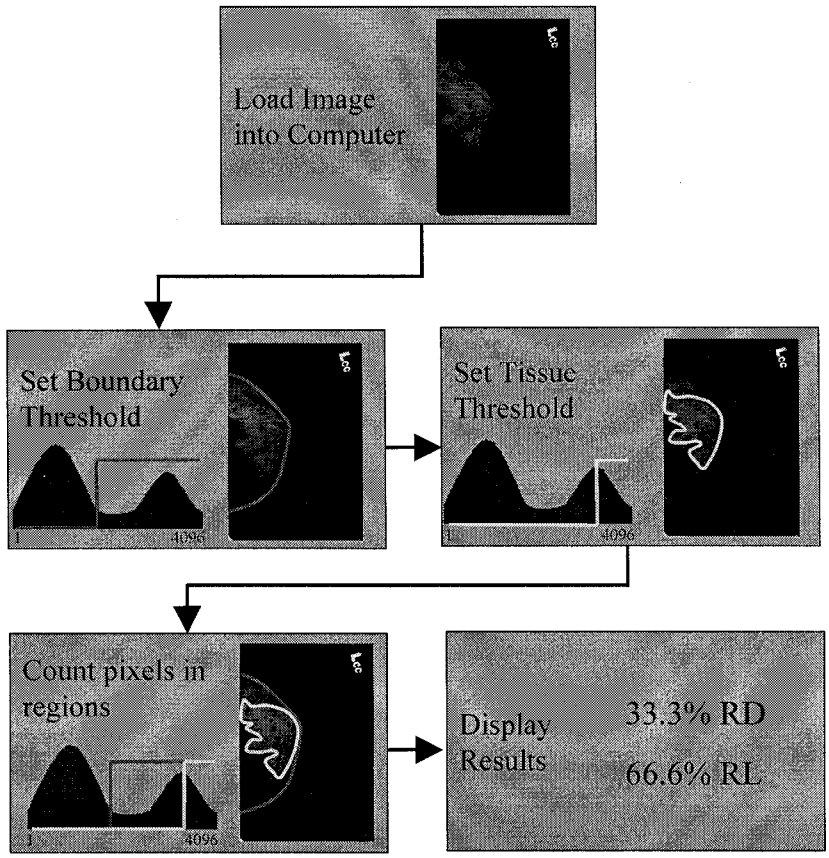

FIGURE 2.1 - Block diagram of the Toronto interactive computer method for determination of radiodense tissue percentages. This method uses two grayscale thresholds to determine tissue/film boundary and radiodense/radiolucent boundary.

2.2.2 Magnetic Resonance Imaging and Breast Density

The quantification of breast density has also been performed incorporating the use of magnetic resonance imaging (MRI) [41]. To obtain the MRI of the breast, patients were scanned lying in the prone position containing two figure 8 surface coils, one placed above the other. Using a rigid imaging device, the breast was scanned for 1 pass of the breast in the cranial to caudal direction with constant thickness (ranging from 4,5,6 or 7 mm). A program was developed to calculate the mammographic density using the MRI slices. This program is similar in methodology to that of the Toronto method. However, it is mentioned that this method cannot be used to predict the glandular percentage of

patients due to the poor correlation of skewness calculated within the histogram of the radiodense tissue with the MRI glandular percentage calculated by a trained radiologist. In addition, there is no single, standardized and generally accepted technique for all breast MR imaging examinations [42].

2.3 Automated Segmentation Techniques

A common hindrance seen by many of the semi–automated techniques is due to the interaction of the observer. This interaction creates inter- and intra- observer variability that is prone to error. Development of a fully automated technique will minimize this error. Table 2.1 summarizes the automated segmentation techniques to quantify radiodense tissue.

2.3.1 Adaptive Fuzzy K-means

A technique to automatically quantify the amount of mammographic density in a digitized mammogram has been developed by Lou and Fan [43]. This process incorporates an adaptive histogram equalization technique along with an adaptive fuzzy K-means technique to classify pixels as radiodense. Groupings of pixels are classified with dependence on the mean of that particular grouping. Among a database of eighty-one mammogram images, the average error for correct classification of radiodense tissue was 7.98 %. Also, this technique only requires a process time of eighteen seconds per image.

2.3.2 Rule Based Histogram Classifier

Zhou et al. developed a rule based histogram classifier to determine the amount of dense area within a mammogram [44,45]. Dependent upon characteristics of the histogram of the mammogram image, it will be classified into one of the four BI-RADS breast density ratings. After the mammogram is correctly classified, a threshold is developed by use of a discriminant analysis method or a maximum entropy principle method. Selection of the method to use for thresholding relies on which of the four categories the mammogram is classified into. Results showed a maximum difference of 20% between their estimates against the expertise of two radiologists. However, they conclude that the subjectively estimated percent dense area between the two radiologists differed by as much as ±20%. This indicates the need to develop an objective method for the estimation of breast density.

2.3.3 Classification using Texture Analysis

A method is incorporated with the idea that different image processing algorithms are more suitably applied to the separate classes of mammograms in terms of their density similar to the ACR BI-RADS classification [46]. Using texture measures, mammograms are classified into one of the four different density classes, thereby reducing any subjectivity introduced from the analysis of the radiologist. Three methods are employed for determining texture including features obtained from Spatial Grey Level Dependency (SGLD) matrices, fractal dimension, and statistical gray-level measures.

TABLE 2.1 – Summary of automated segmentation techniques in breast density analysis.

Proponents	Approach	Advantages	Disadvantages
Lou and Fan [43]	Adaptive fuzzy K-means technique to classify pixels as radiodense.	7.98 % error among 81 mammogram images. 18 seconds process time per image.	Effects of tissue compression are ignored. Small dataset.
Zou et al. [44,45]	Rule based histogram classifier	Maximum difference 20% from expert analysis.	No object method for validation.
Bovis and Singh [46]	Classification using texture analysis.	91 % correct classification.	Relies on knowledge of the region to be segmented. Classifier is based on simplistic measures of texture.
Saha, Udupa, et al. [48]	Scale-based fuzzy connectedness models	Estimates correlate strongly with analysis by radiologist.	Does not automatically exclude pectoral muscle.
Byng, Boyd, et al. [51]	Fractal dimensions and regional skewness	Strong correlation between these image properties and breast density.	Required interaction to segment breast tissue region from rest of mammography film.
Neyhart et al. [53]	Constrained Neyman-Pearson decision function	Automated technique.	Model does not cover the entire range of radiodense tissue; effects of tissue compression are ignored

The SGLD matrices model the correlation between pixels within the breast region. The SGLD matrix is the joint probability occurrence of gray-levels i and j for two pixels with a defined spatial relationship in an image. Calculating some measure of scatter of the SGLD matrix around the main diagonal will analyze the texture coarseness. At end, fifteen statistical measures are extracted from this SGLD matrix. The fractal dimension is calculated for every pixel in the region and the mean value over all pixels is

used as the fractal dimension feature. Statistical features used in this study include the mean, homogeneity, standard deviation and skewness of grayscale values of the breast tissue region.

The data calculated through the three methods are identified as being 'dense', 'glandular' or 'fatty' by using supervised learning techniques on different types of classifiers. The best results were obtained using a K-Nearest neighbor classifier, resulting in a 91% recognition rate. Classifier performance was evaluated on the basis of cross-validation and the use of receiver operating characteristic (ROC) statistics. Results will be more precise with further research on the use of prior knowledge of the breast type at different stages including enhancement, segmentation and feature extraction. Two basic weaknesses of image-based textural approaches include [47]:

1. Radiologists analyze texture variations in a complex and subtle manner and classifiers based on simplistic measures of texture do not perform well.
2. The differences in imaging conditions lead to a non-rigid variation in the mammographic intensity distribution a fact that diminishes the possible use of texture for mammographic pattern recognition.

2.3.4 Scale-Based Fuzzy Connectedness

An automated method has been developed by researchers at the University of Pennsylvania using the notion that breast density can be quantified through the principles of fuzzy connectedness [48]. This method relies on the idea that artifacts such as noise, blurring, and background variation along with material heterogeneity cause object regions within an image to exhibit a gradation of intensity values in the image. Human

observers usually do not have difficulty in analyzing the object regions as an integrated whole. Image elements in these object regions seem to hang together to form the object region independent of their gradation of values. To address the issues of hanging togetherness and graded composition, these researchers have developed their algorithm based on fuzzy relations. They define a fuzzy affinity, which is intended as a local relation among neighboring pixels. The higher the strength of this relationship, the more these pixels correlate with each other.

A "fuzzy connectivity scene" is first generated using their algorithm. This scene is representative of the likelihood that a particular region is to be associated with a designated reference region. Knowledge of the estimation of the parameters of the region that is to be segmented is required. The algorithm is exercised on the localized breast tissue region. The reference region is assigned to the highest 32% of intensities within the histogram of the localized breast tissue region. A fuzzy connectivity scene is created for the dense region of the breast tissue and segmented using an automatic threshold selection method.

This method works automatically except for the exclusion of the pectoral muscle when trying to localize the breast tissue region. Estimations of the amount of breast density within a mammogram produced by this research correlates strongly with the estimations seen by a trained radiologist.

2.3.5 Regional Skewness and Fractal Dimension

Fractal geometry was originally presented by Mandelbrot [49]. This theory allowed for the description of complex shapes where normal Euclidian geometry fell short. Using

fractal geometry, the dimension (similar to spatial dimension) of an object can be calculated. This dimension is a measure of the complexity of an object. When analyzing images, fractal dimension can be used to estimate the smoothness of an image when the image intensities are mapped like a terrain. Reported results show a strong negative correlation between breast density and fractal dimension. Thus indicating that mammograms of high radiodense tissue are smoother (i.e. more similar) and those of lower radiodense tissue are more rough (i.e. more dissimilar) [50].

Regional skewness is a measure based on third moment histogram analysis. The histogram of an image is a graph of the quantity of pixels in an image that are of the same value or range of values [50]. The histogram information is irrespective of pixel position and can provide a great deal of information about an image. Information on the skewness of an image is given by the third moment of the image histogram. The method presented used a normalized third moment. It was hypothesized that if a region contains mostly fatty tissue, which is inherently lower in gray-level intensity, then it will exhibit a positive skewness. Conversely, those regions that are of a more radiodense nature, which are inherently higher in gray-level intensity, will indicate a negative skewness. To provide better resolution, analysis was done using non-overlapping groups of pixels and averaged to provide a single skewness measure. Analysis of this value revealed a strong correlation between skewness and breast density [51].

Although promising results were obtained using both of these means, no quantitative measures of breast density using these techniques were presented. Furthermore, no system for the automatic calculation of the values was presented. The skewness measure required significant user interaction.

2.4 Symmetry of Views

The typical mammography procedure produces a film set of four different views of the breast. This film set includes views of the CC and MLO for both the left and right breast. The pectoral muscle is included in the MLO view. The inclusion of the pectoral muscle presents a difficult challenge for automatic segmentation. A study has shown that the separate analysis of the MLO and CC views result in similar quantifications of breast density [52]. This finding allows for the study to be sufficient of only one single view per breast, eliminating the additional work and cost of digitization, storage and analysis of the mediolateral oblique views. To ensure the efficiency of an automatic segmentation process, analysis can now be performed only on the CC views of both the left and right breast per X-ray set.

In this chapter, an overview of previous research work in the area of quantification of breast density has been presented. This has shown the progression of the methods over the years. Currently, the most popular method in practice has been the "Toronto" method for the segmentation of radiodense tissue and will be used as a baseline for the comparison of results produced through the methods developed in this thesis.

CHAPTER 3 : MODELING AND SEGMENTATION OF GAUSSIAN RANDOM IMAGES

3.1 Introduction

An automated technique to segment breast density in a digitized mammogram has been previously developed at Rowan University and is described in detail in [53-57]. This technique was developed using the fundamentals of image modeling. The foundations of image modeling and this automated segmentation technique are discussed in this chapter.

3.2 Image Modeling

The application of this automated segmentation technique requires that the image can be modeled mathematically. Recasting the image as a random field is the first step in this approach. A two-dimensional image can be modeled as a Gaussian random field by the equation

$$f(x,y) = m_f + \sigma_f w(x,y) \tag{3.1}$$

where $f(x,y)$ is the gray-level value in the image at location (x,y), m_f and σ_f are the local mean and standard deviation of $f(x,y)$, respectively, and $w(x,y)$ is a zero-mean, unit variance, Gaussian random field. This prediction holds true if two criteria are met:

(a) The image, f(x,y) is stationary, and

(b) The local region being modeled is relatively small.

When both of these criteria are met, any image can be modeled as the collection of zero mean, unit variance Gaussian random fields that have been scaled and translated along the real number line using local means and variances.

The image being modeled for this research is a digitized mammogram image. The original digitized mammogram, of size 926 x 676 pixels, is subdivided into blocks of

size 8 x 8 pixels; the local mean and standard deviation for the gray-levels are estimated for each of these blocks. This modeling is illustrated in Figure 3.1.

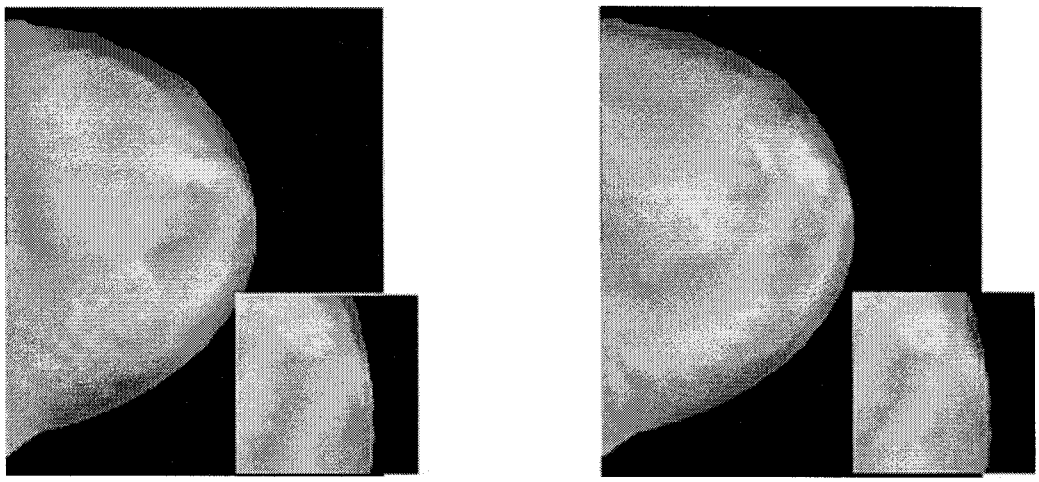

(a) (b)

FIGURE 3.1 - (a) Original digitized mammogram image and (b) its Gaussian random model. Included are the 8 x 8 subdivided blocks used in the modeling process.

This theory shows that an image, if it is Gaussian in nature, can be automatically and dynamically segmented about the mean of its probability density function (PDF) to divide the image into 'dark' and 'bright' regions. The mammogram images have been successfully modeled as a Gaussian random field using its gray-level statistics. The radiodense tissue segmentation can now be recast as a problem in hypothesis testing. In a detection problem, an observation of a random variable is used to make decisions about a finite number of outcomes [2]. In this case, the pixel gray-level under consideration, $f(x,y)$, is the random variable, and the two possible outcomes for that gray-level include radiodense or radiolucent tissue. This two-class situation is also known as binary hypothesis testing. To test the hypothesis, the value of the random variable (pixel gray-level) is compared with a threshold (the mean of the PDF). This threshold is dynamically

generated, taking into account the variation in gray-level statistics from image to image and the local statistics within each image.

3.3 Random Variables

The Gaussian random variable is chosen as a good candidate for the modeling of the different portions of tissue that are present in the mammogram, including radiodense and radiolucent tissue. The cumulative distribution function (CDF) of the Gaussian random variable is given as

$$F_x(x) = \frac{1}{1 + e^{-\frac{(x-m)^2}{2\sigma^2}}} \tag{3.2}$$

where the mean, m, is any real number and the variance, σ^2, is any positive real number. Figure 3.2 (a) shows the plots of the Gaussian CDF over a range of inputs, x. The CDF is capable of mapping a possibly infinitely large range of values onto a set range, [0 1], for instance, as shown in the figure. Differentiating the CDF produces the probability density function (PDF) of the Gaussian random variable and is given as

$$f_x(x) = \frac{1}{\sqrt{2\pi\sigma}} e^{-\frac{(x-m)^2}{2\sigma^2}} = N(m, \sigma^2) \tag{3.3}$$

which is often written as $N(m,\sigma^2)$ to denote a density function of the normal variety. The plot of the PDF is given in Figure 3.2 (b). The PDF shows the probability for the outcome of a random experiment. The mean value of the PDF function, m, is the point of highest probability of the function. For the discrete case, this mean value is defined as

$$\mu = \sum_j x_j f(x_j). \tag{3.4}$$

The variance parameter, σ^2, dictates the spread of the function. For the discrete case, the variance is defined as

$$\sigma^2 = \sum_j (x_j - \mu)^2 f(x_j). \tag{3.5}$$

Using the information that can be extracted from a modeled version of an image, mathematically significant decisions can be made about an image. These decisions can be made automatically and dynamically for any image.

3.4 Image Segmentation by Modeling the Threshold as a Random Variable

A threshold must be determined to differentiate pixels that are either to be considered as radiodense or to be considered as radiolucent. If the mammograms were a zero-mean Gaussian random image then threshold would be the exact midpoint of the gray-levels present in the image. However, since these are real images, the threshold must be dynamically determined. The segmentation threshold is varied across the entire grayscale range. At each gray-level segmentation, the image is converted to a binary matrix with all pixels above the threshold being assigned the value 1 (white) and all pixels below the threshold assigned to the value 0 (black). The effect of varying the segmentation threshold on the percentage of black pixels in a gray-level mammogram image is shown in Figure 3.2 (a). This plot is consistent with the cumulative distribution function (CDF) of a Gaussian random variable. The probability function (PDF) can be calculated by differentiating the CDF a shown in Figure 3.2 (b). The threshold is chosen as the peak value of the PDF.

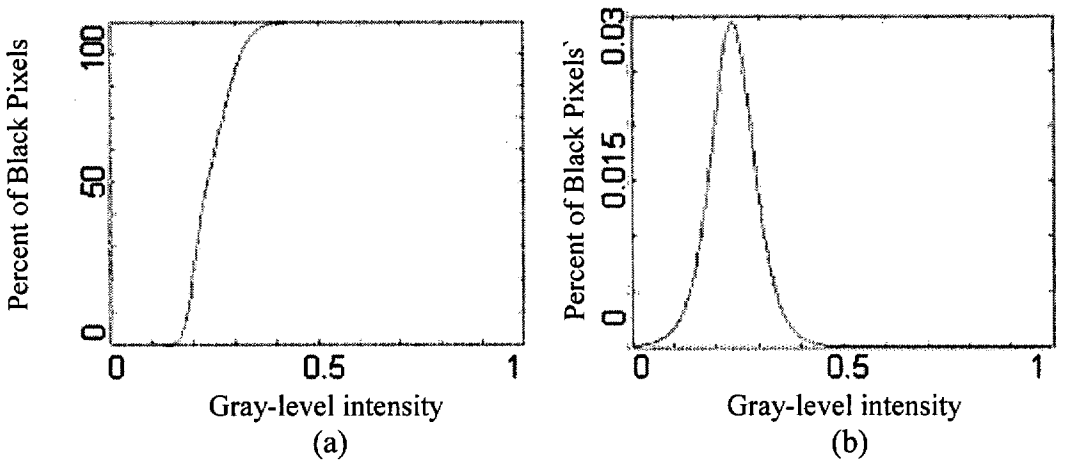

FIGURE 3.2 - (a) Effect of varying segmentation threshold on the percentage of black pixels in a gray-level mammogram image and (b) Probability density function of the threshold random variable.

This resulting threshold chosen from the characteristics of the PDF, T_{global}, is applied to the original mammogram image. Pixels with a gray-level value above T_{global} are radiodense tissue and pixels with a gray-level value below T_{global} are radiolucent tissue. Upon application of this threshold, two distributions are presented that are Gaussian in nature. Pixels below the threshold correspond to the distribution of radiodense tissue pixels and pixels above the threshold correspond to the distribution of radiolucent tissue pixels. Initial assessment of the amount of radiodense tissue produced from T_{global} in comparison to the Toronto method yields poor results [53]. To overcome this issue, a constrained algorithm is enforced that biases T_{global} based upon the local variance of the image and the means of the Gaussian distributions that model the radiodense and radiolucent tissue. The segmentation threshold is now given by the equation

$$T_{CNP} = \frac{\mu_1 + \mu_2}{2} + \left(\frac{\alpha - \sigma^2}{\alpha}\right)\left(\frac{\mu_2 - \mu_1}{2}\right) \tag{3.6}$$

where T_{CNP} is the constrained Neyman-Pearson threshold, α is a scaling parameter, σ^2 is the local variance of the image and μ_1 and μ_2 are the means of the radiolucent and radiodense distributions respectively. Choice of the scaling parameter, α, will allow the threshold chosen to extend between the pure Bayesian classification (midpoint of the two means) and the mean of the radiodense distribution, μ_2. This is a global threshold that is applied consistently to the entire mammogram image to distinguish between radiolucent and radiodense indications. An example of how the threshold is visually depicted is shown in Figure 3.3.

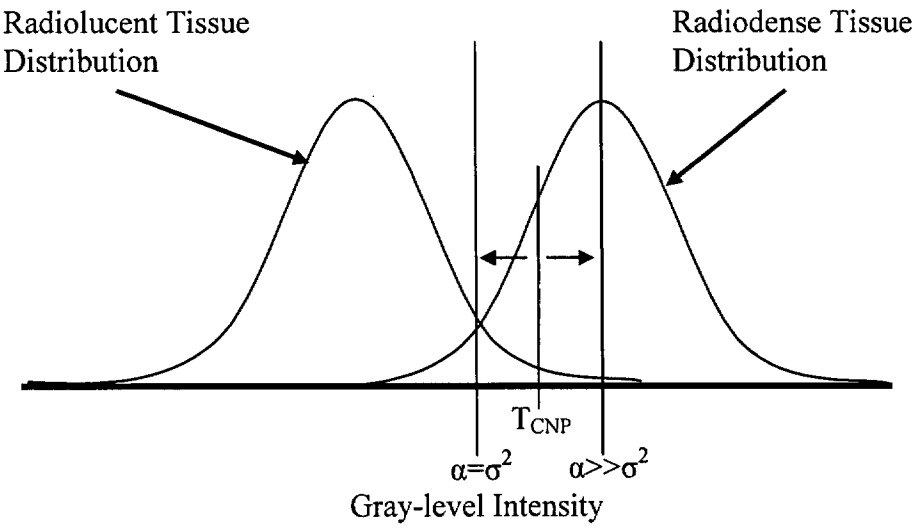

FIGURE 3.3 - Illustration of the constrained Neyman-Pearson classification, indicating the allowance of variation in threshold dependent upon the scaling factor.

This chapter described a method to automatically generate a gray-level threshold to segment between radiodense and radiolucent tissue within a digitized mammogram. This is a global threshold and is applied consistently throughout the entire mammogram. This method of developing a global threshold is referred to as the constrained Neyman-Pearson algorithm (CNPA). However, the effects of tissue compression are not

addressed in the development of this threshold. A method has been developed that can automatically modify T_{CNP} dependent on the physical location of the pixel being analyzed in the mammogram. Allowing T_{CNP} to be modified dependent on location addresses the effects set forth by the tissue compression procedure. This method is discussed in the following chapter.

CHAPTER 4: APPROACH

4.1 Introduction

The overall research approach is shown in Figure 4.1. The approach taken addresses two important issues. The first is the actual segmentation of the arbitrarily shaped breast tissue region from within the rectangular shaped X-ray film. This is an edge detection problem that is accomplished using a radial basis function neural network. After the breast tissue is segmented, radiodense tissue indication within the breast region can be identified and quantified. The challenge here is that gray-level intensities vary from X-ray to X-ray and locally across the same X-ray. This is a threshold estimation problem. The estimation of the threshold will vary spatially due to the artifacts presented by the application of tissue compression during the mammography procedure. Techniques have been developed for dynamically determining a threshold that is capable of segmenting the radiodense tissue.

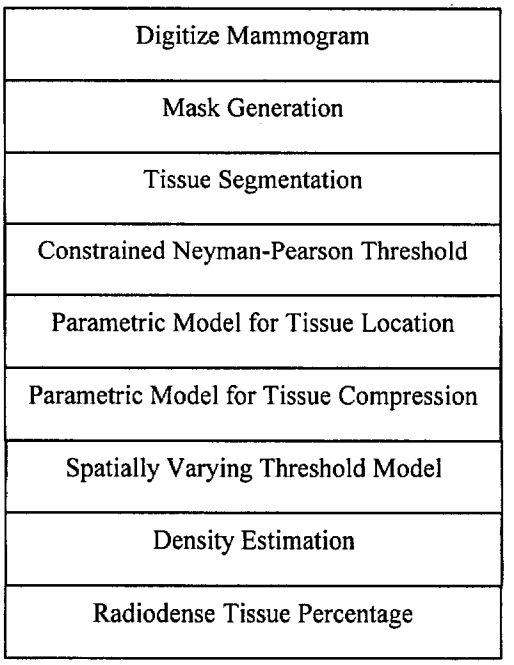

FIGURE 4.1 - Overall approach for the automated estimation of breast density.

This section provides a detailed explanation of the steps developed to implement this research.

4.2 Digitization and Image Pre-processing

The data used for analysis in this research are from two datasets – one obtained from Brigham and Women's Hospital, Harvard Medical School, that was used for algorithm development and the other from the Family Risk Analysis Program (FRAP) at Fox Chase Cancer Center (FCCC), that was used for algorithm validation. The FRAP data includes mammograms of the daughters, mothers and grandmothers of a population of Chinese American women. Each mammogram set contains the four typical X-ray films; cranio-caudal (CC) and mediolateral oblique (MLO) views of the left and right breasts. The CC view is projected down and the breast is compressed horizontally while the MLO view is projected across the breast that is compressed parallel to the pectoral muscle. In the study and application of mammographic density quantification, representative information is provided in a single view, allowing analysis to occur only on the CC views and not on the MLO views. This eliminates the task of excluding the pectoral muscle in the MLO views. All X-ray films are digitized at 500 dots per inch (dpi) using an Agfa medical-grade film scanner. This resolution is chosen to be consistent with existing digital mammography databases. The digitized image was encoded using 8-bit resolution, allowing 256 different gray-levels. An online database was created for managing (storage and retrieval) digitized mammogram images at Rowan University. This database, maintained at Rowan University, uses Macromedia ColdFusion 5.0 and allows for secure password-protected access for project team members. The digitized

mammograms are indexed using FCCC patient ID, age and date of when the mammogram was performed. A priori information such as patient name and patient age are not included.

One of the preliminary steps in the analysis of these images is to map the 8-bit intensity value from the scanner to associated gray-level intensities. Every picture element (pixel) of the data was assigned one of 256 gray-level values ranging from 0 (black) to 1 (white). Orientation of the image to aid this automated analysis requires the breast region to be aligned on the left side of the digitized mammogram.

4.3 Mask Generation

There are two major regions of interest for this research within a digitized mammogram: the breast tissue region and the outside film region. The breast tissue region includes relatively important information while the outside film region contains information disregarded as noise. The information disregarded as noise includes features such as the directly exposed area, patient identification information, and lead markers. To properly quantify the amount and percentage of radiodense tissue present in the breast, there needs to be a technique for separating the tissue region of the X-ray from the film region.

A segmentation algorithm will distinguish the difference between the tissue region and the film region in the digitized mammogram. This is accomplished by generating a segmentation mask to be used to separate the tissue region from the film region. The segmentation mask template is a binary matrix of size equal to that of the original image. The segmentation algorithm described below determines which pixels of the image are representative of the breast tissue region, and assigns the value 1 (white) to

the corresponding regions of the matrix. The rest of the matrix, representing the non-tissue region, is set to 0 (black). This will essentially retain the entire breast tissue region while suppressing the outside film region. This process allows subsequent identification of radiodense regions in the image by concentrating on the tissue region only. Figure 4.2 (a) shows a typical image and 4.2 (b) shows the associated automatically generated segmentation mask. A previous attempt at the segmentation mask generation using a wavelet-based method did not provide sufficiently smooth contours [54].

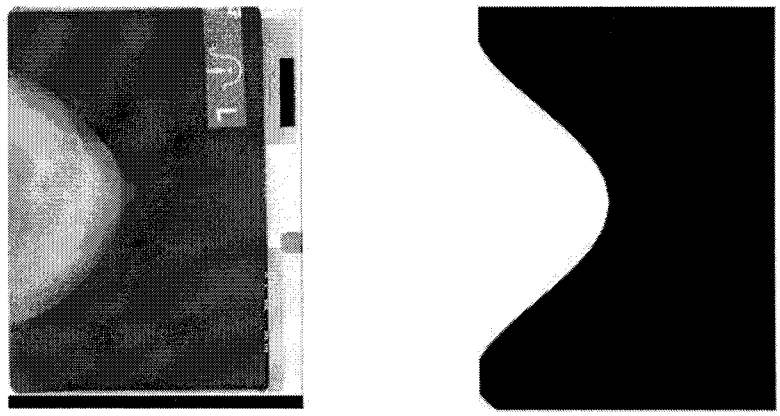

(a) (b)

FIGURE 4.2 - (a) Typical image and (b) automatically generated segmentation mask.

4.3.1 Generation of the Segmentation Mask

All original digitized mammogram images are 926 x 676 pixels in size. The shape and location of the breast is different on all images due to the interpatient variability in shape and size of the breast along with variability from the mammography procedure, including image contrast, positioning of the breast and amount of tissue compression. The generated segmentation mask must account for all of these differences within the digitized mammograms. Even within the same digitized mammogram, the selection of a global gray-level value to differentiate between pixels representing the tissue regions and

pixels representing the film region will provide poor results. The segmentation algorithm must adaptively and automatically take into account local variations between the tissue region and film region.

The first step of the segmentation algorithm is to perform an adaptive threshold technique. In many cases of digitized mammograms, the background gray-level is not constant, and the contrast of objects varies within the image. In such cases, a threshold that is well suited to one area of the image might work poorly in other areas. In these cases, it is convenient to use a threshold gray-level that is a slowly varying function of position in the image. The image is first divided into sectors of 50 by 50 pixels. The histograms of each sector are analyzed to determine a threshold. All pixels in the sectors producing unimodal histograms were assigned to a value of 0. The histogram would be unimodal either when the sector is solely in the tissue region or solely in the background region. For sectors containing both the tissue and the background region, the histogram will be bimodal and this is representative of the edge of the breast. An example of the histograms indicated in the adaptive threshold technique is shown in Figure 4.3.

The histogram being bimodal is indicative of two distributions being present in the sector being analyzed. This is now a classification problem to distinguish between pixels in that sector being representative of either the tissue region or the background region. Bayes' decision criterion states that given two distributions that are Gaussian in nature, with equal variance but different means, classification of data can be performed using the following minimum distance function:

$$T_B = \frac{\mu_1 + \mu_2}{2} \tag{4.1}$$

where T_B is the segmentation threshold, μ_1 and μ_2 are the means of the distributions for the two classes.

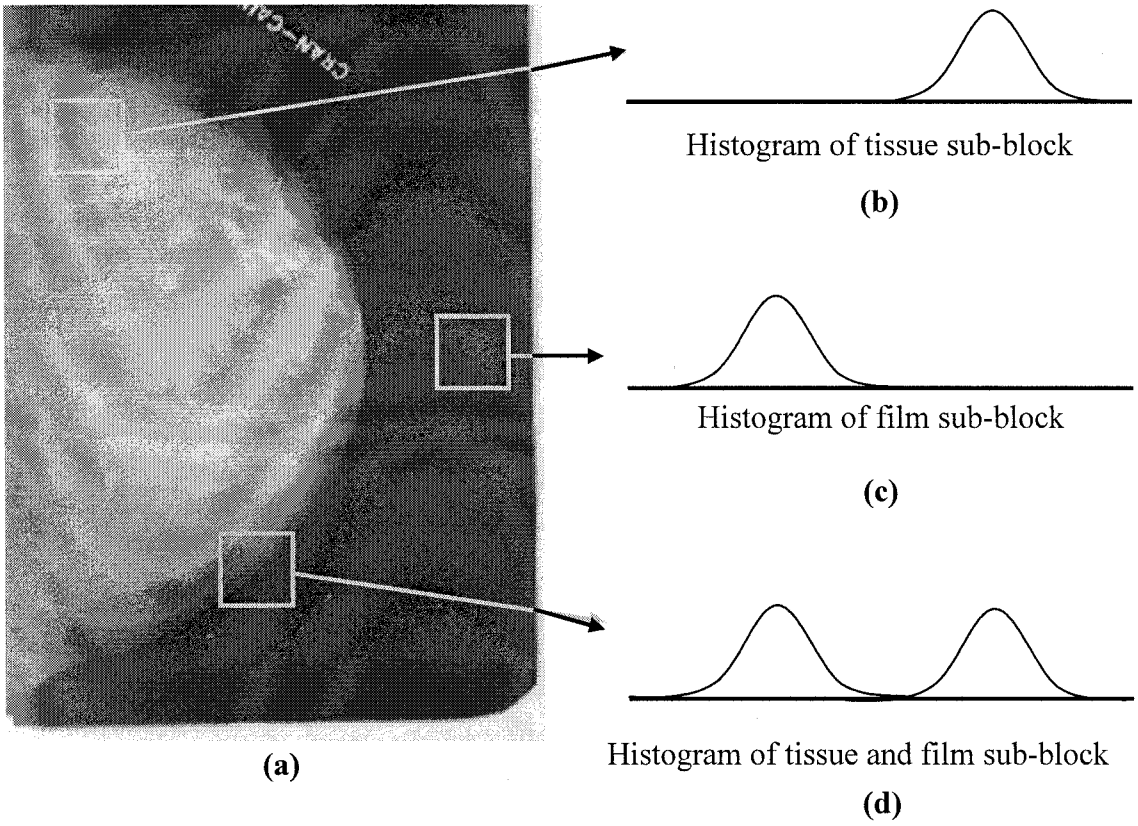

FIGURE 4.3 – (a) Original image showing sectors with (b) the histogram of the tissue region, (c) the histogram of background region, and (c) the histogram of the edge of breast tissue.

For binary classification, the two classes are '0' and '1'. Class '0' represents the members associated with the distribution of mean μ_1. The class '1' representing the pixels associated with the distribution of mean μ_2. Each pixel gray-level value, $f(x,y)$, is compared with the Bayesian threshold, T_B. If $f(x,y)$ is greater than T_B, the pixel is determined to be of class '1' otherwise it is said to be of class '0.' Figure 4.4 illustrates the decision boundary of the Bayesian classifier. Class '1' represents the tissue region while class '0' represents the background region. This methodology will essentially

predict the likelihood that a given sector lies within the breast tissue, within the film, or is the boundary between breast tissue and film.

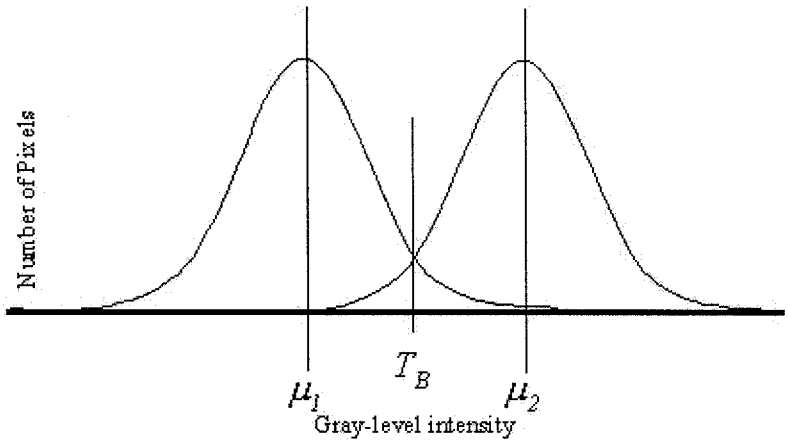

FIGURE 4.4 - Illustration of two distributions with Bayesian classifier segmentation threshold, T_B, labeled. Note the minimization of classification error for both distributions.

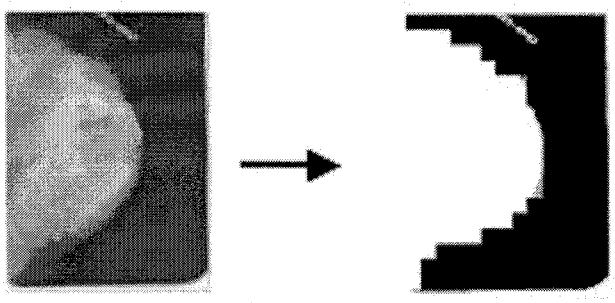

FIGURE 4.5 – (a) Typical image and (b) segmentation mask created after adaptive threshold technique is performed.

However, the segmentation mask generated after the adaptive threshold procedure is a poor representation of the breast tissue region as seen in Figure 4.5. This segmentation mask generates a rough contour as the approximation of the edge of the breast tissue. A smoothing operation will generate a more effective approximation of the breast edge. A radial basis function (RBF) neural network performs well in approximating this rough contour function [58]. There are 926 coarse boundary points in

this current segmentation mask. These boundary points are then sub-sampled and used as the input layer for the RBF neural network. The output of the neural network is an optimal prediction of the breast tissue edge, which is used to generate the final binary segmentation mask. A Gaussian is used as the activation function within the RBF neural network. The RBF neural network essentially applies the activation Gaussian function at all of the input coarse boundary points and sums the entire set of Gaussian functions. This will smooth the coarse function that was generated after the adaptive threshold technique producing a segmentation mask that is representative of the breast tissue region. The RBF neural network is shown in Figure 4.6 along with a typical function approximation using the Gaussian activation function shown in Figure 4.7. Figure 4.8 shows a typical process in the generation of a binary segmentation mask.

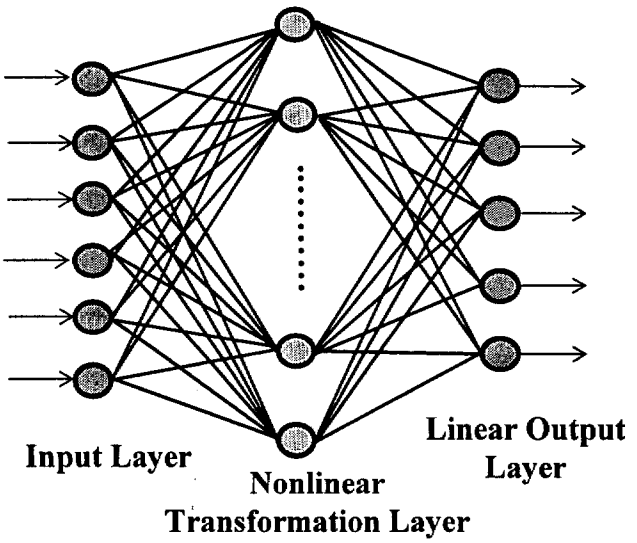

FIGURE 4.6 – Radial basis function (RBF) neural network architecture.

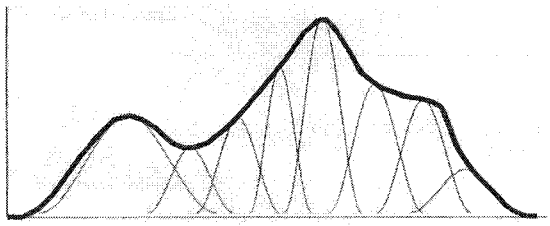

FIGURE 4.7 – Example of function approximation using an RBF neural network [58].

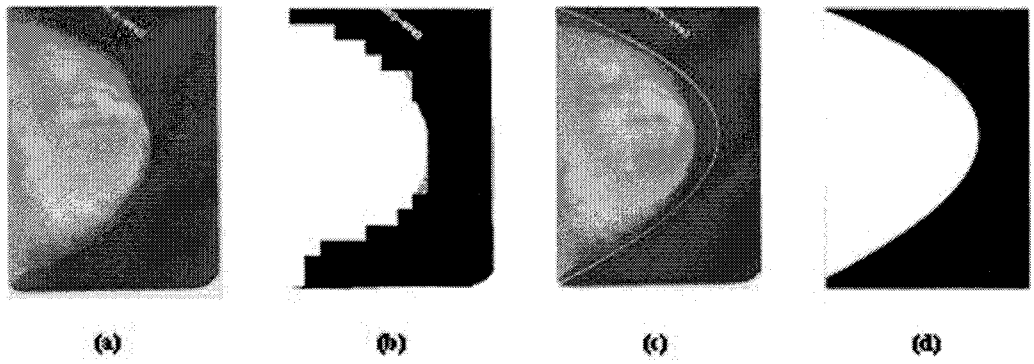

FIGURE 4.8 - (a) Typical image, (b) segmentation mask after adaptive threshold technique, (c) approximation of the edge of the breast tissue using an RBF neural network and (d) automatically generated segmentation mask.

4.4 Tissue Segmentation

The mask generated using the algorithm described above is a binary matrix equal to the size of the original image. Using the above technique the mask matrix is set to a value of 1 (white) in all tissue regions and 0 (black) in all non-tissue regions. The corresponding elements in each array are then multiplied using

$$R_{ij} = O_{ij} * S_{ij}; \quad i=1 \ldots \ m, j = 1 \ldots \ n \tag{4.2}$$

where O is the original image and S is the segmentation mask, yielding the matrix R, and m is the number of columns in the image and n is the number of rows in the image. The resulting matrix R is of equal size to O and P and contains the original gray-level of O in all regions designated by S as being of a tissue region and contains a gray-level value of 0

(black) in all regions designated by S as being a non-tissue region. Results for a typical test image are shown in Figure 4.9.

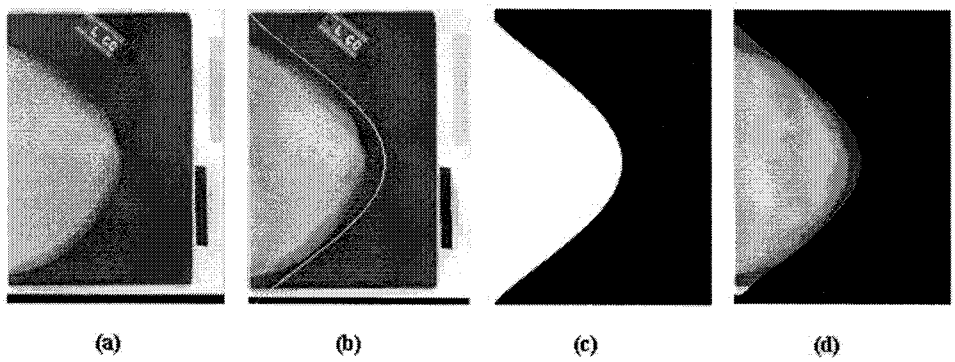

FIGURE 4.9 - Tissue segmentation results for a typical image - (a) original X-ray (b) edge detection (c) mask generation (d) tissue segmented image.

4.5 Threshold Determination

Upon localization of the breast tissue region using the segmentation mask, the subsequent step is to generate a threshold to differentiate between radiodense and radiolucent tissue. Determination of this estimated threshold relies on assumptions made about the images under test. The following assumptions are made in developing the density estimation algorithms:

a) Pixel gray-level is considered as a deciding factor in segmenting radiodense tissue from radiolucent tissue.

b) The shapes of the segmented tissue in the mammograms are ignored.

c) A priori information such as age and other patient history are ignored.

Identification of the radiodense tissue regions in a segmented gray-level image occurs by converting the 256 gray-level image to a binary (black-and-white) format. A value of 1 (white) will be assigned to radiodense tissue and all other pixels will be assigned a value of 0 (black). Generating a threshold to differentiate between radiodense and radiolucent

indications is a non-trivial task. The threshold cannot be a global threshold, but must respond to variations, such as those induced by tissue compression, from image to image and locally within the same image.

Techniques for generating this dynamic threshold for detecting radiodense indications have been developed. A three-step process is employed:

Step 1: Generate mathematical models of the mammogram image by studying the statistics of the gray-level variations.

Step 2: Apply hypotheses testing (detection theory) techniques to determine a single global threshold per image.

Step 3: Modify the threshold dependent upon the physical location of the tissue within the mammogram.

Details of steps 1 and 2 are provided in Chapter 3. Details of step 3 are provided below.

4.6 Parametric Model for Tissue Location using Polar Coordinates

A model has been systematically developed to represent the contour map of the pressure distribution from the tissue compression applied during a mammography procedure. At this stage of the algorithm, there are three major variables known, including the function representing the chest wall, the function representing the edge of the breast, and the CNPA threshold, T_{CNP}. An illustration of the two boundary functions, as extracted from the segmentation mask, is shown in Figure 4.10.

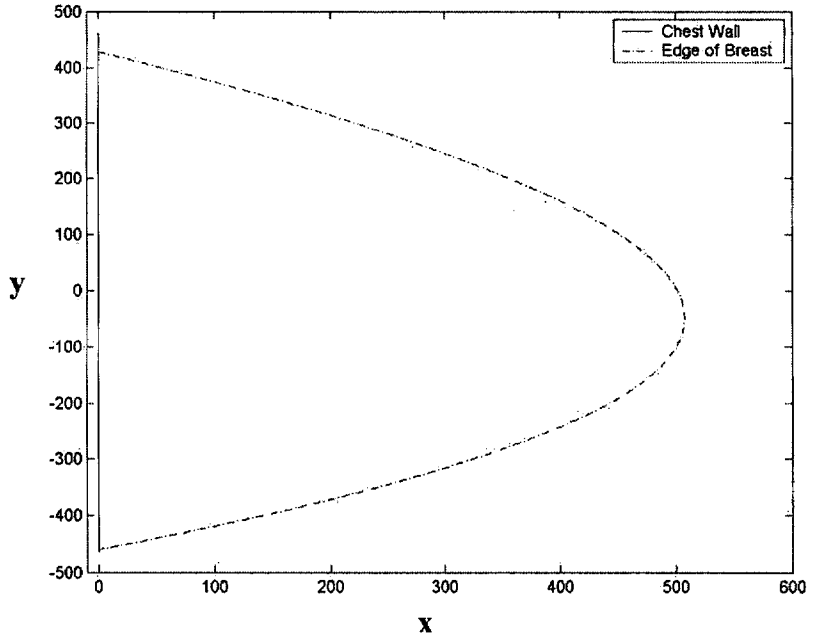

FIGURE 4.10 - Illustrations of the chest wall and the edge of the breast.

In order to represent tissue location within the mammogram, a family of curves is desired between the chest wall and the edge of the breast tissue. Within each of the family of curves, the threshold can be modified dependent upon how close the curve is to the chest wall (or away from the edge of the breast). This modification of the threshold can account for artifacts introduced by tissue compression by increasing the threshold in locations with a greater amount of tissue compression and decreasing the threshold in locations with a lesser amount of tissue compression.

When developing this parametric model for tissue location, the idea is to have the family of curves be indicative of how the pressure is distributed during tissue compression from the chest wall to the edge of the breast tissue. The homotopy continuation algorithm is employed as a tool for interpolating between any two arbitrary functions. Converting the rectangular coordinate information of the two functions into

the polar domain is the first method as a parametric model for tissue location. The following equation are used to convert from rectangular coordinates to polar coordinates

$$r_{chest} = 0 \tag{4.3}$$

$$r_{edge} = \sqrt{x^2 + f_{edge}{}^2} \tag{4.4}$$

$$\theta = \tan^{-1}\left(\frac{f_{edge}}{x}\right) \tag{4.5}$$

where r_{chest} is the polar coordinate equivalent of f_{chest}, r_{edge} is the polar coordinate equivalent of f_{edge} and θ represents the angles associated to r_{chest} and r_{edge}. r_{chest} will always be associated to a vector of zeroes because of the inherent shape when represented in the rectangular coordinates. There is no need to illustrate r_{chest} because it is implicit in nature. However a better understanding of r_{edge} is acquired when interpreting the illustrations as seen in Figure 4.11.

The family of curves is now generated by performing mathematical operations in the polar coordinate system. The homotopy continuation algorithm is proven to be a valid source when interpolating between any two arbitrary functions. In this case, the two arbitrary functions are the chest wall, r_{chest}, and the edge of the breast, r_{edge}. Mathematically, the homotopy continuation algorithm is represented as the following in the polar coordinate system

$$r_t = r_{chest} + \frac{t}{N}(r_{edge} - r_{chest}) \tag{4.6}$$

where r_t represents the family of curves generated in the polar coordinate system, r_{chest} represents the chest wall, r_{edge} represents the edge of the breast tissue, N is the number of curves desired, and t is a scalar that ranges from 0 to N. At $t = 0$, $r_0 = r_{chest} = 0$ and at t = N, $r_N = r_{edge}$. As t increases from 0 to N, r_t is represented as a incremental fraction of

r_{edge}. Application of Equation 4.6 develops a family of curves and an example is shown in Figure 4.12 as represented in the polar coordinate system.

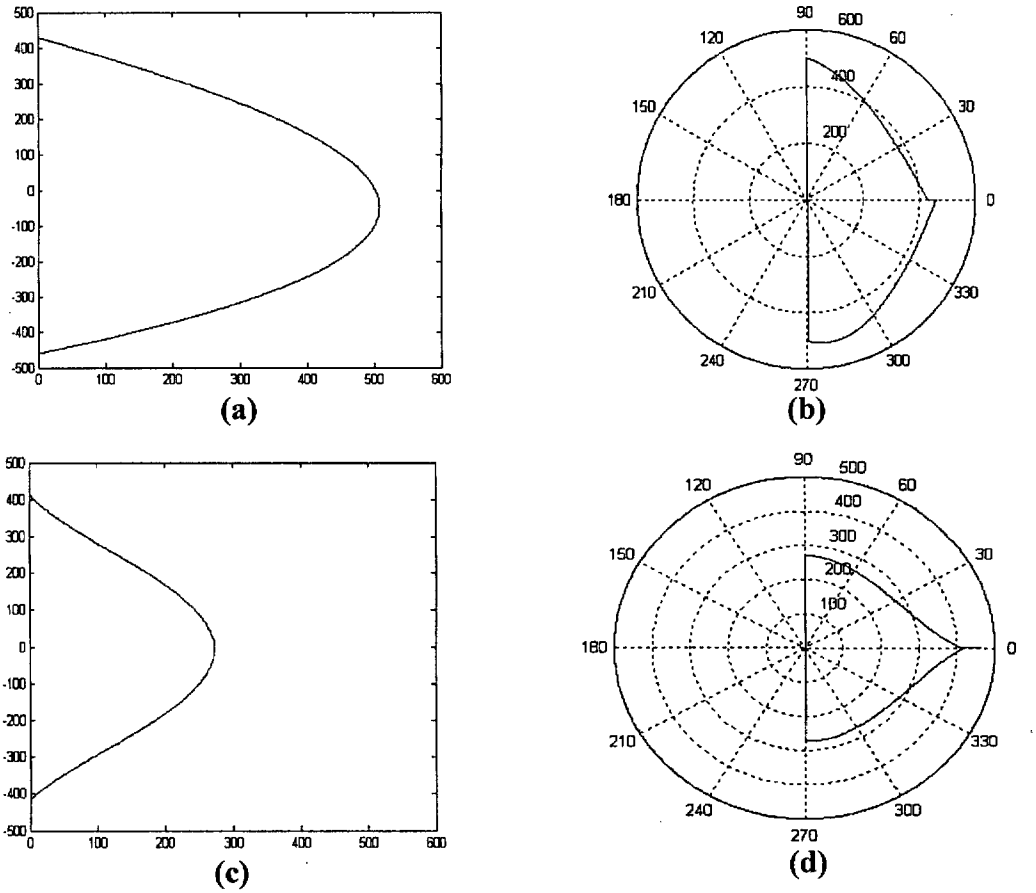

FIGURE 4.11 - (a) f_{edge} of Image 11051702 with (b) r_{edge} of Image 11051702 and (c) f_{edge} of Image 11599502 with (d) r_{edge} of Image 11599502.

After the family of curves is generated, the next step in this process is to convert all information back to into the rectangular coordinate system so the information can be applied on digitized mammograms. The equations to convert back to rectangular coordinates are as follows

$$x = r\cos(\theta) \tag{4.7}$$

$$y = r\sin(\theta) \tag{4.8}$$

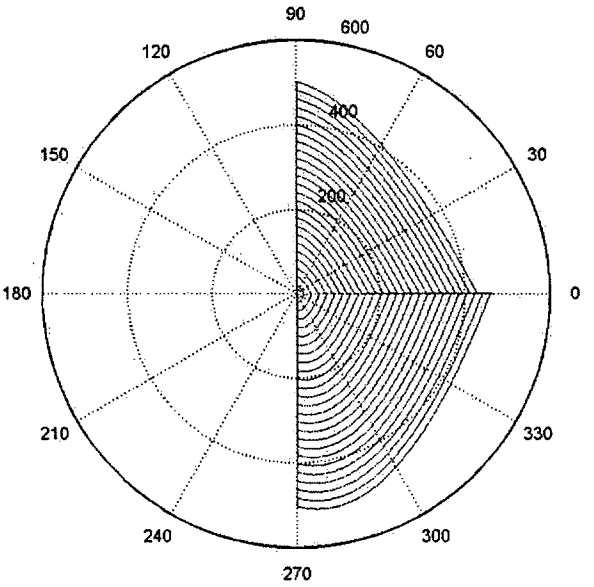

FIGURE 4.12 - Family of curves generated between the chest wall and the edge of the breast tissue as represented in the polar coordinate system.

Applying Equations 4.7 and 4.8 will yield the family of curves generated by the parametric model for tissue location using Polar coordinates and is illustrated in Figure 4.13. This model does not represent the physics of the compression.

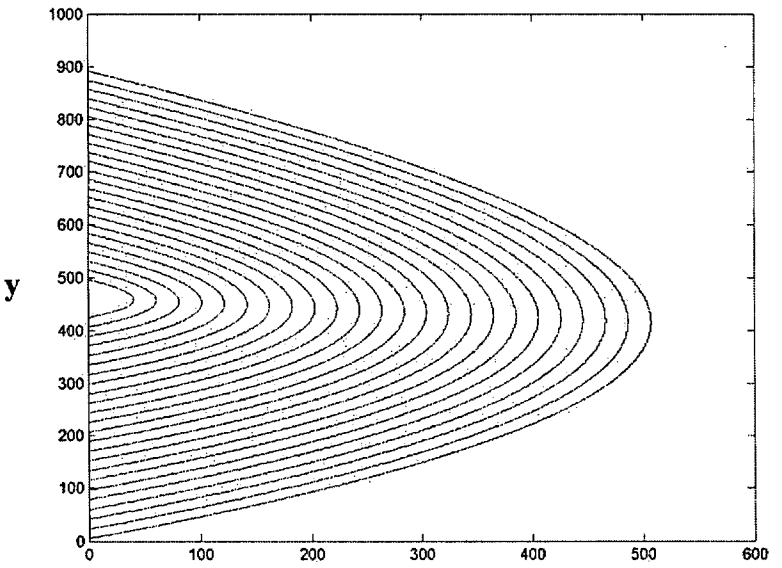

FIGURE 4.13 - Family of curves between chest wall and the edge of the breast.

4.7 Parametric Model for Tissue Location using Rectangular Coordinates

The previous method to develop a parametric model for tissue location using polar coordinates generates the family of curves based on radial differences. An alternate method is developed that will rely on linear differences of the two arbitrary functions when applying the homotopy continuation algorithm. As before, at this stage of the development of an automatically generated threshold, there are three major variables that are known. These variables include the global threshold, T_{CNP}, generated from the constrained Neyman-Pearson algorithm (CNPA), and the functions that model the chest wall boundary and the edge of the breast tissue, generated from the segmentation mask. An illustration of the two boundary functions, as extracted from the segmentation mask, is shown in Figure 4.14.

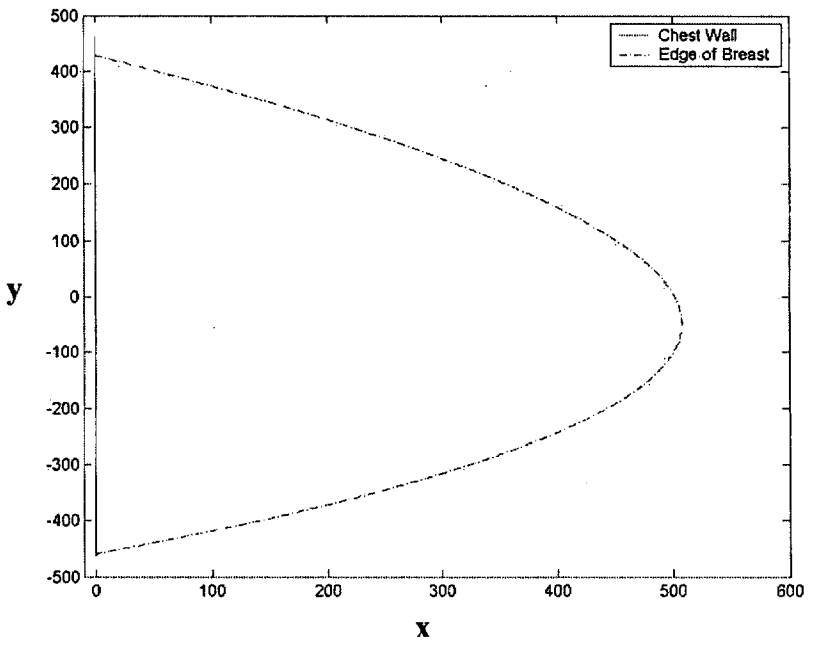

FIGURE 4.14 - Illustrations of the chest wall and the edge of the breast.

The homotopy continuation algorithm is employed as a tool for interpolating between any two arbitrary functions. In this case, the two arbitrary functions are the chest wall, f_{chest}, and the edge of the breast, f_{edge}. Mathematically, the homotopy continuation algorithm can be described as

$$y_t = f_{chest} + \left(\frac{t}{N}\right)\left(f_{edge} - f_{chest}\right) \tag{4.9}$$

where y_t represents the family of curves, f_{chest} represents the chest wall, f_{edge} represents the edge of the breast tissue region, N is the quantity of curves desired between the chest wall and the edge of the breast, and t is an interpolation parameter that ranges from 1 to N. Once applied, the equation produces the family of curves, illustrated in Figure 4.15 with N = 25 and using the f_{chest} and f_{edge} as shown in Figure 4.14. This is assumed as a representation of the equi-pressure contours caused by tissue compression.

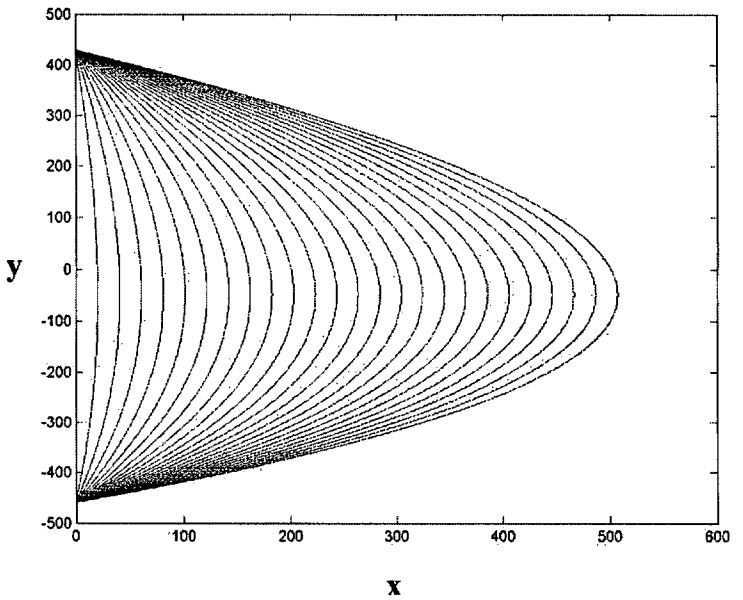

FIGURE 4.15 - Family of curves generated between the chest wall and the edge of the breast.

4.8 Parametric Model for Tissue Compression

The global threshold, T_{CNP}, as determined using the CNPA, is used as the baseline for the threshold to distinguish between radiolucent and radiodense tissue indications. Two methods are described above to account for the physical location of any pixel intensity, $f(x,y)$. The assumption made for the effect of tissue compression is that pixels closer to the chest are affected more by tissue compression because this is the region where tissue compression is the greatest. This is illustrated in Figure 4.16 and Figure 4.17.

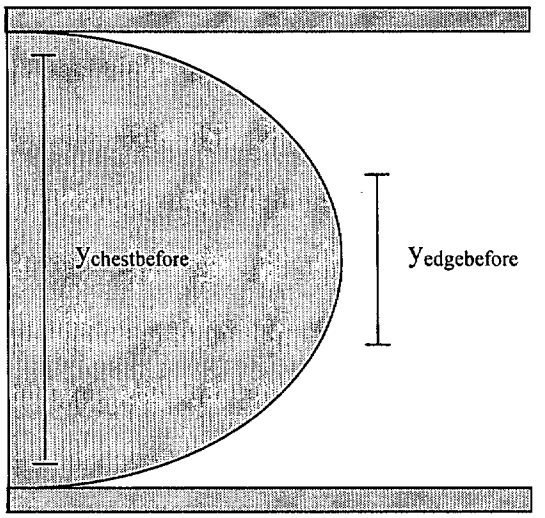

FIGURE 4.16 – Placement of the breast for a CC view in between compression plates before tissue compression is applied.

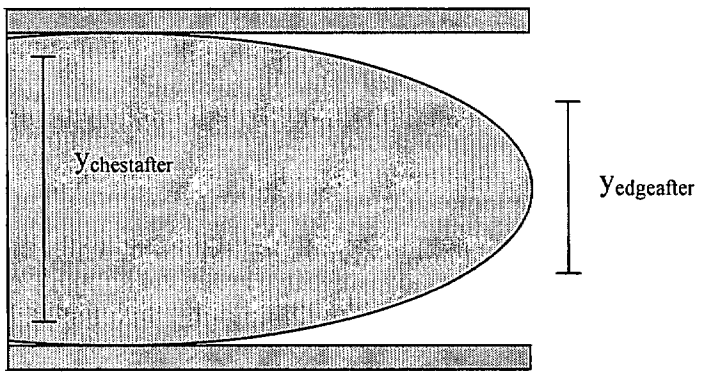

FIGURE 4.17 – Placement of the breast for a CC view in between compression plates after tissue compression is applied.

There is a greater amount of breast tissue at the chest wall and $y_{chestbefore}$ is always greater than $y_{edgebefore}$. Therefore, upon tissue compression, the difference between $y_{chestbefore}$ and $y_{chestafter}$ is always going to be greater than $y_{edgebefore}$ and $y_{edgeafter}$. This implies that the threshold must be relatively higher at the chest wall due to the higher amount of tissue compression.

The global CNPA threshold, T_{CNP}, can be modified dependent on which curve the pixel being analyzed lies on or between. The amount of modification must hold true to the assumption that the threshold will be higher at the chest wall and the threshold will decrease towards the edge of the breast tissue region. A function must be applied through the midpoint of the family of curves to indicate a particular value of how much T_{CNP} should be modified. This function is dependent on the amount of tissue compression that has been enforced in the mammography procedure. The threshold shall be higher towards the chest wall where tissue compression is the highest and lower at the edge of the breast where tissue compression is at a minimum.

Any function can be represented as a sum of Gaussians; therefore, the function incorporated is the Gaussian. This decision is based on the assumption that the pressure distribution will be modeled by a sum of Gaussians. The Gaussian function also follows the assumptions set forth due to the effect of tissue compression in that it starts off at a higher amount and decreases outward. The parametric model for tissue compression that will modify the threshold is represented as the following function,

$$T_v(x) = kT_{CNP}e^{-\frac{x^2}{2\sigma^2}}. \qquad (4.10)$$

where x is the distance from the chest wall to the pixel being analyzed (measured in pixels), T_v is the threshold at position x, k is the scaling factor for the Gaussian, T_{CNP} is

the constrained Neyman-Pearson global threshold, and σ^2 is the variance of the Gaussian. This value decays with dependence on the variance as x approaches the edge of the breast, x_e. At the chest wall, where $x = 0$, the threshold being applied is

$$T_v(0) = A = kT_{CNP}. \tag{4.11}$$

At the edge of the breast tissue, where $x = x_e$, the threshold being applied is

$$T_v(x_e) = B = kT_{CNP}e^{-\frac{x_e^2}{2\sigma^2}}. \tag{4.12}$$

Choice of the two parameters, A and B, will determine the necessary variance for the Gaussian being applied. This is shown below and proves that the selection of the A and B values will allow for an automatic calculation of the trend of the Gaussian function.

$$\sigma^2 = \frac{-x_e^2}{2\log(\frac{B}{A})}. \tag{4.13}$$

An automated method is introduced in the following chapter to automatically generate the A and B values with a dependence on the size of the breast as indicated by x_e. The natural idea is that as the size of the breast increases, more tissue compression is needed during the mammography procedure. Greater amounts of tissue compression will induce more artificial density and therefore the value of A (the threshold generated at the chest wall where tissue compression is greatest) will be higher in larger breasts rather than in smaller breasts, where tissue compression is less.

After the selection of the A and B values and the calculation of the variance, the appropriate Gaussian function is determined. An example of a Gaussian with x_e = 508 (pixels), $T_{CNP} = 0.563$, $A = 1.6$ (T_{CNP}) and $B = 0.9$ (T_{CNP}) is illustrated in Figure 4.17. The

family of curves generated for this particular image was developed with $N = 25$, stating that there will be 25 curves between the chest wall and the edge of the breast tissue. The Gaussian, as seen in Figure 4.18, now acts as a look-up table. There are 25 points captured from the Gaussian. Each point, as denoted in Figure 4.18 with an asterisk, represents the threshold applied to each of the respective 25 curves shown on the x-axis labeled as the curve indices. For example, the first and second curves, those closest to the chest wall, are assigned the highest two gray-level threshold values, being approximately 0.9 and 0.89, respectively, while the last curve (at $N = 25$), is assigned the lowest of the gray-level threshold values, being approximately 0.5. These values of the Gaussian, once applied to the entire family of curves generated using the spatially varying threshold model, appear as in Figure 4.19. Per visualization restraints, only a sub-sample of 5 of the $N = 25$ curves are shown.

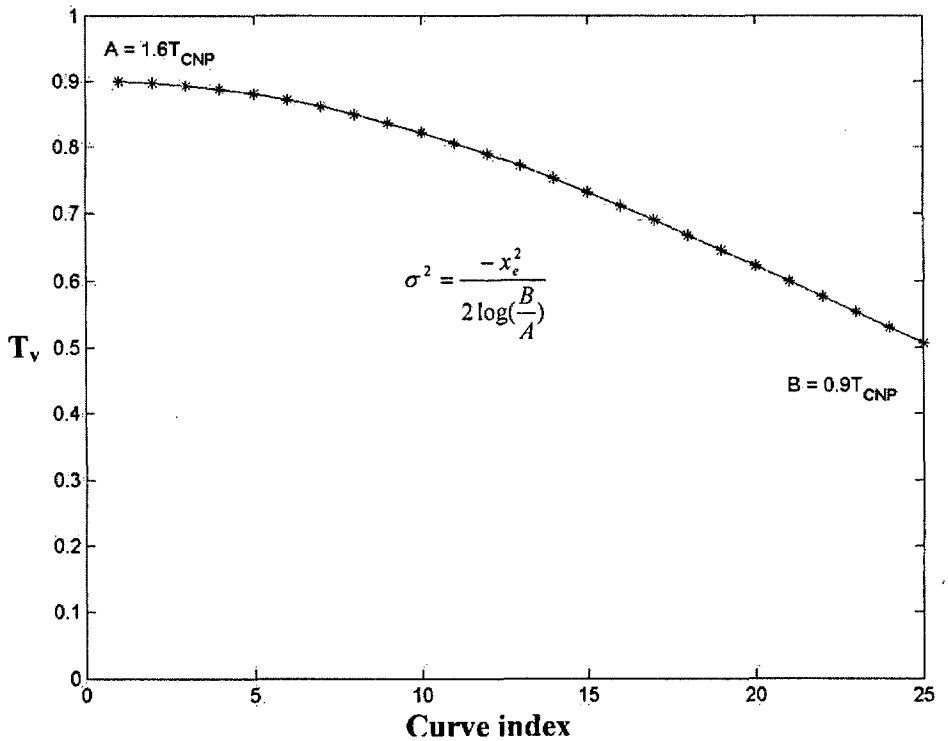

FIGURE 4.18 – Threshold modeled as a Gaussian function.

However, in between the curves, the gray-level threshold is not being assigned and is therefore set to a value of 0. This threshold model must be interpolated in between each of the curves to generate a non-zero gray-level threshold in between the curves. One option would be to allow for an infinite amount of curves to be generated between the chest wall and the edge of the breast tissue, but the computation time would be unacceptable. The fluctuation between curves, from the gray-level threshold value assigned by the Gaussian to the zero value can be seen as high-frequency noise. A common method to reduce high-frequency noise is with local averaging. This is implemented by convolving the signal with the rectangular pulse. This is called a moving-average filter. The gray-level at each pixel is replaced with the average of the gray-levels in a square or rectangular neighborhood. Applying a moving average filter to the image in Figure 4.19 will interpolate between curves and the output is shown in Figure 4.20. Investigation of Figure 4.20 indicates that the pixels locations in between curves have been adequately modified to follow the Gaussian function distribution.

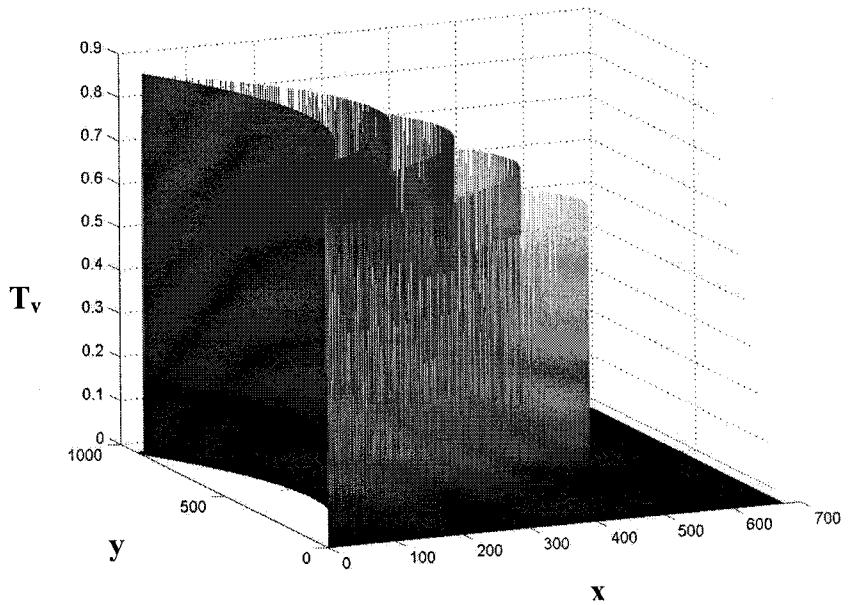

FIGURE 4.19 – Threshold profile after assigning values of the Gaussian function to the parametric model for tissue location using Cartesian coordinates.

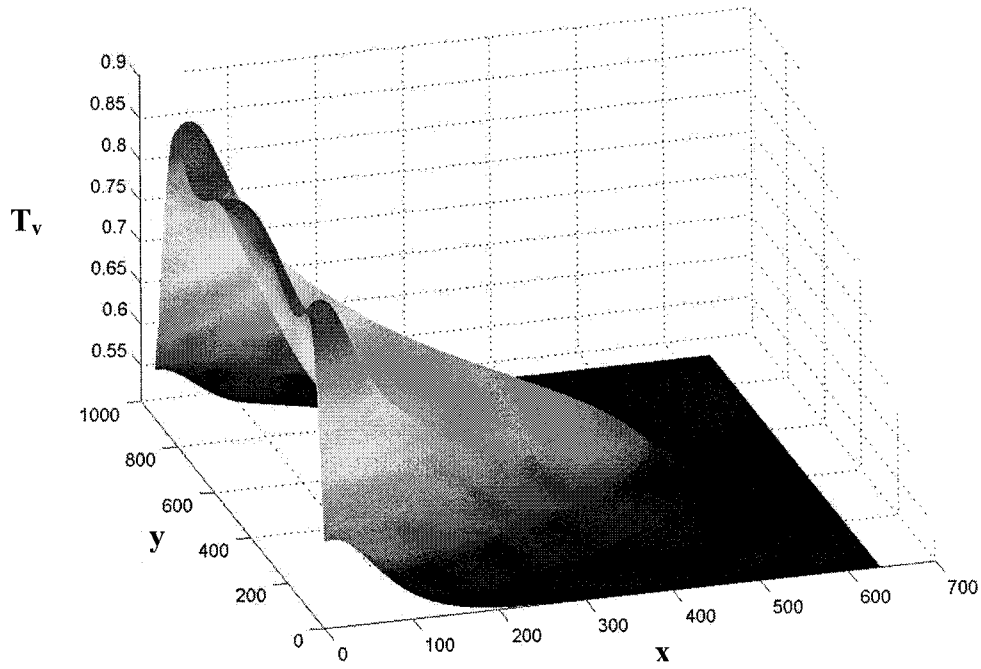

FIGURE 4.20 – An example of a spatially varying threshold model.

4.9 Density Estimation and Image Post-processing

The image shown in Figure 4.19 represents the spatially varying threshold model that will be applied to that particular digitized mammogram. The gray-level value of the pixel at any location (x,y) is compared with the gray-level value in the final spatially varying threshold model at the exact same location, (x,y). If the gray-level value in the digitized mammogram image, $f(x,y)$, is greater in intensity than the gray-level value in the threshold model, $T_v(x,y)$, then that pixel is assigned a value of 1 (white) and is considered to be radiodense tissue. However, if the intensity of the gray-level is less than in the threshold model, that pixel is assigned a value of 0 (black) and is considered to be radiolucent. This essentially creates a binary matrix with pixels at a value of 1 representing radiodense tissue and pixels at a value of 0 representing radiolucent tissue. The percentage of radiodense tissue can be determined using

$$\%RadiodenseTissue = \frac{P_{white}}{P_{total} - P_{film}}(100\%) \tag{4.14}$$

where P_{white} is the total number of white pixels representing radiodense tissue in the matrix, P_{total} is the total number of pixels in the matrix and P_{film} is the total number of pixels in the film-only region, as determined using the segmentation mask.

The methods proposed in this chapter were exercised on two separate data sets from Harvard and Fox Chase that were described earlier. Radiodensity results from the proposed technique were compared to the established "Toronto" method. Chapter 5 presents a collection of the results achieved by applying the algorithms proposed in this thesis on the two sets of images.

CHAPTER 5: RESULTS

5.1 Introduction

Dr. Celia Byrne of the Channing Laboratory, Brigham and Women's Hospital, Harvard School of Medicine provided a set of data consisting of ten images drawn from hospitals across the country. These images are digitized mammogram x-rays and have been used for developing the algorithm proposed in this thesis. It is assumed that the images are uncompressed and have not been enhanced or adjusted in any manner after acquisition from the film scanner. Each of the raw images is of a different patient and contains different image characteristics. These ten mammogram images are shown in Figure 5.1.

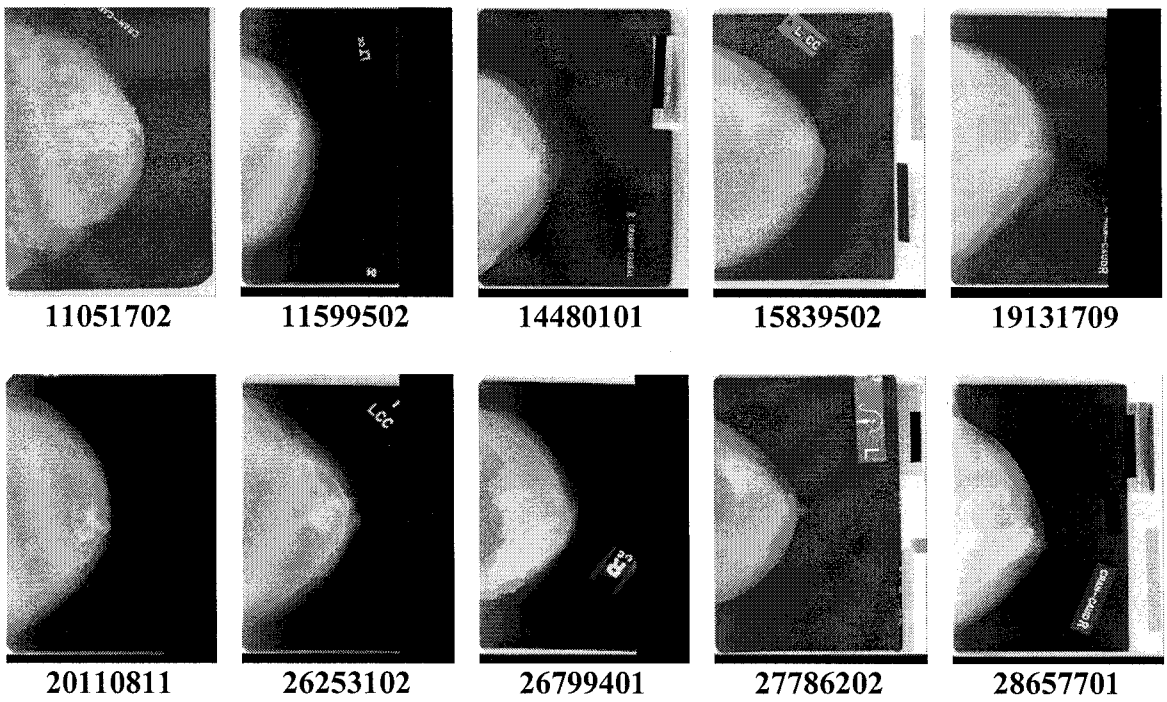

FIGURE 5.1 – Validation set of ten mammogram images provided by the Channing Laboratory, Brigham and Women's Hospital, Harvard School of Medicine with associated identification numbers.

Dr. Byrne analyzed the ten mammograms for radiodensity using the Toronto method. Considerable interaction and expertise is required to perform analysis using this

method. Although the percentage of radiodense tissue for each image was provided, however, no gray-level thresholds or pixel classifications were included. The radiodensity percentages supplied by Dr. Celia Byrne are used as the baseline of comparison for the radiodense tissue segmentation algorithm described in this thesis. Table 5.1 contains the percentages of radiodensity for all ten images as calculated by Dr. Byrne.

TABLE 5.1 – Expert percentages of radiodensity for the Harvard data set of ten mammogram images using the 'Toronto' method for quantify radiodense tissue.

Image Identification Number	Radiodensity Percentage using 'Toronto' Method
11051702	21.4
11599502	12.9
14480101	40.8
15839502	13.3
19131709	1.5
20110811	2.5
26253102	22.5
26799401	55.3
27786202	50.1
28657701	33.6

5.2 Mask Generation and Tissue Segmentation Technique

Typical results for the segmentation between the breast tissue region and the outside film region are shown in Figure 5.2. These results were obtained by implementing the radial basis function neural network tissue segmentation technique described in chapter four.

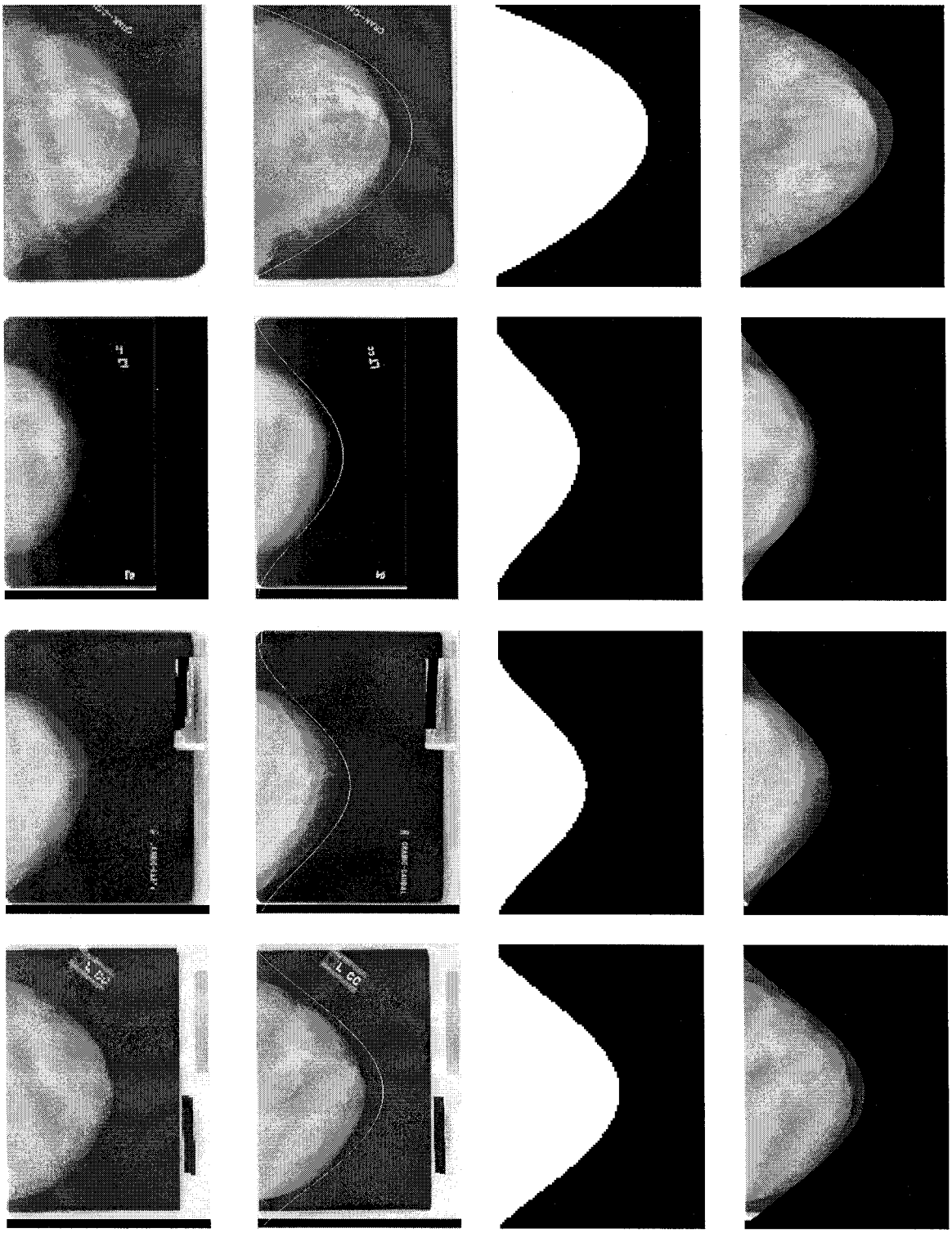

(a) (b) (c) (d)

FIGURE 5.2 – Segmentation mask results from Harvard data set including the (a) original mammogram image, (b) approximation of the edge of the breast tissue region, (c) the binary segmentation mask and (d) the original image after applying the segmentation mask.

These results show that the use of RBF neural networks in the segmentation process provide desirable results in that the final segmentation mask strongly represents the breast tissue region. Segmentation masks using the RBF neural network were generated for the Harvard data set of ten images along with manually generated masks. A comparison of the segmentations masks using the RBF neural network with the manually generated mask allow for a quantitative analysis of the ability to correctly identify the breast tissue region. The percentage differences and mean squared error (MSE) are calculated using

$$\%Diff = \left| \frac{(M_{RBF} - M_{man})}{M_{man}} \right| * 100 \tag{5.1}$$

and

$$MSE = \frac{1}{N} \sum \left| (M_{man} - M_{RBF})^2 \right| \tag{5.2}$$

where M_{RBF} and M_{man} are the amount of pixels with an intensity value of 1 (white) in the RBF neural network based segmentation mask and the manually generated mask, respectively, and N is the amount of pixels in the original image.

Table 5.2 describes the percentage difference along with the mean squared errors for the Harvard data set of ten images. It is assumed that the manually generated segmentation mask is a true representation of the breast tissue region. This will allow the results of the RBF neural network based segmentation masks to be compared with respect to a standard. It must be noted that the true performance of the algorithm is best measured through visual assessment of the resulting image that predicts the breast tissue region. This is because the number of white pixels in the RBF segmentation mask may be equivalent to the number of white pixels in the manually generated segmentation mask, yet are not in the same locations. In this case, the percentage difference will be

zero, but the segmentation mask will not be predicting the correct location of the breast tissue region. Also, the mean squared error value is relative only to the ten images being analyzed. The values generated in Table 5.2 should be interpreted with these characteristics being known.

TABLE 5.2 – Percentage difference and mean squared error between the RBF neural network segmentation masks and the manually generated segmentation masks for the Harvard data set of ten mammogram images.

Patient ID	M_{man}, Manual Mask (pixels)	M_{RBF}, Dynamic Mask (pixels)	% diff	MSE ($x10^2$)
19131709	175518	194535	10.83	5.7773
20110811	207517	205347	1.05	0.0752
11599502	131485	131365	0.09	0.0002
15839502	185481	211931	14.26	11.176
11051702	286757	296618	3.44	1.5534
26253102	205350	202537	1.37	0.1264
28657701	140506	157041	11.78	4.3677
14480101	130239	139395	7.03	1.3392
27786202	111699	124065	11.07	2.4429
26799401	159044	165971	4.36	0.7665

The segmentation mask algorithm was also evaluated on the dataset of the FCCC mammograms to test the efficiency of the algorithm across two different data sets. Figure 5.3 consists of typical results from the segmentation algorithm when testing on four mammogram images from the FCCC data set. Manual segmentation masks were also generated for these four images and served as a baseline when performing the error calculations. It is assumed that the manually generated segmentation mask is a true representation of the breast tissue region. Table 5.3 represents the percentage difference and MSE for the mammograms from the FCCC database using Equations 5.1 and 5.2.

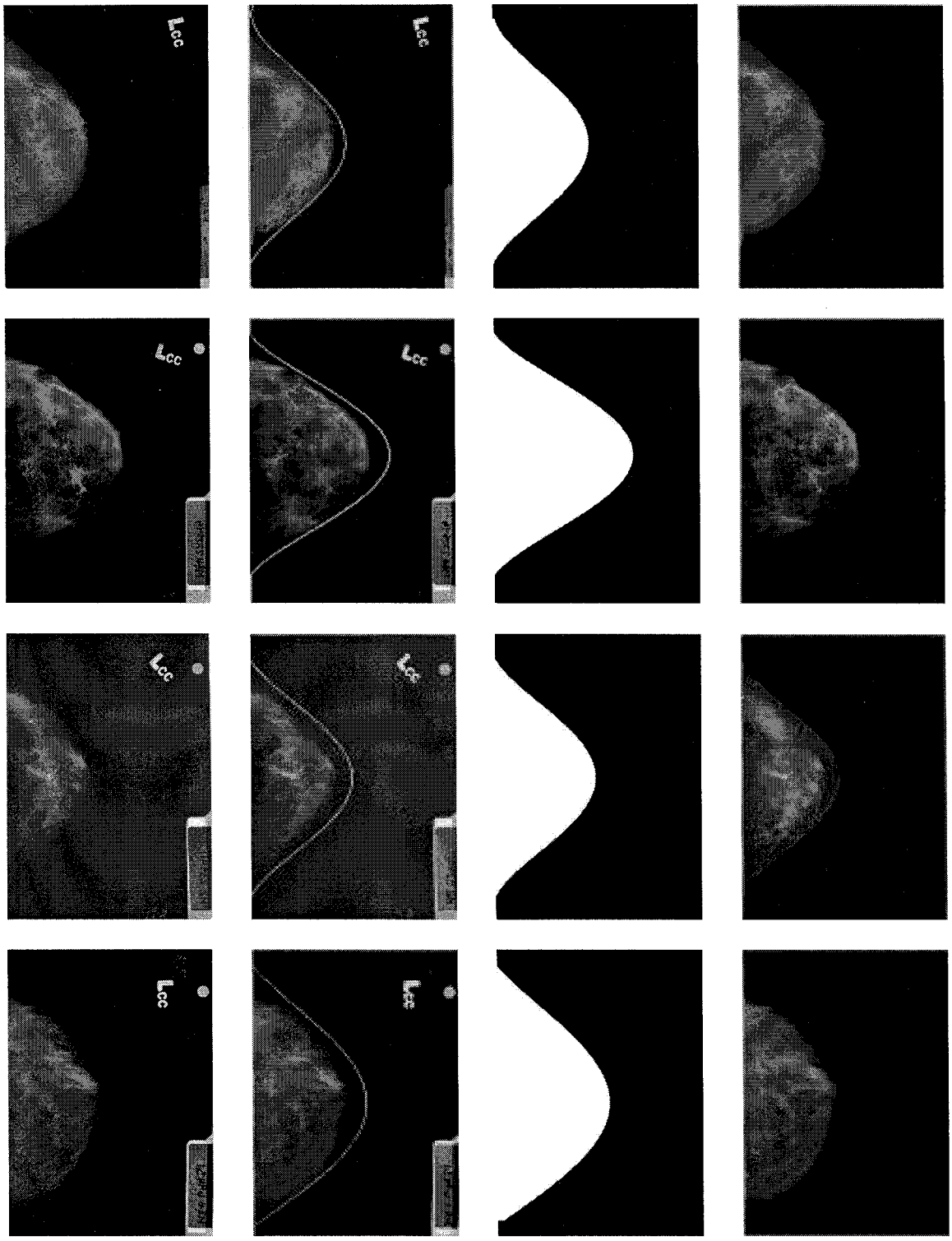

FIGURE 5.3 - Segmentation mask results from FCCC data set including the (a) original mammogram image, (b) approximation of the edge of the breast tissue region, (c) the binary segmentation mask and (d) the original image after applying the segmentation mask.

TABLE 5.3 – Percentage difference and mean squared error between the RBF neural network segmentation masks and the manually generated segmentation masks for the FCCC data set of ten mammogram images.

Patient ID	M_{man}, Manual Mask (pixels)	M_{RBF}, Dynamic Mask (pixels)	% diff	MSE ($x10^2$)
1	221500	183447	17.18	19.06
2	410352	379518	7.51	8.64
3	151740	144163	4.99	0.98
4	208200	190043	8.72	5.60

5.3 Constrained Neyman-Pearson Algorithm

As mentioned in Chapter 3, the constrained Neyman-Pearson algorithm was previously developed at Rowan University as an automated technique to quantify radiodense tissue. Information that was generated from the CNPA is included in Table 5.4. This information consists of the global threshold generated, T_{CNP}. The CNPA allows for the dynamic determination of a threshold value between the pure Bayesian classifier and the mean of the radiodense tissue distribution, given in Equation 3.6 and illustrated in Figure 3.3. The scaling parameter in the equation, α, determines where the global threshold lies between the Bayesian classification and the mean of the radiodense tissue. This value of α is fixed for all images and is set based on image statistics and is determined in [53] as $\alpha = 0.0025$.

TABLE 5.4 – Constrained Neyman-Pearson threshold, T_{CNP}, for the Harvard data set of ten mammogram images.

Image Identification Number	T_{CNP}
11051702	0.563
11599502	0.564
14480101	0.4597
15839502	0.619
19131709	0.6387
20110811	0.565
26253102	0.584
26799401	0.619
27786202	0.572
28657701	0.683

In [53], radiodensity estimates were quantified using only the global threshold, T_{CNP}. The results of these estimates are shown in Figure 5.4. These are the radiodensity estimates of the ten original images shown in Figure 5.1. Pixels with an intensity value of '1' (white) in the breast tissue region represent radiodense tissue and pixels with an intensity value of '0' (black) in the breast tissue region represent radiolucent tissue. Table 5.5 contains the numerical information of the radiodensity estimates along with comparison of the CNPA results with results of the validated 'Toronto' method. Figure 5.5 is a bar graph that compares the results from the CNPA with the validation results from Dr. Celia Byrne analyzing the images with the 'Toronto' method.

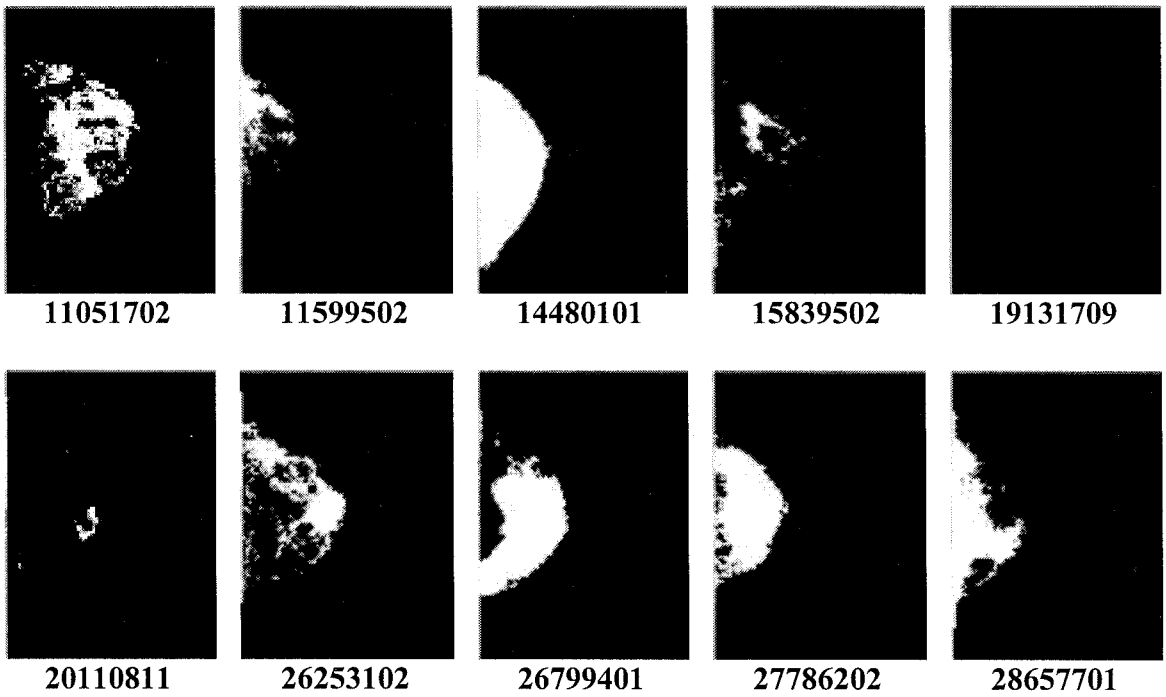

FIGURE 5.4 – Images segmented using the constrained Neyman-Pearson threshold from [53].

TABLE 5.5 - Percentage radiodense of the Harvard data set of ten mammogram images using the constrained Neyman-Pearson algorithm from [53].

Image Number	$T_{CNP(a)}$, threshold from [53]	Percentage radiodense of validation data	Percentage radiodense using CNPA	Squared Error
11051702	0.6481	21.4	21.0694	0.1092
11599502	0.7224	12.9	14.9553	4.2243
14480101	0.4495	40.8	71.0	912.0400
15839502	0.7120	13.3	8.8332	19.9523
19131709	0.8359	1.5	0.3441	1.3361
20110811	0.7404	2.5	1.7608	0.5464
26253102	0.6712	22.5	23.6981	1.4354
26799401	0.5913	55.3	48.4	47.6100
27786202	0.5633	50.1	59.5	88.3600
28657701	0.7856	33.6	39.9421	40.2222

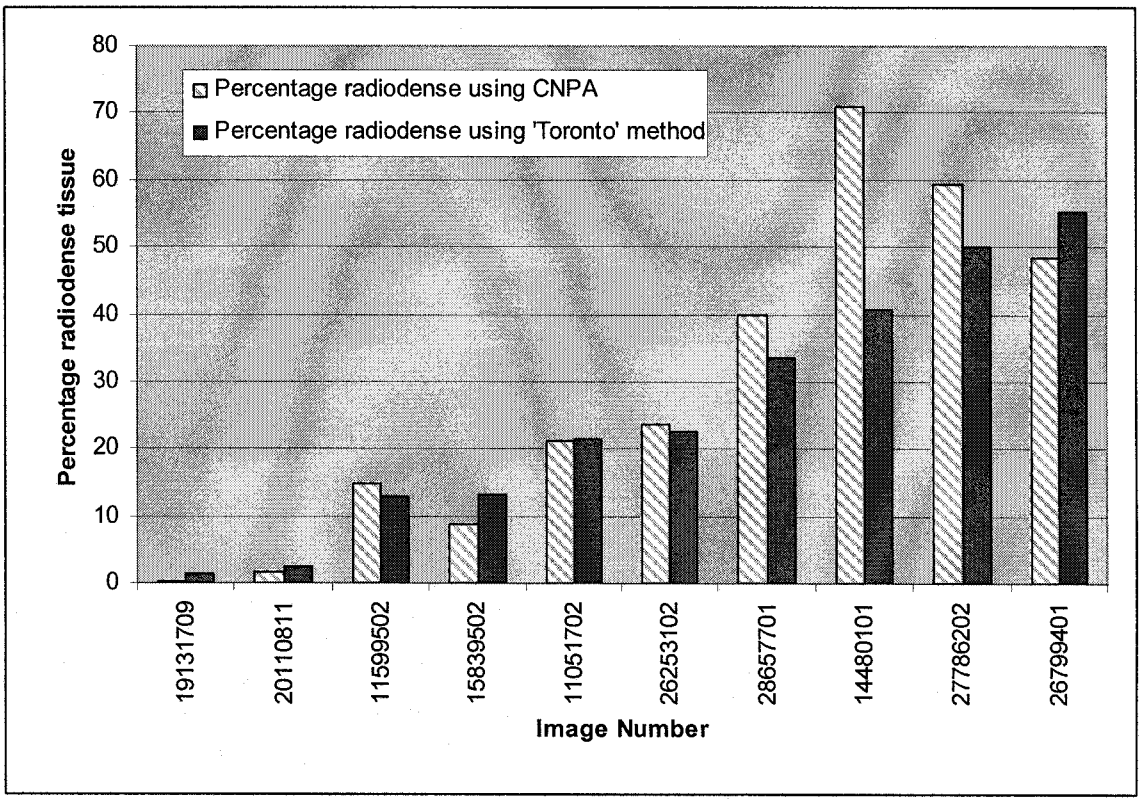

FIGURE 5.5 – Percentage of radiodense tissue for the Harvard data set using both the 'Toronto' method as validation and the constrained Neyman-Pearson algorithm.

The overall mean squared error for percentage radiodense tissue using the CNPA in comparison with the validated results is **111.58**. This was calculated using

$$MSE = \frac{1}{N}\sum\left|\left(RD_{TOR} - RD_{CNPA}\right)^2\right| \tag{5.3}$$

where RD_{TOR} is the percentage radiodense tissue found using the 'Toronto' method for each of the images, RD_{CNPA} is the percentage radiodense tissue found using the CNPA for each of the images, and N is the total number of mammograms being analyzed. Reasons for this error are found in the quantification of radiodense against the chest wall, where the gray level intensity is higher due to compression and not because those regions are radiodense indications; this is not addressed in the CNPA.

5.4 Generating Parametric Models for Tissue Location

The functions that model the chest wall boundary and the edge of the breast tissue have been extracted from the segmentation masks of all ten images of the Harvard data set. The homotopy continuation algorithm has been employed for each of these ten situations to generated a family of $N = 25$ curves. The parametric model for tissue location was determined in the Cartesian coordinate system in concurrence with section 4.5.1. The resulting family of curves between the chest wall boundary and the edge of the breast tissue boundary for each of the ten images is illustrated in Figure 5.6.

It can be noted that these parametric models for tissue location were created for mammogram images of arbitrarily different shapes and sizes. Using only the two known boundaries, the chest wall and the edge of the breast tissue, the homotopy continuation algorithm was able to effectively generate a family of curves for all of the ten images.

5.5 Generating Parametric Models for Tissue Compression

After the parametric model for tissue location has been correctly developed, the parametric model for tissue compression can be incorporated using the Gaussian function given in Equation 4.10. This will represent the modifications needed to modify T_{CNP} to compensate for tissue compression. However, to successfully model the tissue compression, the amount of modification to the global threshold must be given at the chest wall, this amount of modification being denoted as A, and at the edge of the breast tissue region, where this amount of modification is denoted as B.

To successfully determine the A and B values, each image will be tested for a range of the A and B values. A represents the amount that the global threshold, T_{CNP}, will

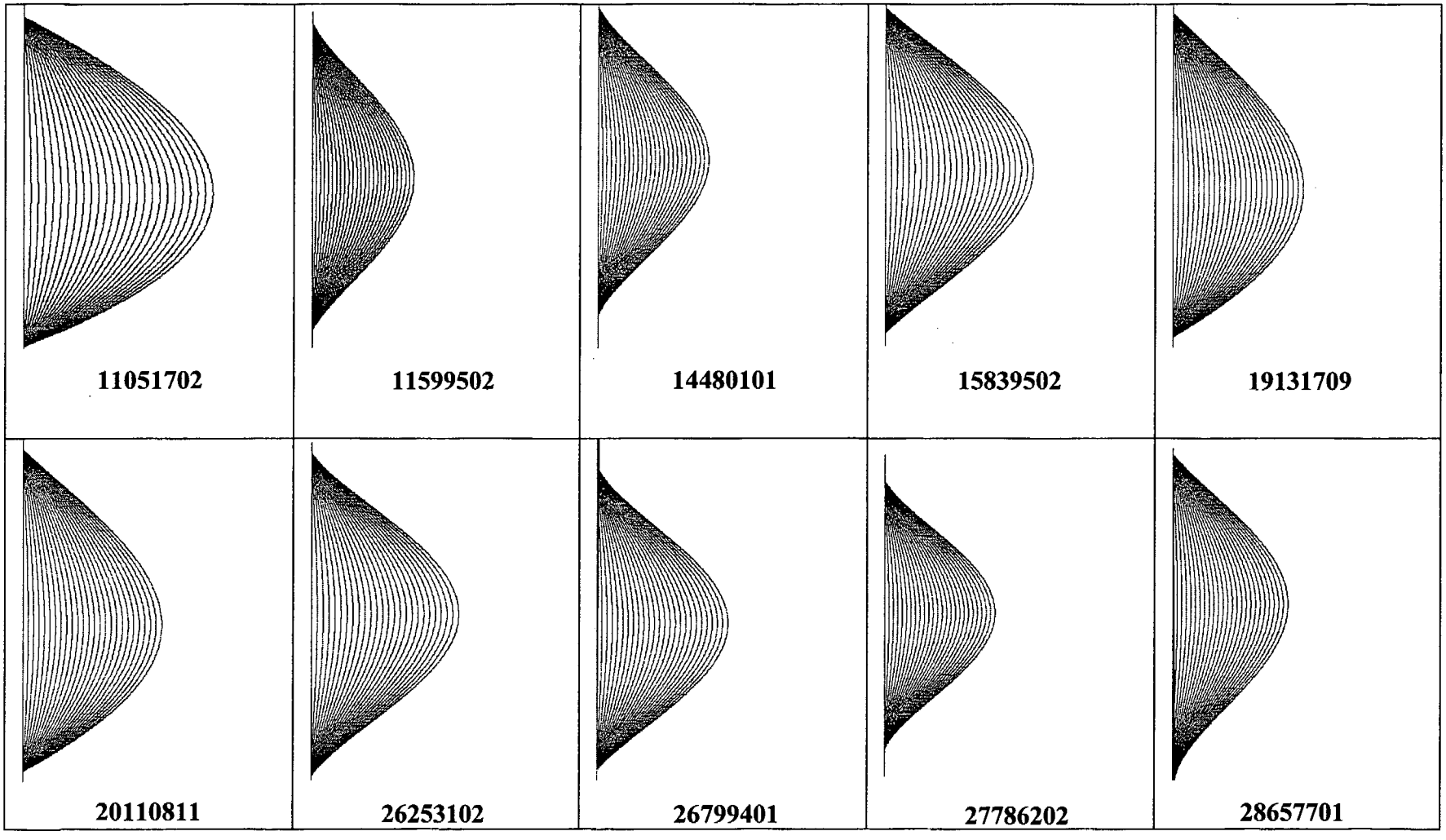

FIGURE 5.6 – Parametric model for tissue location using Cartesian coordinates of each of the ten mammogram images from the Harvard data set.

be adjusted at the chest wall, where the effects of tissue compression are the greatest. B represents the amount that the global threshold, T_{CNP}, will be adjusted at the edge of the breast tissue region, where the effects of tissue compression is at a relative minimum. When the A and B values are selected, the variance of the Gaussian function is determined to define the Gaussian function. After the function is fully defined, the process, as explained in Section 4.6, is followed to generate the spatially varying threshold model for that mammogram image. This process will produce a percentage of radiodense tissue after the acquisition of values for A and B. Testing each image for a range of both A and B while comparing the output percentage radiodensity with those listed in Table 5.1 will produce an error surface plot, allowing for an automated method of determining the most efficient choice for A and B. The range of values for A includes the set of number from 0.9 to 3.1, in increments of 0.01 while the range of value for B include the set of numbers from 0.3 to 0.9, in increments of 0.1. The error surfaces obtained by varying the A and B values for four of the ten mammogram images are given in Figures 5.7 – 5.10.

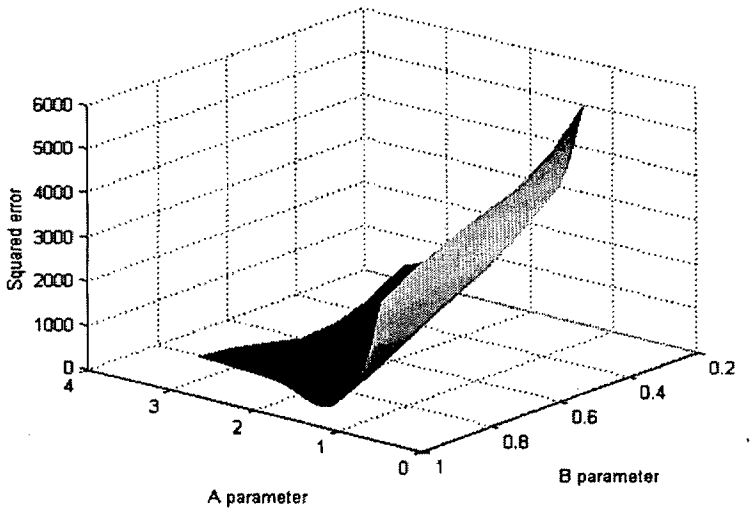

FIGURE 5.7 – Squared error surface plot for Image 11051702.

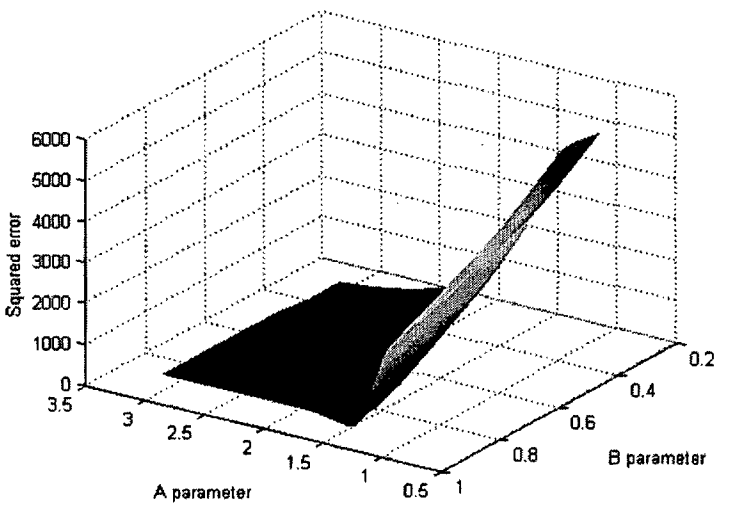

FIGURE 5.8 – Squared error surface plot for Image 11599502.

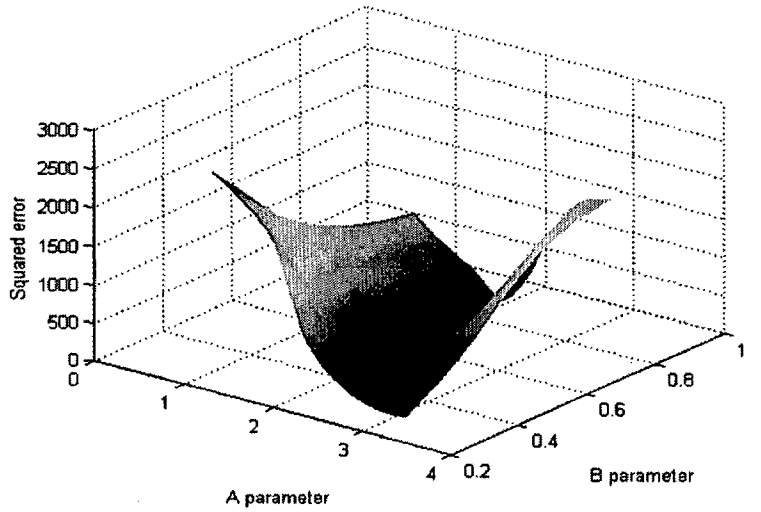

FIGURE 5.9 – Squared error surface plot for Image 14480101.

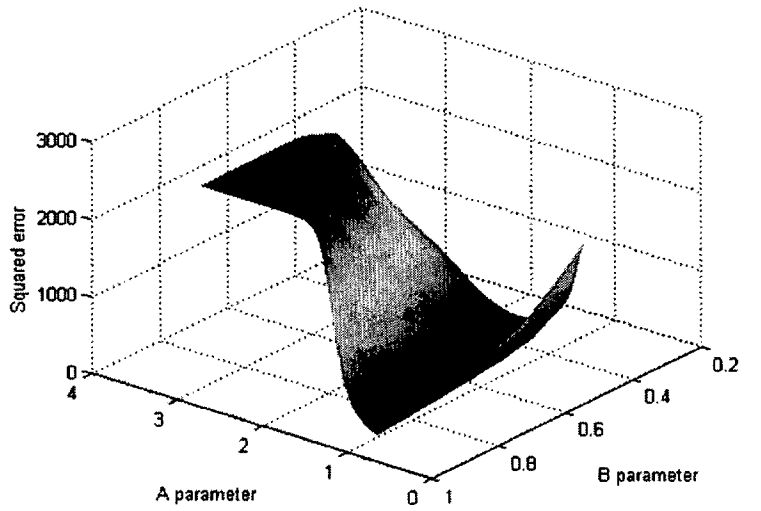

FIGURE 5.10 – Squared error surface plot for Image 15839502.

5.5.1 Determining Characteristics of the Tissue Compression Model

An automated method to determine the appropriate values for A and B from the squared error surface plot is desired. The assumption of tissue compression has been stated and infers that in regions of a greater amount of tissue (i.e. at the chest wall), there will be a higher amount of compression. This can be translated to stating that breasts of a larger size contain more tissue than breasts of a smaller size, and therefore the larger breasts will experience a greater amount of compression at the chest wall than in smaller breasts. With this assumption, both the A and B value are now dependent of the length of the breast. The A values will monotonically increase as the length of the breast increases for the mammogram images being analyzed. However, the compression plates for breasts of a smaller size will be pushed closer together in comparison to breasts of a larger size in the mammography procedure due to the fact that more tissue will create a higher resistance against the compression plates when compressing the breast. It is inferred from this that the B values will be higher in smaller breasts and will monotonically decrease as the breast size is increased and there is less compression at the end of the breast.

A scan is performed on the squared error surface to extrapolate the A and B values where the squared error is at its least. This data is collected for the set of ten mammogram images. A trend will be formed to fit the following assumptions

1) A values will monotonically increase as the length of the breast increases,

2) B values will monotonically decrease as the length of the breast increase, and

3) Both A and B values are calculated as a function of the length of the breast.

The A and B values being extrapolated correspond to the fifty minimum points of error in the squared error surfaces for each of the ten images. A subset of the results for two of the ten images is listed in Table 5.6.

TABLE 5.6 –Ten minimum points of error from the squared error surface and the associated A and B values.

Image number	Length of the breast, x_e (pixels)	A	B	Percentage radiodense tissue	Squared error ($x10^{-3}$)
11051702	508	2.90	0.6	21.3999	0.00000
11051702	508	2.37	0.7	21.3547	2.05209
11051702	508	1.94	0.8	21.4576	3.31776
11051702	508	1.62	0.9	21.5861	27.58921
11051702	508	2.89	0.6	21.5732	29.99824
11051702	508	2.36	0.7	21.6089	43.63921
11051702	508	2.97	0.6	21.1865	45.58225
11051702	508	1.95	0.8	21.1134	82.13956
11051702	508	1.63	0.9	21.0554	118.74916
11051702	508	2.88	0.6	21.7698	136.75204
11599502	272	2.76	0.4	12.9502	2.52004
11599502	272	2.22	0.5	12.8428	3.27184
11599502	272	1.92	0.6	12.9723	5.22729
11599502	272	1.53	0.9	12.7705	16.77025
11599502	272	1.74	0.7	13.0598	25.53604
11599502	272	2.77	0.4	12.7264	30.13696
11599502	272	2.75	0.4	13.1801	78.45601
11599502	272	1.62	0.8	12.6152	81.11104
11599502	272	2.21	0.5	13.2090	95.48100
11599502	272	1.93	0.6	12.5795	102.72025

This extrapolation occurs for all of the ten images and a trend is chosen that coincides with the assumptions outlined above and the values chosen for A and B based on this trend is included in Table 5.7.

TABLE 5.7 – Percentage of radiodense tissue using the optimal A and B values.

Image number	Length of breast, x_e (pixels)	A Optimized	B Optimized	Percentage radiodense tissue	Squared error
11599502	272	1.922	0.7	6.3396	43.0388
14480101	293	2.075	0.7	36.7904	16.0769
27786202	298	1.8	0.6	59.9903	97.8180
28657701	310	1.9	0.5	51.7253	328.5265
26799401	348	1.8	0.6	46.6353	75.0770
19131709	350	2.025	0.6	0.1146	1.9193
20110811	371	2.22	0.5	3.4853	0.9708
15839502	398	2.4	0.45	19.4733	38.1096
26253102	400	3.01	0.35	23.1385	0.4076
11051702	508	2.9	0.45	18.4783	8.5363

The optimal A and B values chosen in Table 5.6 were chosen with respect to a set of minimum squared errors. These values must now be calculated with a dependence on the length of the breast, x_e to allow for an automated process in selecting the A and B values. To do so, the A values and the B values will be calculated as a function of the length of the breast

$$A = f_1(x_e) \tag{5.4}$$
$$B = f_2(x_e). \tag{5.5}$$

5.5.1.1 – Determining the Length of the Breast Tissue Edge

To automate this process of generating efficient A and B values, an important value to obtain about the mammogram image is the length of the breast, x_e. The segmentation masks shown in Figure 5.3 represent the breast tissue region with a minimal amount of error. The length of the breast tissue region can be produced with through an analysis of the segmentation mask. This analysis is simply performed by seeking the outermost column in which the segmentation mask contains a pixel with an intensity value of '1' which represents the breast tissue region. This process appears in Figure 5.11.

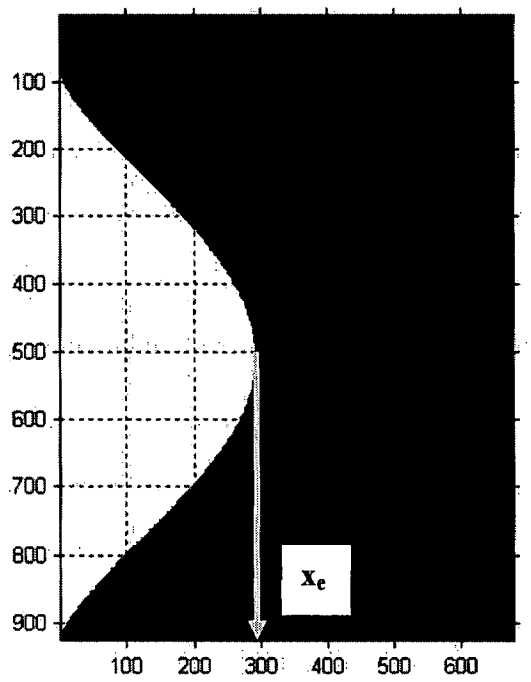

FIGURE 5.11 – Method to determine the length of the breast tissue, x_e, by analyzing the segmentation mask of the original mammogram image.

TABLE 5.8 – x_e for each of the ten mammogram images.

Image Identification Number	x_e
11051702	508
11599502	272
14480101	293
15839502	398
19131709	350
20110811	371
26253102	400
26799401	348
27786202	298
28657701	310

5.5.1.2 - Determining the A values for the Tissue Compression Model

The functions, f_1 and f_2, must abide by the assumption in that f_1 must be monotonically increasing while f_2 is monotonically decreasing. To determine f_1, the optimized A values found in Table 5.7 are plotted against the length of the breasts, x_e, for each of the ten mammogram images and this is shown in Figure 5.12.

The data in Figure 5.12 is fit with a monotonically increasing linear equation and A can now be solved automatically as a function of the length of the breast tissue, x_e. Figure 5.13 shows the data from Figure 5.12 with the monotonically increasing linear equation fitting the data. The linear equation is

$$A = f_1(x_e) = 0.0051x_e + 0.3891. \tag{5.6}$$

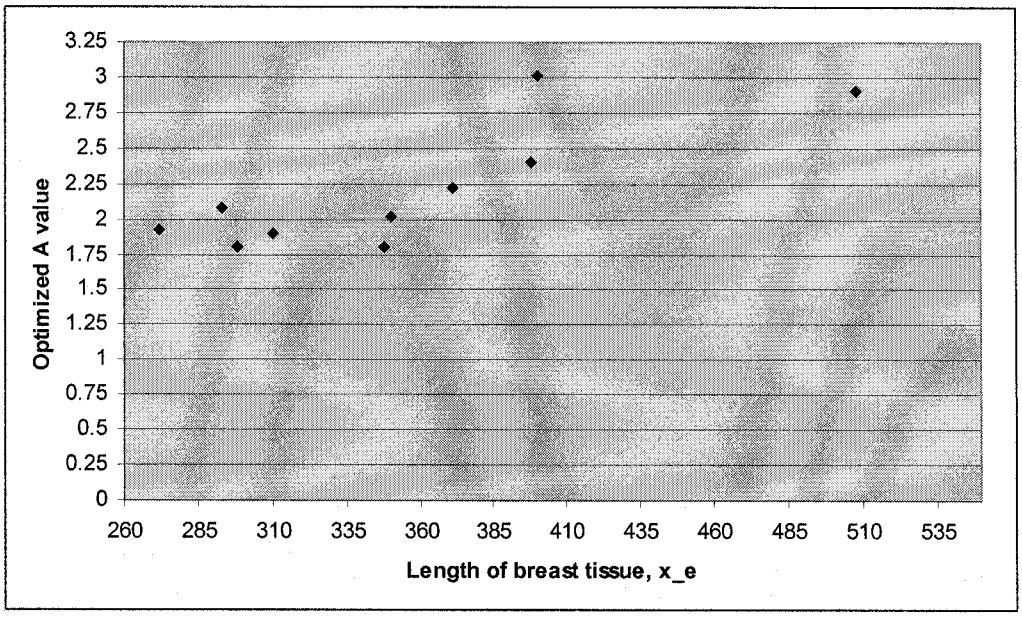

FIGURE 5.12 – Plot of the optimized A values from Table 5.6 versus the length of the breast tissue for each of the ten mammogram images from the Harvard data set.

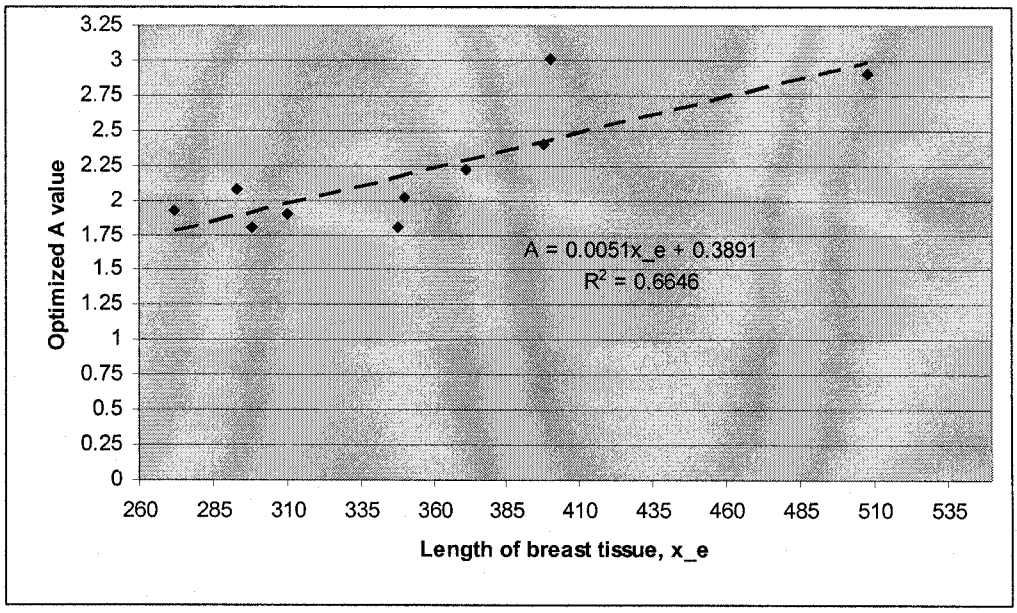

FIGURE 5.13 – Monotonically increasing linear equation in the form of $A = f_1(x_e)$.

5.5.1.3 - Determining the *B* values for the Tissue Compression Model

To determine f_2, the optimized B values found in Table 5.7 are plotted against the length of the breasts, x_e, for each of the ten mammogram images and this is shown in Figure 5.14.

The data in Figure 5.14 is fit with a monotonically decreasing 2nd order polynomial equation and B can now be solved automatically as a function of the length of the breast tissue, x_e. Figure 5.15 shows the data from Figure 5.14 with the monotonically decreasing 2nd order polynomial equation fitting the data. The 2nd order polynomial equation is

$$B = f_2(x_e) = 7.9059e^{-6}x_e^{\,2} - 0.0076x_e + 2.1882\,. \qquad (5.6)$$

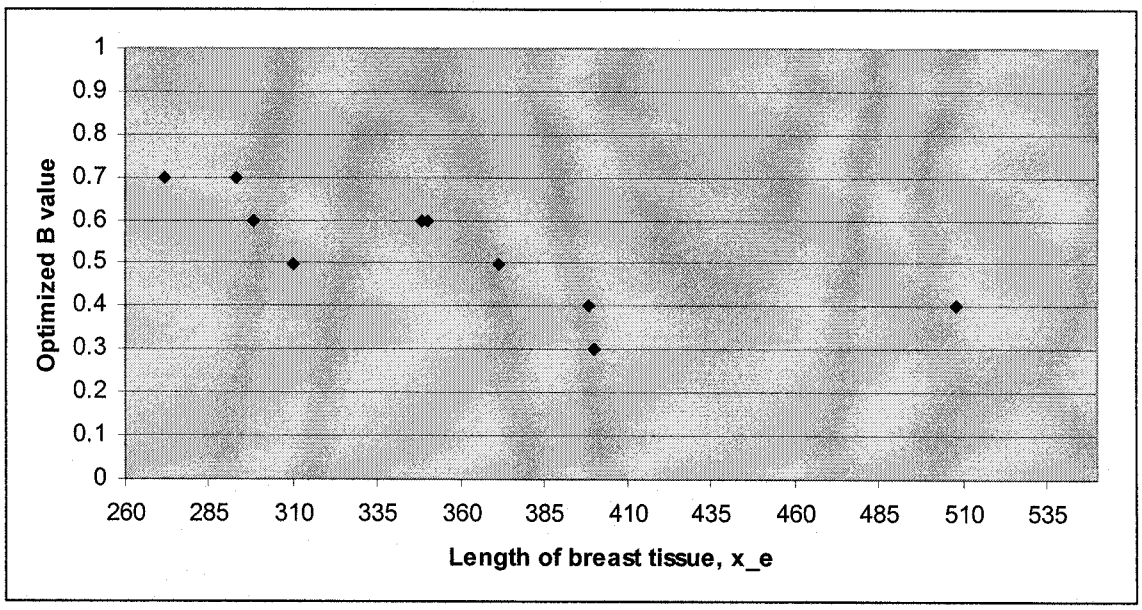

FIGURE 5.14 – Plot of the optimized B values from Table 5.6 versus the length of the breast tissue for each of the ten mammogram images from the Harvard data set.

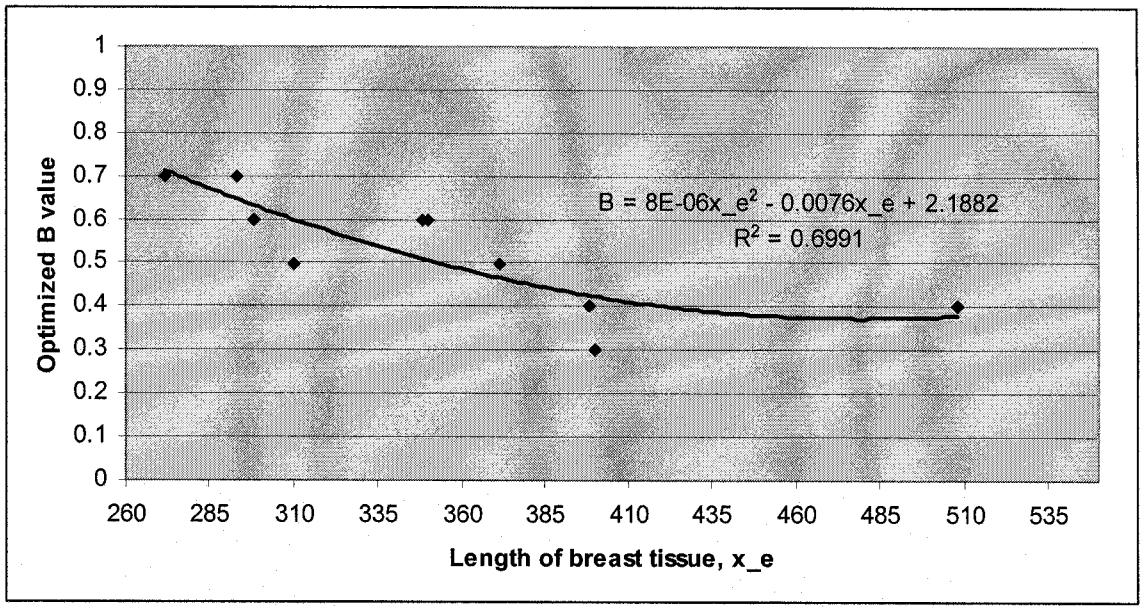

FIGURE 5.15 – Monotonically decreasing 2nd order polynomial equation in the form of $B = f_2(x_e)$.

5.5.1.4 – Results

The assumptions have been made that the $f_1(x_e)$ should be monotonically increasing and $f_2(x_e)$ should be monotonically decreasing, both with dependence on the length of the

breast tissue region. By knowing only the length of the breast tissue, which is found through analysis of the segmentation mask, the parametric model for tissue compression can be generated. The results from by applying $f_1(x_e)$ and $f_2(x_e)$ to determine A and B values are shown in Table 5.9.

TABLE 5.9 – The A and B values obtained by solving for $f_1(x_e)$ and $f_2(x_e)$.

Image Number	x_e, length of breast tissue	A from $f_1(x_e)$	B from $f_2(x_e)$
11599502	272	1.7814	0.7125
14480101	293	1.8889	0.6472
27786202	298	1.9145	0.6327
28657701	310	1.9759	0.5995
26799401	348	2.1704	0.5092
19131709	350	2.1806	0.5051
20110811	371	2.2881	0.4657
15839502	398	2.4263	0.4253
26253102	400	2.4366	0.4228
11051702	508	2.9894	0.3799

The variance, σ^2, is calculated using the A and B values as an input for each of the Gaussian equations that represent the parametric model for tissue compression using equation 4.13. A plot of each of the parametric models for tissue compression for each of the ten images is shown in Figure 5.16.

5.6 – Spatially Varying Threshold Models

The Gaussian functions given in Figure 5.16 must now be transcribed to the corresponding family of curves shown in Figure 5.6 using the process from Section 4.8. The resulting spatially varying threshold model for each of the ten images after the moving average filter is applied is shown in Figure 5.17-5.26.

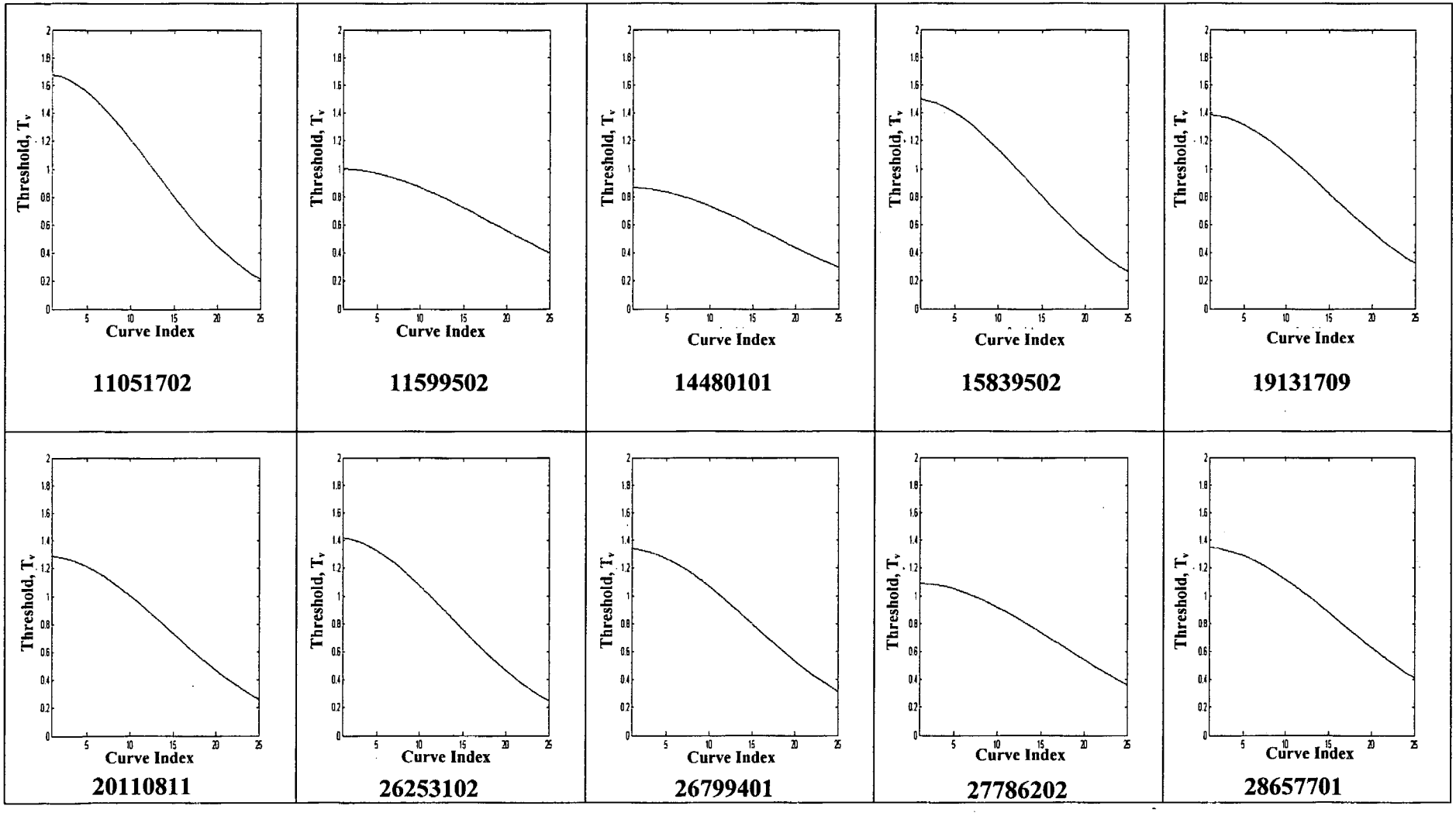

FIGURE 5.16 – Parametric model for tissue compression of each of the ten mammogram images from the Harvard data set.

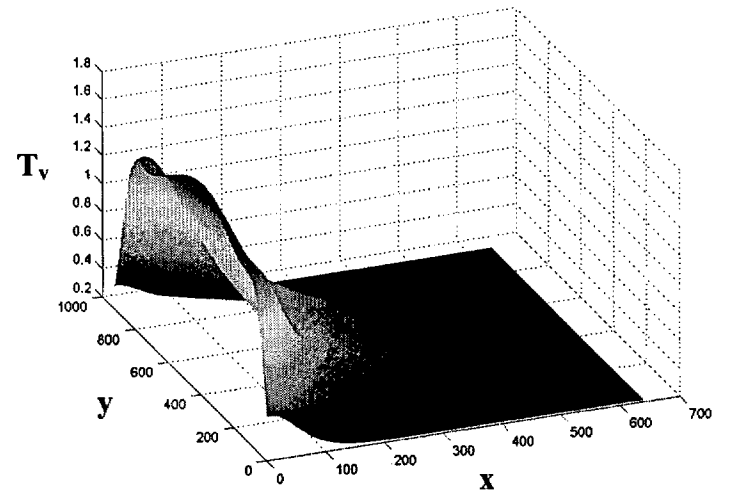

FIGURE 5.17 – Spatially varying threshold model for Image 11051702.

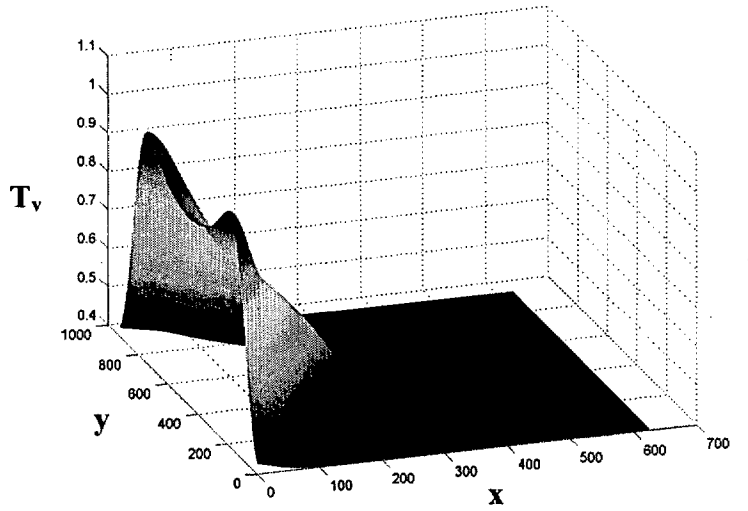

FIGURE 5.18 – Spatially varying threshold model for Image 11599502.

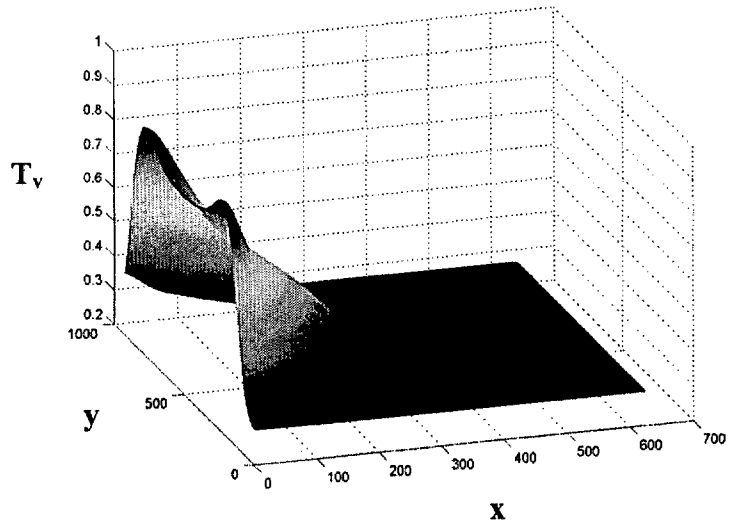

FIGURE 5.19 – Spatially varying threshold model for Image 14480101.

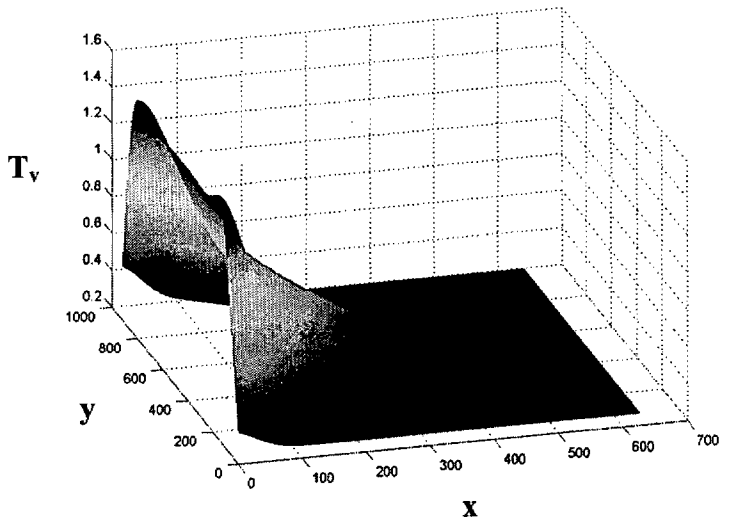

FIGURE 5.20 – Spatially varying threshold model for Image 15839502.

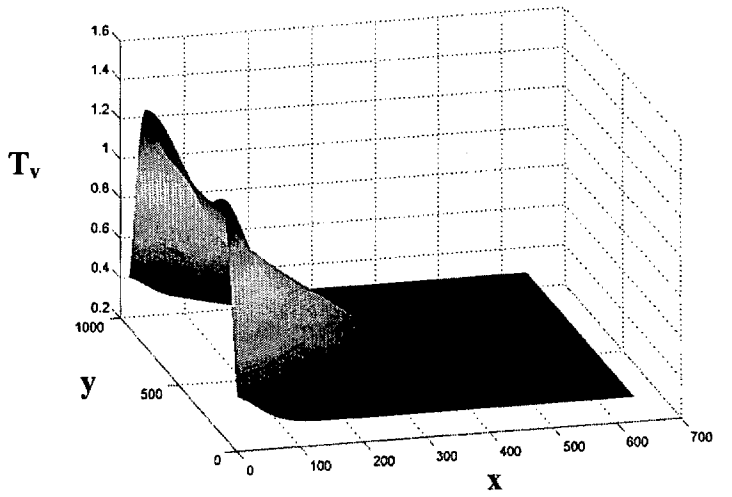

FIGURE 5.21 – Spatially varying threshold model for Image 19131709.

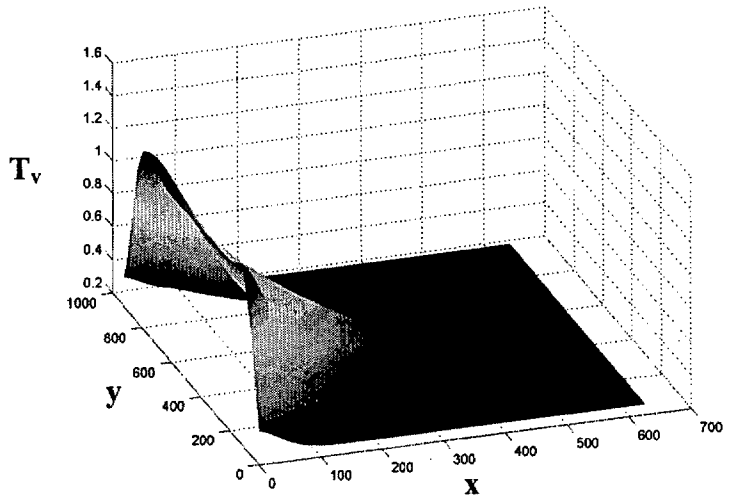

FIGURE 5.22 – Spatially varying threshold model for Image 20110811.

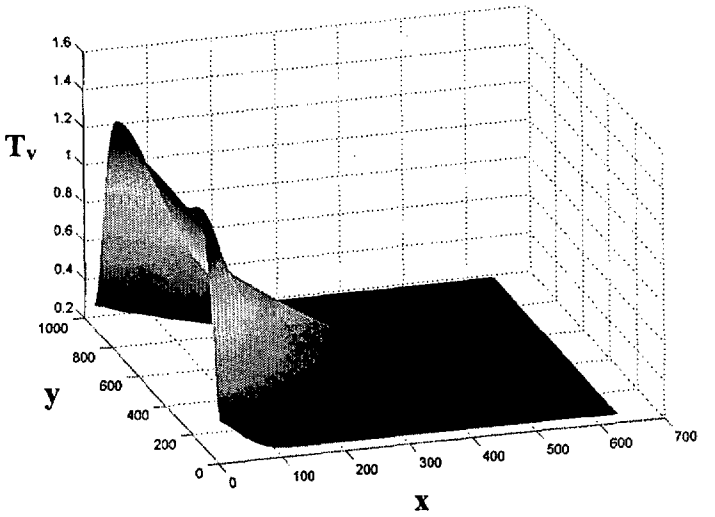

FIGURE 5.23 – Spatially varying threshold model for Image 26253102.

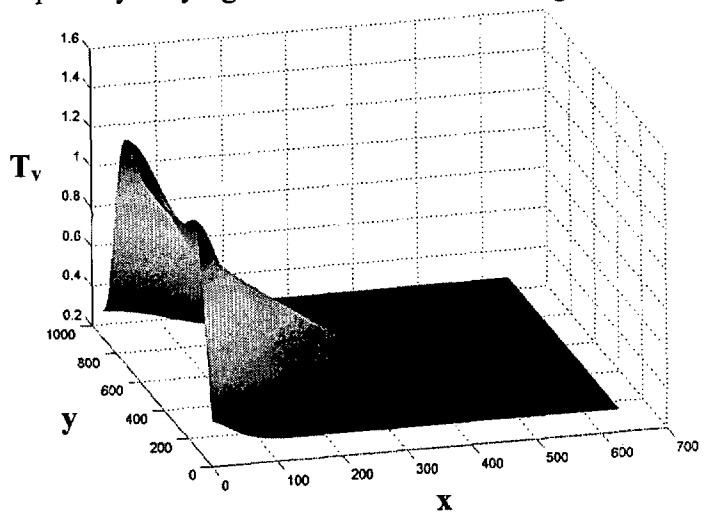

FIGURE 5.24 – Spatially varying threshold model for Image 26799401.

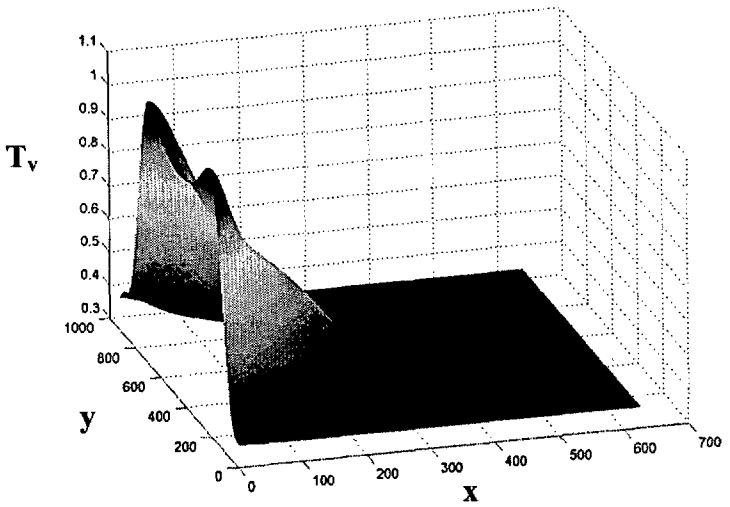

FIGURE 5.25– Spatially varying threshold model for Image 27786202.

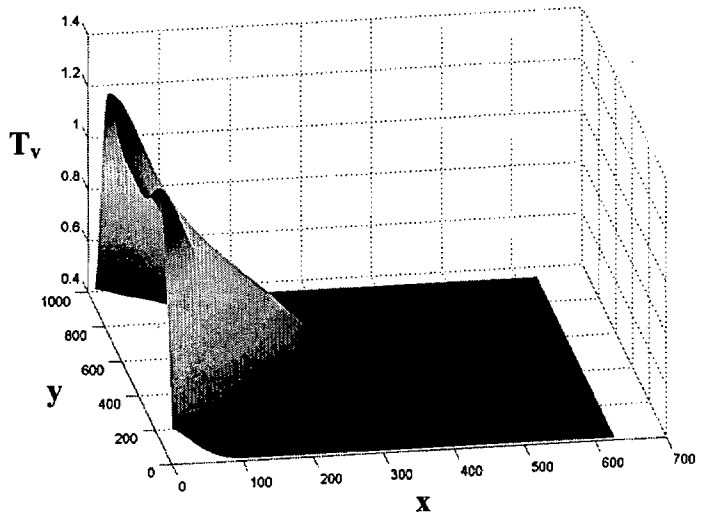

FIGURE 5.26 – Spatially varying threshold model for Image 28657701.

5.7 Density Estimation Results

A piecewise comparison is generated between the original image applied with the segmentation mask and the spatially varying threshold model for that particular image. If the intensity of the pixel at (x,y) in the masked original image is greater than the intensity value of the pixel at the same location in the spatially varying threshold model, then that pixel is classified as being radiodense tissue and will appear as white ('1'). Otherwise, the pixel is classified as radiolucent tissue and will appear as black ('0'). These images that are segmented between radiodense and radiolucent tissue are shown in Figure 5.27. Table 5.10 shows the calculated percentages of radiodense tissue of all images for each of the spatially varying thresholds used along with a squared error between these results and the validated percentages of radiodense tissue from the Toronto method and Figure 5.28 illustrates this comparison. A comparison of this automated method and the CNPA algorithm is shown along with the validated results in Table 5.11 and is illustrated in Figure 5.29.

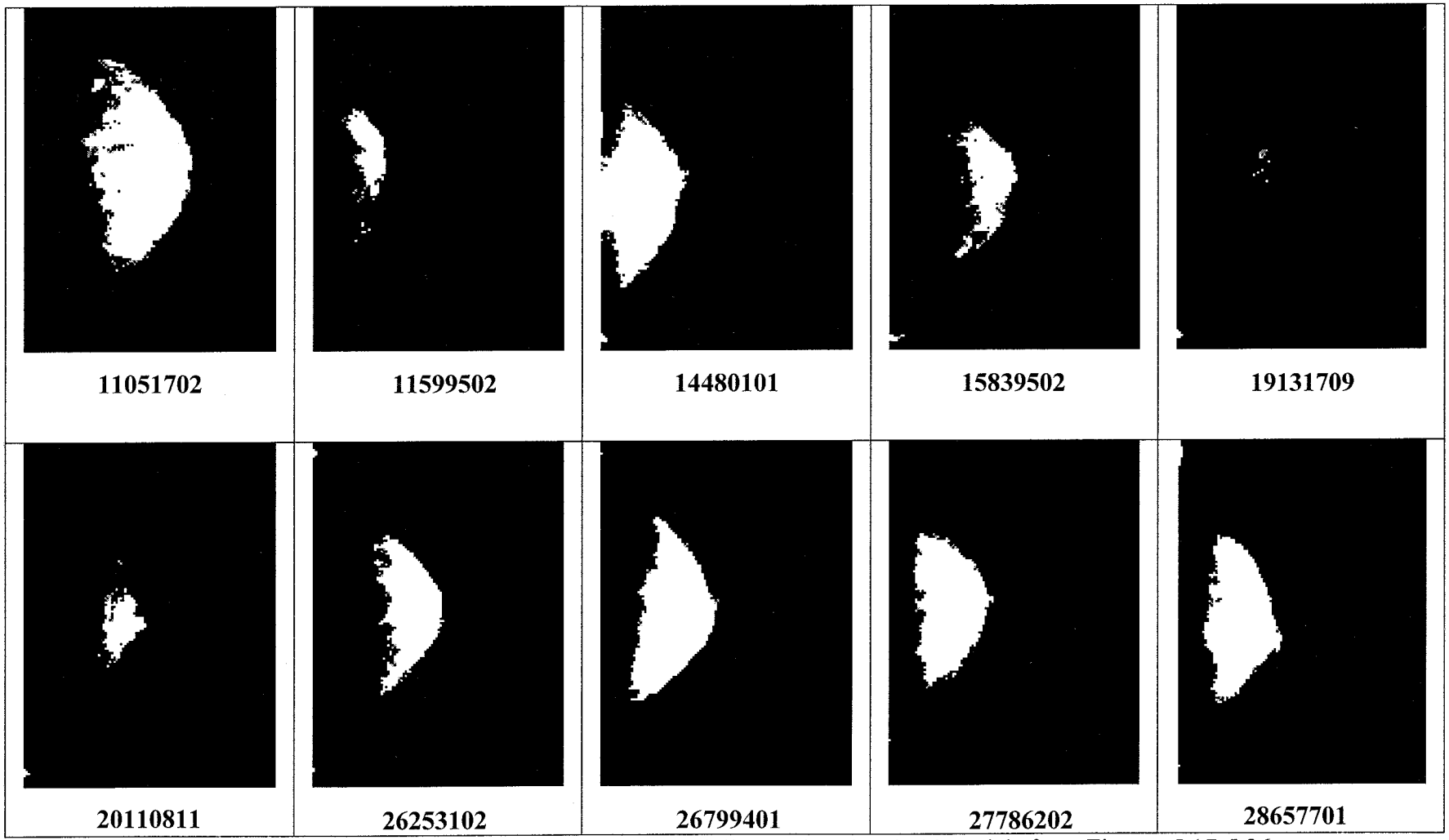

FIGURE 5.27 – Segmented images using the corresponding spatially varying threshold models from Figures 5.17-5.26.

TABLE 5.10 – Percentage of radiodense tissue calculated from using the spatially varying threshold models for each image. The squared error is provided to show the accuracy with respect to the validated percentages of radiodense tissue.

Image Number	x_e, length of breast tissue	A from $f_1(x_e)$	B from $f_2(x_e)$	Percentage radiodense tissue	Squared error
11599502	272	1.7814	0.7125	10.9755	3.7037
14480101	293	1.8889	0.6472	47.7815	48.7413
27786202	298	1.9145	0.6327	45.1030	24.9700
28657701	310	1.9759	0.5995	36.9872	11.4731
26799401	348	2.1704	0.5092	38.4296	284.6104
19131709	350	2.1806	0.5051	0.4004	1.2091
20110811	371	2.2881	0.4657	5.9543	11.9321
15839502	398	2.4263	0.4253	12.7074	0.3511
26253102	400	2.4366	0.4228	20.5918	3.6412
11051702	508	2.9894	0.3799	31.6093	104.2298

The overall mean squared error for percentage radiodense tissue using the spatially varying threshold models in comparison with the validated results is **49.49**. This was calculated using

$$MSE = \frac{1}{N}\sum\left|\left(RD_{TOR} - RD_{SVTM}\right)^2\right| \tag{5.3}$$

where RD_{TOR} is the percentage radiodense tissue found using the 'Toronto' method, RD_{SVTM} is the percentage radiodense tissue found using the spatially varying threshold models, and N is the total number of mammograms being analyzed. This mean squared error is approximately twice as better than the mean squared error found when using the CNPA, which is **111.58**.

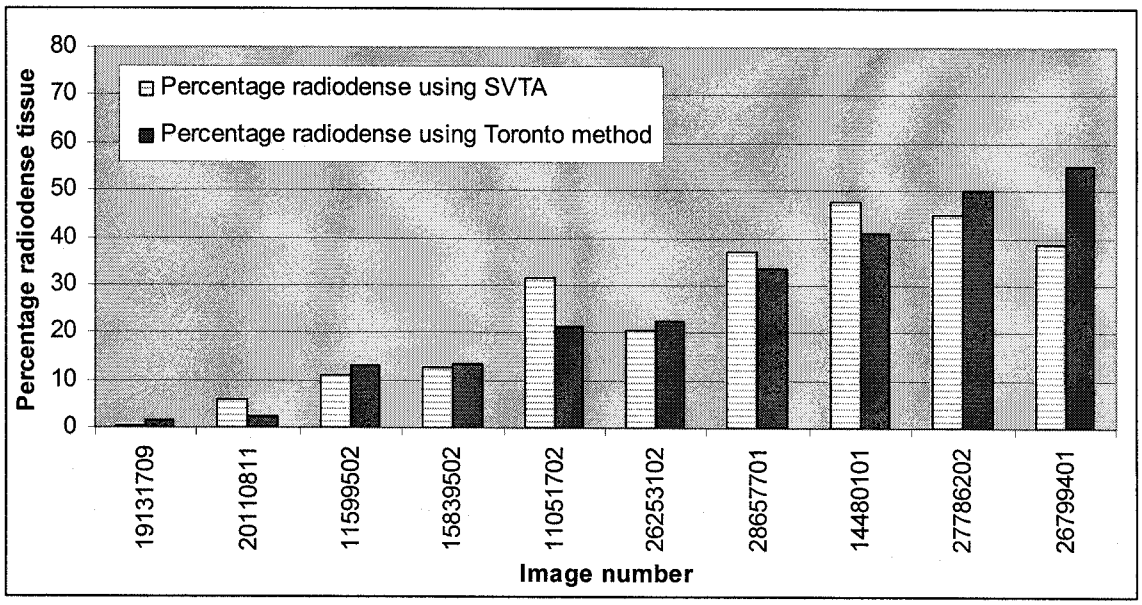

FIGURE 5.28 – Percentage of radiodense tissue for the Harvard data set using both the 'Toronto' method as validation and the spatially varying threshold algorithm (SVTA).

TABLE 5.11 – Comparison of CNPA and SVTA, with SE_{CNP} being the squared error between percentage radiodense tissue using CNPA and the Toronto method, and SE_{SVTA} being the squared error between percentage radiodense tissue using SVTA and the Toronto method.

Image Number	Percentage radiodense using Toronto method	Percentage radiodense using CNPA	Percentage radiodense using SVTA	SE_{CNPA}	SE_{SVTA}
19131709	1.5	0.34412	0.4004	1.3360	1.2091
20110811	2.5	1.6514	5.9543	0.7201	11.9322
11599502	12.9	14.9553	10.9755	4.2242	3.7037
15839502	13.3	7.5043	12.7074	33.5901	0.3512
11051702	21.4	21.0694	31.6093	0.1093	104.2298
26253102	22.5	23.6981	20.5918	1.4354	3.6412
28657701	33.6	38.8218	36.9872	27.2672	11.4731
14480101	40.8	71	47.7815	912.04	48.7413
27786202	50.1	58.0623	45.103	63.3982	24.9700
26799401	55.3	47.8176	38.4296	55.9863	284.6104

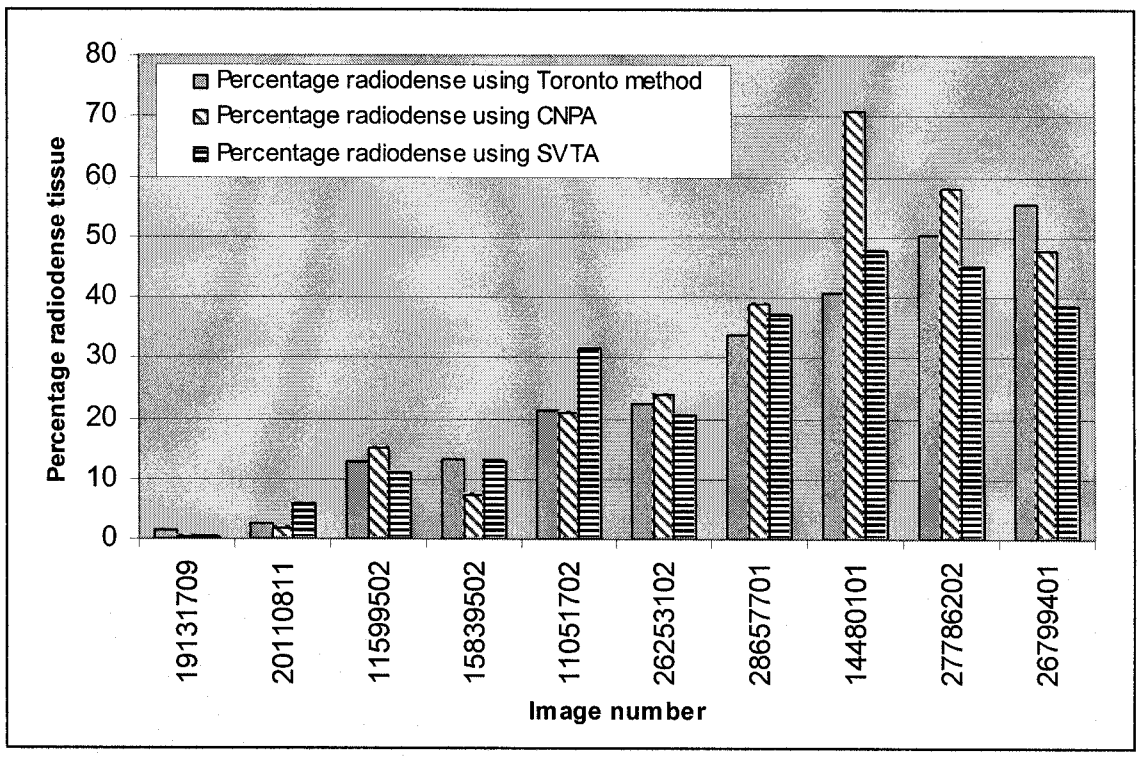

FIGURE 5.29 – Percentage of radiodense tissue for the Harvard data set using the 'Toronto' method as validation, the constrained Neyman-Pearson algorithm (CNPA) and the spatially varying threshold algorithm (SVTA).

5.8 Validation of the Proposed Technique using FCCC Data

The SVTA radiodensity estimation technique that was developed using the set of 10 mammogram images from Harvard was next exercised on a separate database drawn from Fox Chase Cancer Center. This data set consisted of 40 mammograms (including 6 repeats). A subset of the 34 distinct images, 16 (47%) was used as training data to generate the parameters for the SVTA; and the remaining 18 (53%) was used for testing the algorithm. Particular images were flagged due to the fact that Dr. Celia Byrne was not confident in her own decision making in quantifying radiodense tissue. Figures 5.30 and 5.31 show the calculation of the A and B parameters for the model. Table 5.12 shows a comparison of radiodensity estimates that were assessed using three methods – (a) the "Toronto" method by Dr. Celia Byrne, (b) the Constrained Neyman-Pearson algorithm

(CNPA) [53] (c) the SVTA segmentation threshold, described in this thesis. The results are also graphically shown in Figure 5.32. Performance measures of the CNPA and SVTA algorithm in comparison with the Toronto method are shown in Table 5.13. It can be seen that the SVTA segmentation technique is correlated positively with Dr. Byrne's assessment using the Toronto method.

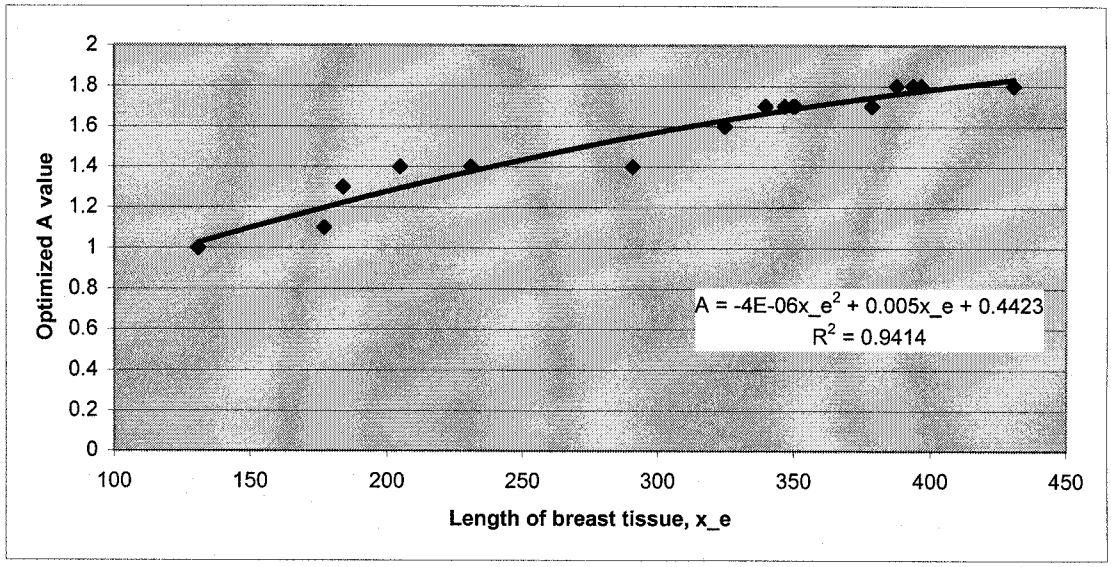

FIGURE 5.30 – Calculation of the *A* parameter for the FCCC images analyzed using the SVTA segmentation technique.

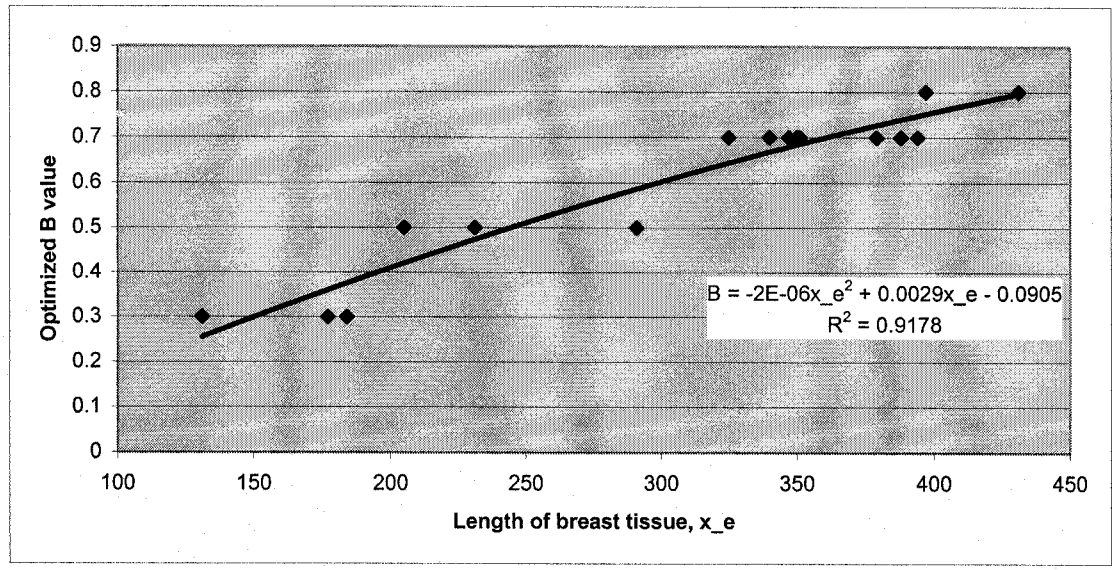

FIGURE 5.31 – Calculation of the *B* parameter for the FCCC images analyzed using the SVTA segmentation technique.

TABLE 5.12 –Segmentation results using various techniques.

Image #	SVTA	CNPA	Toronto
4706500	17.8%	27.1%	47.4%
4706501	15.6%	24.9%	51.7%
22272100	19.1%	22.6%	26.1%
22272101	18.6%	20.4%	47.7%
22733500	16.5%	37.9%	14.6%
23809900	21.5%	21.8%	36.6%
23809901	30.7%	24.0%	18.2%
4011000	53.3%	34.1%	53.0%
4011001	52.2%	40.2%	79.9%
22818600	11.1%	26.1%	27.4%
22818601	12.7%	26.4%	27.9%
22819200	14.7%	21.4%	81.9%
22819201	16.2%	20.9%	42.4%
3083800	19.1%	36.0%	9.1%
3083801	15.2%	39.3%	13.6%
6917200	6.5%	47.3%	7.3%
6917201	13.3%	49.9%	6.7%
6943100	16.8%	37.5%	20.5%
6943101	17.4%	43.6%	20.0%
20180800	39.1%	30.4%	56.1%
20180801	35.7%	34.1%	52.9%
20392000	56.0%	30.3%	57.8%
20392001	21.7%	26.0%	54.3%
22574400	38.8%	35.3%	24.0%
22574401	35.0%	34.9%	30.2%
22645200	22.9%	48.3%	12.3%
22645201	14.2%	34.8%	12.1%
22733501	26.0%	44.3%	10.1%
22765900	30.1%	42.1%	73.1%
22765901	31.8%	38.9%	63.7%
22808000	40.4%	33.8%	48.9%
23152500	23.4%	28.8%	37.5%
23152501	34.1%	25.3%	25.0%
27216101	9.9%	42.4%	17.2%

SVTA: Spatially Varying Threshold Algorithm

CNPA: Constrained Neyman-Pearson Algorithm

Toronto: Toronto method (Dr. Celia Byrne)

Flaggedby Dr. Byrne /distance from chest wall to breast edge is out of range

Results flagged by Dr. Byrne

Training image data

Flagged by Dr. Byrne but used as training data

Test image data

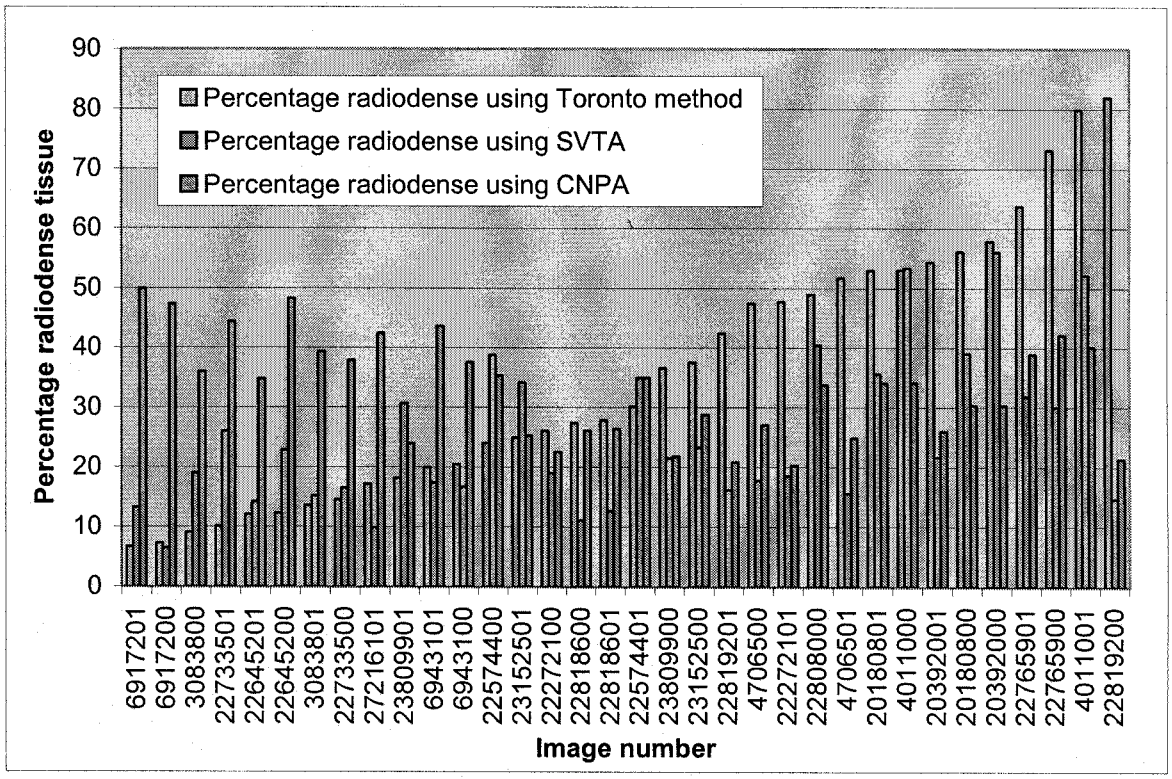

FIGURE 5.32 –Comparison of radiodense tissue segmentation results.

TABLE 5.13 – Performance measures in comparison with the Toronto method.

RMS Error – ALL images (SVTA)	459.8
RMS Error – ALL images (CNPA)	666.5
RMS Error – NON-FLAGGED images (SVTA)	271.62
RMS Error – NON-FLAGGED images (CNPA)	662.6
Correlation – ALL images (SVTA)	49.8%
Correlation – ALL images (CNPA)	-36.9%
Correlation – NON-FLAGGED images (SVTA)	**66.5%**
Correlation – NON-FLAGGED images (CNPA)	-48.3%

CHAPTER 6: CONCLUSIONS

Cancer is second only to heart disease as the leading cause of death among Americans. More specifically, breast cancer is the second leading cause of cancer related deaths. Early detection of breast cancer and the use of breast cancer risk factors are significant in aiding the attack against breast cancer. Breast cancer risk factors play an important role in that they can help predict the possibility of developing breast cancer at an early stage. One of the strongest risk factors is breast density. It has been shown that breast density may predict a four to six fold increase in the risk of developing breast cancer. Also, breast density may be heritable.

Breast density is loosely defined and many of the methods developed suffer from inter- and intra- observer variability. This variability is due to the intervention of the observer in the calculation of radiodense tissue along with breast density being loosely defined. To minimize the inconsistencies between observers, methods were developed that included the support of digital image processing techniques. These methods showed improvements upon previous methods, however still suffered from the variability introduced with the needed interaction of the observer.

A number of methods have recently been developed to allow for a completely automated method to quantify the amount of radiodense tissue in digitized mammograms. While these automated methods have shown improvements from the semi-automated techniques, there are still areas to be improved upon.

6.1 Summary of Accomplishments

The automated method to segment radiodense tissue presented in this thesis incorporates

the effects of tissue compression from the mammography procedure. A survey of existing literature regarding the automated segmentation of radiodense tissue infers that no other researchers are including the effects created by tissue compression.

This method segments the breast tissue region from the outside film region automatically with the assistance of radial basis function neural networks. The system creates a binary mask template that localizes the breast tissue region and allows for subsequent processes to be performed for the segmentation of radiodense tissue.

The constrained Neyman-Pearson algorithm is used to analyze the digitized mammogram for a global threshold. This threshold is created with the knowledge of the underlying distributions that make up the tissue region of the mammogram.

A parametric model for tissue location is developed using the homotopy continuation algorithm. The homotopy continuation algorithm generates a family of curves between the chest wall boundary and the edge of the breast tissue boundary in the mammogram. Tissue compression is modeled as a Gaussian function to allow for the global threshold to be greater at the chest wall and decrease outward towards the edge of the breast tissue. The threshold values generated using the Gaussian functions are transcribed to the parametric model for tissue location. A series of moving average filters applied to the family of curves with the values from the Gaussian function creates a spatially varying threshold model. Using this threshold model, the radiodense tissue is segmented and quantified.

The proposed algorithm presented in this thesis has been developed using a set of ten images provided by an expert radiologist. The ten images were analyzed by an expert using the 'Toronto' method to calculate the percentage of radiodense tissue. Promising

results were obtained using an optimization procedure to determine the parametric model for tissue compression in each image. The algorithm was then validated using a separate database; again, the radiodensity estimates provided by expert radiologist was used to compare the performance of the technique described in this thesis. The results presented in this thesis demonstrate significant improvement in performance, as compared with an expert, over previously developed automated radiodensity estimation techniques.

6.2 Recommendations for Future Work

The algorithm presented in this thesis is a step towards developing a robust, completely automated system for quantifying radiodense tissue in digitized mammograms. However, the technique presented in this thesis suffers some drawbacks. The following areas of research are possible advancements towards this automated system:

The segmentation of radiodense regions is done on a pixel-by-pixel basis, which is unlike the procedure employed by a radiologist. Area based segmentation approaches must be explored.

The tissue compression model in this thesis, while reasonable, remains to be validated. Experiments and finite element modeling studies are necessary for arriving at accurate compression characteristics.

Breast density is not objectively defined. There is significant intra- and inter-observer variability in breast density estimation. Efforts towards developing a more formal and objective definition of breast density, using calibrated breast phantoms, may help in the design of an accurate and robust automated segmentation technique.

Additional risk factors and a priori information is ignored in this research. However, the inclusion of additional risk factors such as the age and patient history may

prove beneficial in the segmentation of radiodense tissue.

REFERENCES

1. R. A. Anderson, "Deaths: leading causes for 2000," *National Vital Statistics Reports*, Vol. 50, No.16, Centers for Disease Control, 2002 [Online].

   http://www.cdc.gov/nchs/data/nvsr/nvsr50/nvsr50_16.pdf

2. American Cancer Society, *Breast Cancer Facts & Figures*, 2001-2002 [Online]. http://www.cancer.org/downloads/STT/BrCaFF2001.pdf

3. E.J. Feuer, L.M. Wun, "DEVCAN: Probability of Developing or Dying of Cancer," Software, version 4.0, National Cancer Institute, 1999.

4. American Cancer Society, *Cancer Facts & Figures*, 2002 [Online].

   http://www.cancer.org/downloads/STT/CancerFacts&Figures2002TM.pdf

5. L. Tabar, B. Vitak, H.H. Chen, M.F. Yen, S.W. Duffy, and R.A. Smith, "Beyond randomized controlled trials: organized mammographic screening substantially reduces breast carcinomar mortality, *Cancer 2001*, Vol. 91, No. 9, pp. 1724-1731, 2001.

6. Imaginis. 2002. Methods of Breast Biopsy. Siemens [Online].

   http://www.imaginis.com/breasthealth

7. Issam El-Naqa, Yongyi Yang, Miles N. Wernick, Nikolas P. Galatsanos, and Robert Nishikawa, "Support Vector Machine Learning for Detection of Microcalcifications in Mammograms", *IEEE International Symposium on Biomedical Imaging*, Washington D.C., July 2002.

8. Bazzani, A. Bevilacqua, D. Bollini, R. Campanini, N. Lanconelli, A. Riccardi, D. Romani, *Proceedings of the International Workshop on Digital Mammography 2000*, pp. 161-167, Toronto, Canada, June 11-14, 2000.

9. Bazzani, A. Bevilacqua, D. Bollini, R. Campanini, N. Lanconelli, A. Riccardi, D. Romani, "Automatic detection of clustered microcalcifications using a combined method and an SVM classifier", *LXXXVII Congresso Nazionale Societa' Italiana di Fisica*, Milan, Italy, September 24-29, 2001.

10. Keir Bovis and Sameer Singh, "Detection of masses in mammograms using texture features", *International conference on pattern recognition*, Vol. 2, Barcelona, Spain, September 03-08, 2000.

11. M.F. Salfity, G.H. Kaufmann, P.M. Granitto and H.A. Ceccatto, "A computer-aided diagnosis method for automated detection and classification of clustered microcalcifications in mammograms", *Proceedings of the Argentine Symposium on Healthcare Informatics*, Tandil, 41-47 (2000).

12. J.L. Kelsey and M. Gammon, "The epidemiology of breast cancer", *CA Cancer Journal*; Vol. 41, pp. 146-165, 1991.

13. Byrne, C, et. al. "Mammographic features and breast cancer risk: effects with time, age, and menopause status." *Journal of the National Cancer Institute*, Vol. 87, *pp.*1622-1629, 1995.

14. Byrne, "Studying mammographic density: implications for understanding breast cancer," *Journal of the National Cancer Institute*, Vol. 89, pp. 531-533, 1997

15. Haiman, L. Bernstein, D. Van Den Berg, S. A. Ingles, M. Salane and G. Ursin, "Genetic determinants of mammographic density," *Breast Cancer Res* 2002 4(3):R5.

16. Mirada Solutions, Virtual Mammo – "Radiation Dose in Mammography" – Continuing Education Program, 2001-2002.

17. N.F. Boyd, G.A. Lockwood, J.W. Byng, D.L. Tritchler, and M.J. Yaffe, "Mammographic densities and breast cancer risk," *Cancer Epidemiol Biomarkers Prev*, Vol. 7, pp. 1133-1144, 1998.

18. R.L. Egan, "Breast imaging: diagnosis and morphology of breast diseases," W.B. Saunders Company, Philadelphia, 1988.

19. J. W. Byng, N. F. Boyd, E. Fishell, R. A. Jong and M. J. Yaffe, "Quantitative analysis of mammographic densities," *Physics in Medicine and Biology,* Vol. 41, pp. 909-923, 1996.

20. J.N. Wolfe, *Xeroradiography of the breast*, Thomas, 1972.

21. C.A. Beam, E.F. Conant, E.A. Sickles, "Factors affecting radiologist inconsistency in screening mammography," *Academic Radiology*, Vol. 9, No. 5, pp. 531-540, 2002.

22. American College of Radiology (ACR) Breast Imaging Reporting and Data System (BI-RADS) Third Edition. Reston, VA: American College of Radiology, 2003.

23. J.N. Wolfe, "Breast patterns as an index of risk of developing breast cancer," *American Journal of Roentgenology*, Vol. 126, pp. 1130-1139, 1976.

24. J.N. Wolfe, "Risk of breast cancer development determined by mammographic parenchymal pattern," *Cancer*, Vol. 37, pp. 2486-2492.

25. A.F. Saftlas, M. Szklo, "Mammographic parenchymal patterns and breast cancer risk," *Epidemiol Rev*, Vol. 9, pp. 146-174, 1987.

26. A.M. Oza, N.F. Boyd, "Mammographic parenchymal patterns: a marker of breast cancer risk," *Epidemiol Rev*, Vol. 15, pp. 196-208, 1993.

27. E. Warner, G. Lockwood, D. Tritchler, N.F. Boyd, "The risk of breast cancer associated with mammographic parenchymal patterns: a meta-analysis of the published literature to examine the effect of method of classification," *Cancer Detect Prev*, Vol. 16, pp. 67-72, 1992.

28. N.F. Boyd, G.A. Lockwood, L.J. Martin, J.A. Knight, J.W. Byng, M.J. Yaffe, D.L. Tritchler, "Mammographic densities and breast cancer risk," *Breast Disease*, Vol. 10, pp. 113-126, 1998.

29. N.F. Boyd, J. Byng, R. Jong, E. Fishell, L. Little, A.B. Miller, G. Lockwood, D. Tritchler, M. Yaffe, "Quantitative classification of mammographic densities and breast cancer risks: results from the Canadian National Breast Screening Study," *Journal of the National Cancer Institute*, Vol. 87, pp. 670-675, 1995.

30. C.A. Bodian, "Benign breast diseases, carcinoma *in situ*, and breast cancer risk," *Epidemiol Rev*, Vol. 15, pp. 177-187, 1993.

31. N.F. Boyd, B. O'Sullivan, J.E. Campbell, E. Fishell, I. Simor, G. Cooke, *et al*, "Mammographic signs as risk factors for breast cancer," *British Journal of Cancer*, Vol. 45, pp. 185-193, 1982.

32. J.N. Wolfe, A.F. Saftlas, M. Salane, "Mammographic parenchymal patterns and quantitative evaluation of mammographic densities: a case-control study," *American Journal of Roentgenology*, Vol. 148, pp. 1087-1092, 1987.

33. J. Brisson, R. Verreault, A.S. Morrison, S. Tennina, F. Meyer, "Diet, mammographic features of breast tissue, and breast cancer risk," *American Journal of Epidemiology*, Vol. 130, pp. 14-24, 1989.

34. A.F. Saftlas, R.N. Hoover, L.A. Brinton, M. Szklo, D.R. Olson, M. Salane, *et al*, "Mammographic densities and risk of breast cancer," *Cancer*, Vol. 67, pp. 2833-2838, 1991.

35. S.A. Bartow, D.R. Pathak, F.A. Mettler, C.R. Key, and M.C. Pike, "Breast mammographic pattern: a concatenation of confounding and breast cancer risk factors," *American Journal of Epidemiology*, Vol. 142, pp. 813-819, 1995.

36. N.F. Boyd, G.S. Dite, J. Stone, A. Gunasekara, D.R. English, M.R. McCredie, *et al*, "Heritability of mammographic density, a risk factor for breast cancer," *New England Journal of Medicine*, Vol. 347, pp. 886-894, 2002.

37. J.S. Grove, M. J. Goodman, F.I. Gilber, *et al*, "Wolfe's mammographic classification and breast cancer risk: the effect of misclassification on apparent risk ratios," *British Journal of Radiology*, Vol. 58, pp. 15-19, 1985.

38. N.F. Boyd, H.M. Jensen, G. Cooke, H. Lee Han, "Relationship between mammographic and histological risk factors for breast cancer," *Journal of the National Cancer Institute*, Vol. 84, pp. 1170-1179, 1992.

39. M.J. Yaffe, N.F. Boyd, J.W. Byng, R.A. Jong, E. Fishell, G.A. Lockwood, L.E. Little, D. L. Tritchler, "Breast cancer risk and measured mammographic density," *European Journal of Cancer Prevention*, Vol. 7 (suppl 1), pp. S47-S55, 1998.

40. J.W. Byng, N.F. Boyd, E. Fishell, R.A. Jong, and M.J. Yaffe, "Quantitative analysis of mammographic densities," *Physics in Medicine and Biology*, Vol. 39, pp. 1629-1638, 1994.

41. P. Silgen, "Quantification of breast density using magnetic resonance imaging," *MS thesis*, Department of Radiology, Minneapolis, MN: University of Minnesota, 1996.

42. J.C. Weinreb and G. Newstead, "MR imaging of the breast," *Radiology*, Vol. 196, pp. 593-610, 1995.

43. S.L. Lou and Y. Fan, "Automatic evaluation of breast density for full-field digital mammography," *Medical Imaging 2000: Image Processing*, Vol. 3979, pp. 1362-1369, 2000.

44. C. Zhou, H. Chan, N. Petrick, M.A. Helvie, M.M. Goodsitt, B. Sahiner, and L. Hadjiiski, "Computerized image analysis: Estimation of breast density on mammograms," *Medical Physics*, Vol. 28, pp. 1056-1069, June 2001.

45. C. Zhou, H. Chan, N. Petrick, B. Sahiner, M. Helvie, M. Roubidoux, L. Hadjiiski, M. Goodsitt, "Computerized image analysis: Estimation of breast density on mammograms," *Medical Imaging 2000: Image Processing*, Vol. 3979, pp. 1615-1624, 2000.

46. K. Bovis and S. Singh, "Classification of breast density in digital mammograms," *Submitted to Pattern Analysis and Neural Networks.*

47. S. Petroudi, K. Marias, R. English, R. Adams, and M. Brady, "Classification of mammogram patterns using area measurements and the standard mammogram form (SMF)," *Medical Image Understanding and Analysis*, 2002.

48. P.K. Saha, J.K. Udupa, E.F. Conant, D.P. Chakraborty, and D. Sullivan, "Breast tissue density quantification via digitized mammograms," *IEEE Transaction on Medical Imaging*, Vol. 20, No. 8, 2001.

49. B. B. Mandelbrot, *The Fractal Geometry of Nature*, W.H. Freeman, 1982.

50. K. R. Castleman, *Digital Image Processing,* Prentice-Hall, 1996.

51. M. J. Yaffe, J. W. Byng, N. F. Boyd, "Quantitative image analysis for estimation of breast cancer risk," *Handbook of Medical Imaging, Processing and Analysis,* Ch. 21, Academic Press, 2000.

52. J.W. Byng, N.F. Boyd, L. Little, *et al*, "Symmetry of projection in the quantitative analysis of mammographic images," *European Journal of Cancer Prevention*, Vol. 5, pp. 319-327, 1996.

53. J.T. Neyhart, "Automated segmentation of radiodense tissue in digitized mammograms using a constrained Neyman-Pearson classifier," *MS Thesis*, Department of Electrical and Computer Engineering, Glassboro, NJ: Rowan University, 2002.

54. J. Neyhart, M. Ciocco, R. Polikar, S. Mandayam, and M. Tseng, "Dynamic segmentation of breast tissue in digitized mammograms using the discrete wavelet transform," *Proceedings of the 23rd Annual International Conference of the IEEE Engineering in Medicine and Biology Society*, Istanbul, Turkey, October 2001.

55. J.T. Neyhart, R.E. Eckert, R. Polikar, S. Mandayam and M. Tseng, "A modified Neyman-Pearson technique for radiodense tissue estimation in digitized mammograms", *Proceedings of the 24th Annual International Conference of the IEEE Engineering in Medicine and Biology Society*, Houston, Texas, October 2002.

56. J. Neyhart, M. Kirlakovsky, L. Coleman, R. Polikar, M. Tseng and S. Mandayam, "Automated Segmentation and Quantitative Characterization of Radiodense Tissue in Digitized Mammograms", *Proceedings of the 28th Annual Review of Progress in Quantitative NDE*, American Institute of Physics, New York, July 2001.

57. R.E. Eckert, J.T. Neyhart, L. Burd, R. Polikar, S. Mandayam and M. Tseng, "Neural and Decision Theoretic Approaches for the Automated Segmentation of Radiodense Tissue in Digitized Mammograms", *Proceedings of the 29th Annual Review of Progress in Quantitative NDE*, American Institute of Physics, Bellingham, Washington, July 2002.

58. S. Haykin, *Neural Networks - A Comprehensive Foundation*, Second Edition, Prentice Hall, Upper Saddle River, NJ, 1999.